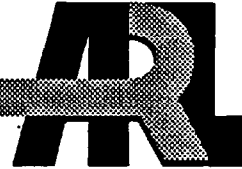


ARMY RESEARCH LABORATORY



# Initial Development of Core Module of Next Generation Interior Ballistic Model NGEN

Paul S. Gough

ARL-CR-234

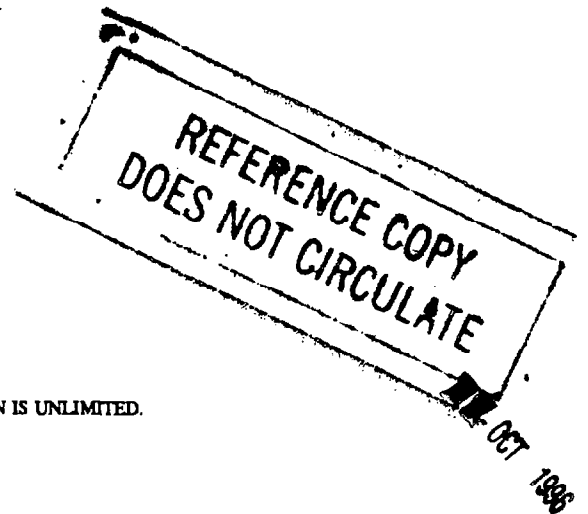
June 1995

prepared by

**Paul Gough Associates, Inc.  
1048 South Street  
Portsmouth, NH 03801-5423**

under contract

**DAAA15-92-D-0001**



APPROVED FOR PUBLIC RELEASE; DISTRIBUTION IS UNLIMITED.

## **NOTICES**

**Destroy this report when it is no longer needed. DO NOT return it to the originator.**

**Additional copies of this report may be obtained from the National Technical Information Service, U.S. Department of Commerce, 5285 Port Royal Road, Springfield, VA 22161.**

**The findings of this report are not to be construed as an official Department of the Army position, unless so designated by other authorized documents.**

**The use of trade names or manufacturers' names in this report does not constitute endorsement of any commercial product.**

# REPORT DOCUMENTATION PAGE

*Form Approved*  
*OMB No. 0704-0188*

Public reporting burden for this collection of information is estimated to average 1 hour per response, including the time for reviewing instructions, searching existing data sources, gathering and maintaining the data needed, and completing and reviewing the collection of information. Send comments regarding this burden estimate or any other aspect of this collection of information, including suggestions for reducing this burden, to Washington Headquarters Services, Directorate for Information Operations and Reports, 1215 Jefferson Davis Highway, Suite 1204, Arlington, VA 22202-4302, and to the Office of Management and Budget, Paperwork Reduction Project(0704-0188), Washington, DC 20503.

1. AGENCY USE ONLY (Leave blank)	2. REPORT DATE June 1995	3. REPORT TYPE AND DATES COVERED Final, Jan 92 - Oct 94	
4. TITLE AND SUBTITLE  Initial Development of Core Module of Next Generation Interior Ballistic Model NGEN		5. FUNDING NUMBERS  DAAA15-92-D-0001 PR: IL161102AH43	
6. AUTHOR(S)  Paul S. Gough		8. PERFORMING ORGANIZATION REPORT NUMBER  PGA-TR-94-1	
7. PERFORMING ORGANIZATION NAME(S) AND ADDRESS(ES)  Paul Gough Associates, Inc. 1048 South St. Portsmouth, NH 03801-5423		9. SPONSORING/MONITORING AGENCY NAMES(S) AND ADDRESS(ES)  U.S. Army Research Laboratory ATTN: AMSRL-WT-PA Aberdeen Proving Ground, MD 21005-5066	
11. SUPPLEMENTARY NOTES The point of contact for this report is Dr. George E. Keller, U.S. Army Research Laboratory, ATTN: AMSRL-WT-PA, Aberdeen Proving Ground, MD 21005-5066.		10. SPONSORING/MONITORING AGENCY REPORT NUMBER  ARL-CR-234	
12a. DISTRIBUTION/AVAILABILITY STATEMENT  Approved for public release; distribution is unlimited.		12b. DISTRIBUTION CODE	
13. ABSTRACT (Maximum 200 words) Gun Propulsion systems of current interest include the traditional solid propellant (SP) designs, regenerative liquid propellant (RLP) designs and various electrothermal-chemical (ETC) designs. Presently, each of these systems is simulated by dedicated computer codes which are not readily extendible to the other systems. It is a goal of the Army Research Laboratory to develop a Next-Generation code which subsumes the capabilities of all existing codes into a structure which is modular and readily transportable from one propulsion engineer to another as well as from one computer architecture to another.  The present report describes progress in the development of such a code referred to as NGEN. We present an algorithm to integrate the properties of the products of combustion in the presence of nonuniform geometry using the LCPFCT methodology on a structured rectangular mesh. Only those cells which are intercepted by bounding surfaces are given special treatment. This continuum flow solver is coupled to a Large Particle Integrator which determines the state of the propellant grains in a solid propellant charge.  The operability of the code is illustrated by reference to two simulations, one for a 155-mm howitzer and one for a 120-mm tank gun.			
14. SUBJECT TERMS  interior ballistics, modeling, numerical analysis		15. NUMBER OF PAGES 102	
17. SECURITY CLASSIFICATION OF REPORT UNCLASSIFIED		16. PRICE CODE	
18. SECURITY CLASSIFICATION OF THIS PAGE UNCLASSIFIED		19. SECURITY CLASSIFICATION OF ABSTRACT UNCLASSIFIED	
20. LIMITATION OF ABSTRACT  UL			

INTENTIONALLY LEFT BLANK.

Foreword

Technical cognizance for the subject contract was provided by Dr. G. E. Keller, Code AMSRL-WT-PE.

INTENTIONALLY LEFT BLANK.

## TABLE OF CONTENTS

	Page
Foreword.....	iii
List of Illustrations.....	vii
1.0 INTRODUCTION.....	1
2.0 THE GOVERNING EQUATIONS.....	4
2.1 General Statement of the Balance Equations.....	4
2.2 Balance Equations for Current NGEN Code.....	8
2.3 Constitutive Laws.....	10
2.3.1 Equation of State of Continuous Phase.....	11
2.3.2 Equation of State for Discrete Phase (Intergranular Stress Law).....	11
2.3.3 Discrete Phase Morphology (Form Functions).....	12
2.3.4 Interphase Drag.....	13
2.3.5 Interphase Heat Transfer.....	14
2.3.6 Solid Phase Surface Temperature.....	15
2.3.7 Ignition and Combustion.....	15
2.4 Boundary Conditions and Projectile Motion.....	16
3.0 METHOD OF SOLUTION.....	17
3.1 Summary of LCPFCT Algorithm.....	17
3.2 Treatment of Non-Uniform Geometry.....	20
3.3 Characteristic Based Application of LCPFCT to Two- Dimensional Flow with Non-Uniform Boundaries.....	27
3.4 The Large Particle Integrator (LPI).....	33
4.0 NUMERICAL SOLUTIONS.....	38
5.0 CONCLUSIONS.....	59
References.....	61
Nomenclature.....	65
Appendix A: Characteristic Analysis of Continuum Equations.....	69
A.1 General Formulation of Characteristic Analysis.....	71
A.2 Two-Dimensional Inviscid Single-Phase Flow.....	74
Appendix B: Description of NGEN Input Files.....	85

INTENTIONALLY LEFT BLANK.

## LIST OF ILLUSTRATIONS

Figure	Title	Page
3.1	Comparison of Virtual Cell and Physical Cell Analysis of Boundary Element for One-Dimensional Problem.....	22
3.2	Chamber and Afterbody Geometry as Represented in NGEN Code.....	28
4.1	Porosity Distributions in 155mm Howitzer at Four times.....	43
4.2	Pressure Distributions in 155mm Howitzer at Four times.....	44
4.3	Gas-Phase Flow Field in 155mm Howitzer at 0.5 ms.....	45
4.4	Comparison of NGEN and XKTC Ballistic Predictions for 155mm Howitzer.....	46
4.5	Porosity Distributions in 120mm Tank Gun at Four times.....	52
4.6	Gas-Phase Flow Field in 120mm Tank Gun at 1.5 ms.....	53
4.7	Gas-Phase Flow Field in 120mm Tank Gun at 3.0 ms.....	54
4.8	Gas-Phase Flow Field in 120mm Tank Gun at 4.5 ms.....	55
4.9	Pressure Contours in 120mm Tank Gun at 1.5 ms.....	56
4.10	Pressure Contours in 120mm Tank Gun at 3.0 ms.....	57
4.11	Pressure Contours in 120mm Tank Gun at 4.5 ms.....	58

**INTENTIONALLY LEFT BLANK.**

## 1.0 INTRODUCTION

Currently, a number of different codes are used to model various types of propulsion systems. Multidimensional models of solid propellant charges have been developed by Fisher and Graves (1972), Gough (1983), Meineke and Heiser (1989), Groenenboom and Thomsen (1989), Fitt et al (1989), Gibelung and McDonald (1984) and Schmitt (1984). Codes to model regenerative liquid propellant guns have been developed by Steffens et al (1987, 1989) and by Coffee (1990). The recent surge of interest in electrothermal-chemical guns has resulted in the development of several models, including those by Chen et al (1990), Kashiwa et al (1990), Cook et al (1989), Winsor and Goldstein (1990), Sinha et al (1991) and Hsiao et al (1991).

All these codes solve subsets of a generally accepted system of equations for multiphase flow. They differ as to constitutive assumptions and the method of solution. Some have a three-dimensional capability. Others do not.

It is a goal of the US Army to develop a Next-Generation code based on a flow solver which is applicable to all the types of gun systems of current and foreseeable interest. It is intended that the code have a three-dimensional capability and be able to address problems that either strain current computational resources or exceed them. Anticipating that such a code would benefit from the emerging new architectures based on massively parallel systems of processors, it is essential that the flow solver be as simple as possible, thereby facilitating reprogramming to take advantage of these new architectures. Simplicity is also desired so that the code can be readily adapted by specialists in each of the various gun system phenomenologies, since it is they who will propose the appropriate constitutive laws.

We have previously suggested an approach to the development of such a code (Gough, 1991). We suggested that an algorithmic distinction be made between the continuous phases and the large discrete phases. In the context of a solid propellant gun the continuous phases would be understood to be the products of combustion while the discrete phases would be defined by the propellant grains. In our formulation we did include the possibility that the

continuous phase might include small particles or droplets on the assumption that they were in mechanical equilibrium with the gases. We suggested that a Continuum Flow Solver (CFS) be developed with the following properties. First and foremost, the solver had to be simple to code and modify in order to promote portability from user to user and from computer to computer. Second, the solver should ideally be explicit rather than implicit, since explicit solvers tend to be much simpler to use and modify, and interior ballistic problems rarely require the sort of mesh resolution defined by wall boundary layer problems which absolutely demand an implicit treatment. Also, since most interior ballistic simulations require wave tracking, integration using Courant numbers larger than unity is not desirable. Third, the method had to be robust. A shock capturing capability was desirable in order to be able to analyze certain classes of propelling charges. Much more important, however, was the ability to remain stable in the presence of strong porosity gradients which would always occur near the boundaries of solid propellant charge increments. Finally, the development of the flow solver would have to anticipate the geometrical complexities associated not only with chamber and projectile shape but also the more formidable characteristics of the increment containers typical of artillery ammunition.

We did not suggest that the continuum solver be required to integrate the motion of the large particles. For that purpose we suggested the development of a second module, referred to as a Large Particle Integrator (LPI), to be appropriately coupled to the continuum integrator. For charge designs which were liquid based, such as Regenerative or Bulk-Loaded Liquid Guns, or for certain Electrothermal-Chemical Guns, the Large Particle Integrator would not necessarily be required. The presence of droplets could be represented within the continuous phase unless a separated flow analysis were justified by the availability of appropriate constitutive data.

In previous studies (Gough, 1991 and 1992), we have identified the principle of Flux-Corrected Transport (Boris and Book, 1976; Boris et al, 1993) as a suitable basis for the continuum flow solver. The method is explicit and simple to use. It has been shown to adapt easily to massively parallel systems

(Oran et al, 1990). It has been shown to be appropriate to ETC problems (Hsiao et al, 1991) and preliminary suitability to SP problems has been shown by Gough (1992).

In the present work we describe two important steps in the development of a Next-Generation Code, referred to as the NGEN Code. We discuss the treatment of non-uniform geometry and present an algorithm for the Large Particle Integrator (LPI). Non-uniform geometry is treated by means of a structured rectangular mesh in which only those cells intercepted by an external boundary element require special treatment. This approach has been developed with a view to the requirement that the code will subsequently be applied to the simulation of artillery ammunition for which the presence of packaging materials defines a number of internal boundary conditions. The method described here is expected to adapt readily to that requirement and to minimize computational mesh distortion associated with motion of the boundaries as would occur for example if a boundary conformal mesh were used.

The LPI algorithm is essentially Lagrangian, the motion of an aggregate of particles being tracked explicitly. However, the method of coupling to the continuum flow involves an attribution of properties, such as porosity, mass generation and so forth, whose spatial variation can be explicitly controlled near the boundaries of each charge increment, thereby defining sufficiently smooth distributions to maintain stability of the continuum solver.

In Chapter 2.0 we discuss the governing equations presently encoded. The method of solution is presented in Chapter 3.0. In Chapter 4.0 we illustrate the code capabilities by reference to two data bases, one for a 155mm howitzer and one for a 120mm tank gun. The discussion of Chapter 3.0 is supported by Appendix A which presents a characteristic analysis of the equations of two-dimensional inviscid flow. Appendix B presents a listing of the current NGEN input files.

## 2.0 THE GOVERNING EQUATIONS

We first provide a general statement of the balance equations for a multiphase mixture in Section 2.1. In Section 2.2 we present the reduced set which is encoded into the present version of the NGEN Code. In Section 2.3 we discuss the current set of constitutive laws. In Section 2.4 we note the boundary conditions and the equation of motion of the projectile.

### 2.1 General Statement of the Balance Equations

The various systems of equations which have been considered in current models are all subsets of the macroscopic balance equations for a multi-component mixture as discussed elsewhere (Gough, 1992).

The mixture may be viewed as consisting of a multicomponent fluid, referred to as the continuous phase, and an aggregate of droplets or solid particles, referred to as the discrete phase. The continuous phase is understood to be a multi-component mixture of gases and droplets or particles which are small enough to ensure local mechanical equilibrium. The gases are always in local thermal equilibrium while the droplets and particles are not necessarily so. The continuous phase is characterized by single local values of density,  $\rho$ ; velocity vector,  $u$ ; temperature,  $T$ ; pressure,  $p$ ; shear stress tensor,  $\tau$ ; and internal energy,  $e$ . It is assumed to comprise  $N_c$  species each characterized by local values of mass fraction  $Y_i$ ,  $i = 1, \dots, N_c$ . Moreover, the velocity  $u$  is understood to be the barycentric or mass weighted average of the velocities of each of the components (Williams, 1965). Each component is characterized by a diffusion velocity  $v_i$  relative to the barycentric value  $u$ .

The term discrete phase is understood to refer to an aggregate of particles or droplets. If a solid propellant charge is being modeled, each type of propellant will constitute a component of the discrete phase. Other components may be present if the decomposition of the propellant or an igniter element yields intermediate combustion products in particulate or droplet form. Still other components may need to be considered if rupture of a container is to be modeled or if wear-reducing additives like talc are present and their

dispersal pattern is to be calculated. In the case of the RLPG the aggregate may consist of a spray created by the breakup of the injected jet of liquid propellant. Similarly, in the ETC the aggregate may consist of droplets created by the Helmholtz instability on the boundary of the Taylor cavity. Because of the generality implicit in the representation of the continuous phase, the foregoing components of the discrete phase, except for the solid propellant grains, may be optionally included in the continuous phase and modeled according to a homogeneous mixture representation. Alternatively, they may be modeled independently when the situation so warrants.

We assume that the discrete phase consists of a total of  $N_d$  components. Each component is characterized by density,  $\rho_{d_i}$ ; stress tensor,  $\sigma_{d_i}$ ; velocity vector,  $u_{d_i}$ ; temperature,  $T_{d_i}$ ; number density,  $n_{d_i}$ ; and morphological data to characterize the volume,  $V_{d_i}$ , and surface area,  $S_{d_i}$  of each particle or droplet. The temperature  $T_{d_i}$  may be either a surface or a bulk temperature depending on the nature of the model assumptions for the problem in question.

In general it is necessary to consider a macroscopic formulation of the balance equations due to the presence of the discrete phases. The macroscopic formulation is such that it reduces to standard continuum equations in the context of single-phase flow. Given a microflow property  $\psi$  we use  $\langle\psi\rangle$ ,  $\langle\psi\rangle_\rho$  and  $\langle\psi\rangle_s$  to respectively denote a bulk average, a mass-weighted (Favre) average and an interphase surface average.

We use  $\alpha$  to denote the porosity, or the fraction of a unit macroscopic volume occupied by the continuous phase. Similarly, we use  $\alpha_{d_i}$  to denote the volume fraction of the  $i$ -th discrete phase. Evidently,

$$\alpha = 1 - \sum_{i=1}^{N_d} \alpha_{d_i} \quad . \quad 2.1.1$$

We may now state the balance equations for the continuous phase in the following forms which differ from those presented earlier (Gough, 1992) only in respect to the neglect of certain correlation terms which result from the formal macroscopic averaging process.

We have the balance of mass

$$\frac{\partial}{\partial t} [\alpha \langle \rho \rangle] + \nabla \cdot [\alpha \rho \langle \mathbf{u} \rangle_\rho] = \sum_{i=1}^{N_d} \dot{m}_{d_i} \quad , \quad 2.1.2$$

where  $\dot{m}_{d_i}$  is the rate of decomposition per unit volume of the  $i$ -th discrete phase.

Each of the  $j$  components of the continuous phase satisfies a balance of mass equation in the following form,

$$\begin{aligned} \frac{\partial}{\partial t} [\alpha \langle \rho \rangle \langle Y_j \rangle_\rho] + \nabla \cdot [\alpha \langle \rho \rangle \langle Y_j \rangle_\rho (\langle \mathbf{u} \rangle_\rho + \langle \mathbf{v}_j \rangle_\rho)] \\ = \alpha \langle \dot{\omega}_j \rangle + \sum_{i=1}^{N_d} \dot{m}_{d_i} \langle Y_{d_{ij}} \rangle_s \end{aligned} \quad 2.1.3$$

Here  $\langle \dot{\omega}_j \rangle$  is the average rate of production per unit volume of species  $j$  by chemical reactions and  $\langle Y_{d_{ij}} \rangle_s$  is the average mass fraction of species  $j$  produced by the decomposition of the  $i$ -th discrete phase including the effect of the surface reaction. The macroscopic balance of momentum for the continuous phase takes the form

$$\begin{aligned} \frac{\partial}{\partial t} [\alpha \langle \rho \rangle \langle \mathbf{u} \rangle_\rho] + \nabla \cdot [\alpha \langle \rho \rangle \langle \mathbf{u} \rangle_\rho \langle \mathbf{u} \rangle_\rho] \\ = -\alpha \nabla \langle p \rangle + \alpha \nabla \cdot \langle \mathbf{r} \rangle + \sum_{i=1}^{N_d} \dot{m}_{d_i} \langle \mathbf{u}_{d_i} \rangle - \sum_{i=1}^{N_d} n_{d_i} S_{d_i} \mathbf{f}_{d_i} \end{aligned} \quad 2.1.4$$

Here  $\mathbf{f}_{d_i}$  represents the interphase drag due to the  $i$ -th discrete phase.

The energy equation for the continuous phase takes the form

$$\begin{aligned} \frac{\partial}{\partial t} \left\{ \alpha \langle \rho \rangle \left[ \langle e \rangle_\rho + \frac{1}{2} \langle u \rangle_\rho^2 \right] \right\} + \nabla \cdot \left\{ \alpha \langle \rho \rangle \langle u \rangle_\rho \left[ \langle e \rangle_\rho + \frac{1}{2} \langle u \rangle_\rho^2 \right] \right\} \\ = \nabla \cdot \alpha \langle u \rangle_\rho \cdot \langle \sigma \rangle - \nabla \cdot \alpha \langle q \rangle - \langle p \rangle \frac{\partial \alpha}{\partial t} - \sum_{i=1}^{N_d} n_{d_i} S_{d_i} \langle q_{d_i} \rangle_s \\ - \sum_{i=1}^{N_d} n_{d_i} S_{d_i} f_{d_i} \cdot \langle u_{d_i} \rangle_\rho + \sum_{i=1}^{N_d} \dot{m}_{d_i} \left[ \langle e_{d_i} \rangle + \frac{\langle p \rangle}{\langle \rho_{d_i} \rangle} + \frac{\langle u_{d_i} \rangle^2}{2} \right] \end{aligned} \quad 2.1.5$$

We note the phase interaction terms on the right hand side of Equation 2.1.5. The first of these introduces the heat transfer due to conduction and radiation per unit surface area  $\langle q_{d_i} \rangle_s$ . The next term represents the work done by the interphase drag. The third term represents the heat added due to decomposition of the discrete phases.

The  $i$ -th discrete phase is found to be governed by a macroscopic mass balance analogous to that for the continuous phase, namely

$$\frac{\partial}{\partial t} [\alpha_{d_i} \langle \rho_{d_i} \rangle] + \nabla \cdot [\alpha_{d_i} \langle \rho_{d_i} \rangle \langle u_{d_i} \rangle_\rho] = - \dot{m}_{d_i} \quad 2.1.6$$

The  $i$ -th discrete phase is governed by a macroscopic balance equation in the following form

$$\begin{aligned} \frac{\partial}{\partial t} [\alpha_{d_i} \langle \rho_{d_i} \rangle \langle u_{d_i} \rangle_\rho] + \nabla \cdot [\alpha_{d_i} \langle \rho_{d_i} \rangle \langle u_{d_i} \rangle \langle u_{d_i} \rangle] \\ = - \alpha_{d_i} \nabla \langle p \rangle - \nabla \cdot [\alpha_{d_i} \langle \sigma_{d_i} \rangle] + n_{d_i} S_{d_i} f_{d_i} - \dot{m}_{d_i} \langle u_{d_i} \rangle_\rho \end{aligned} \quad 2.1.7$$

We note on the right hand side of Equation 2.1.7 the formal presence of a stress term  $\langle \sigma_{d_i} \rangle$  which reflects the difference between the average stress in the  $i$ -th discrete phase and the average ambient pressure in the continuous phase. This is interpreted as reflecting interactions between droplets or particles.

## 2.2 Balance Equations for Current NGEN Code

In the current version of the code diffusive processes are not considered. We consider the mixture to consist of a continuous phase - the combustion products - with constant thermodynamic properties, and a single discrete aggregate - the propelling charge. In order to provide a vehicle for the representation of an igniter we include the influence of a local source term. We consider the continuous phase first. Since there is no composition dependence, Equation 2.1.3 is not required. Moreover, we drop the explicit representation of the averages. The resulting balance equations for the continuous phase are therefore

$$\frac{\partial \alpha \rho}{\partial t} = - \frac{\partial}{\partial z} \alpha \rho u - \frac{1}{r} \frac{\partial}{\partial r} r \alpha v + \dot{m} + \dot{m}_{ig} \quad , \quad 2.2.1$$

$$\frac{\partial \alpha \rho u}{\partial t} = - \frac{\partial}{\partial z} \alpha \rho u u - \frac{1}{r} \frac{\partial}{\partial r} r \alpha \rho u v - \alpha g_o \frac{\partial p}{\partial z} + \dot{m} u_p - f_z \quad , \quad 2.2.2$$

$$\frac{\partial \alpha \rho v}{\partial t} = - \frac{\partial}{\partial z} \alpha \rho v u - \frac{1}{r} \frac{\partial}{\partial r} r \alpha \rho v v - \alpha g_o \frac{\partial p}{\partial r} + \dot{m} v_p - f_r \quad , \quad 2.2.3$$

$$\begin{aligned} \frac{\partial \alpha E}{\partial t} = & - \frac{\partial}{\partial z} \alpha u E - \frac{1}{r} \frac{\partial}{\partial r} r \alpha v E - \frac{\partial}{\partial z} \alpha p u - \frac{1}{r} \frac{\partial}{\partial r} r \alpha p v - p \frac{\partial \alpha}{\partial t} \\ & - q_p - (f_z u_p + f_r v_p) / g_o + \dot{m} \left[ e_p + \frac{p}{\rho_p} + \frac{u_p^2 + v_p^2}{2 g_o} \right] + \dot{m}_{ig} e_{ig} \quad , \quad 2.2.4 \end{aligned}$$

where  $E = \rho \left( e + \frac{u \cdot u}{2 g_o} \right)$  and  $g_o$  is used to reconcile units and we use a subscript  $p$  to denote a property of the solid propellant which constitutes the discrete phase. Also  $\dot{m}$  and  $q_p$  are respectively the rates of mass and heat transfer per unit volume while  $f_z$  and  $f_r$  are the components of the interphase drag. We use

$\dot{m}_{i8}$  to denote the rate of addition of a source term per unit volume and  $e_{i8}$  represents the chemical energy of the source.

As we will discuss further, in Chapter 3.0, these Equations are integrated using the one-dimensional solver LCPFCT which assumes that the system is timesplit into an axial set

$$\frac{\partial \alpha \rho}{\partial t} = - \frac{\partial}{\partial z} \alpha \rho u + \dot{m} + \dot{m}_{i8} \quad , \quad 2.2.5$$

$$\frac{\partial \alpha \rho u}{\partial t} = - \frac{\partial}{\partial z} \alpha \rho u u - \alpha g_o \frac{\partial p}{\partial z} + \dot{m} u_p - f_z \quad , \quad 2.2.6$$

$$\frac{\partial \alpha \rho v}{\partial t} = - \frac{\partial}{\partial z} \alpha \rho v u \quad , \quad 2.2.7$$

$$\begin{aligned} \frac{\partial \alpha E}{\partial t} = & - \frac{\partial}{\partial z} \alpha u E - \frac{\partial}{\partial z} \alpha \rho u - p \frac{\partial \alpha}{\partial t} - q_p - (f_z u_p + f_r v_p) / g_o \\ & + \dot{m} \left[ e_p + \frac{p}{\rho_p} + \frac{u_p^2 + v_p^2}{2 g_o} \right] + \dot{m}_{i8} e_{i8} \quad , \end{aligned} \quad 2.2.8$$

and a radial set

$$\frac{\partial \alpha \rho}{\partial t} = - \frac{1}{r} \frac{\partial}{\partial r} r \alpha v \quad , \quad 2.2.9$$

$$\frac{\partial \alpha \rho u}{\partial t} = - \frac{1}{r} \frac{\partial}{\partial r} r \alpha \rho u v \quad , \quad 2.2.10$$

$$\frac{\partial \alpha \rho v}{\partial t} = - \frac{1}{r} \frac{\partial}{\partial r} r \alpha \rho v v - \alpha g_o \frac{\partial p}{\partial r} + \dot{m} v_p - f_r \quad , \quad 2.2.11$$

$$\frac{\partial \alpha E}{\partial t} = - \frac{1}{r} \frac{\partial}{\partial r} r \alpha v E - \frac{1}{r} \frac{\partial}{\partial r} r \alpha p v \quad . \quad 2.2.12$$

The balance equations for the discrete phase - the aggregate of granular propellant - may be restated in the present context as follows. Equation 2.1.6 becomes

$$\frac{\partial}{\partial t} (1 - \alpha) + \nabla \cdot [(1 - \alpha) \mathbf{u}_p] = - \frac{\dot{m}}{\rho_p} \quad . \quad 2.2.13$$

Equation 2.1.7 may be simplified with the help of 2.1.6 and the assumption that  $\sigma_{d_i}$  is isotropic to yield

$$\rho_p (1 - \alpha) \frac{D \mathbf{u}_p}{D t_p} = - g_o (1 - \alpha) \nabla p - g_o \nabla \sigma + f \quad , \quad 2.2.14$$

where  $D/Dt_p$  is the convective derivative along the propellant streamline. We do not express 2.2.13 and 2.2.14 in cylindrical coordinates because, as we discuss in Chapter 3.0, they are solved in a Lagrangian formulation for which 2.2.14 is the natural expression. We note that  $\sigma$  in Equation 2.2.14 corresponds to  $\alpha_{d_i} \langle \sigma_{d_i} \rangle$  in Equation 2.1.7.

### 2.3 Constitutive Laws

Closure of the balance equations requires equations of state for the continuous phase and the discrete phase as well as correlations to describe the interphase transfer processes - heat transfer, drag and combustion - together with laws to determine the morphology of the discrete phase - the surface area and volume of the particles. In general, the laws chosen here are a subset of those used in current versions of the TDNOVA Code (Gough, 1983).

### 2.3.1 Equation of State of Continuous Phase

It is assumed that the continuous phase obeys the covolume equation of state

$$e = c_v T = \frac{p(1 - b\rho)}{(\gamma - 1)\rho} \quad 2.3.1.1$$

where  $b$  is the covolume,  $\gamma$  is the ratio of specific heats and  $c_v$  is the specific heat at constant volume.

The molecular weight and the ratio of specific heats are assumed to be constant and are given values appropriate to the fully reacted propellant.

### 2.3.2 Equation of State for Discrete Phase (Intergranular Stress Law)

The intergranular stress is taken to depend on porosity and also on the direction of loading. We embed the constitutive law into the formula for the rate of propagation of intergranular disturbances

$$a(\epsilon) = \left[ -\frac{g_o}{\rho_p} \frac{d\sigma}{d\alpha} \right]^{1/2} \quad 2.3.2.1$$

We may recast 2.3.2.1 into a form more suitable for numerical integration, namely

$$\frac{D\sigma}{Dt_p} = -\rho_p \frac{a^2}{g_o} \frac{D\alpha}{Dt_p} \quad 2.3.2.2$$

In order to formulate the functional behavior of  $a(\alpha)$  we introduce  $\alpha_o$ , the settling porosity of the bed, and values of  $a(\alpha)$  equal to  $a_1$  and  $a_2$  which respectively correspond to loading at  $\alpha_o$  and to unloading/reloading. The nominal loading curve, corresponding to monotonic compaction of the bed from  $\alpha_o$  to a smaller value of the porosity  $\alpha$  is given by

$$\sigma = \sigma_{nom}(\alpha) = \rho_p \frac{a_1^2}{g_o} \alpha_o^2 \left( \frac{1}{\alpha} - \frac{1}{\alpha_o} \right) \quad 2.3.2.3$$

The functional dependence of  $a(\alpha)$  may now be stated as:

$$a(\alpha) = \begin{cases} a_1 \alpha_0 / \alpha & \text{if } \dot{\alpha} \leq 0, \sigma = \sigma_{nom}, \alpha \leq \alpha_0 \\ a_2 & \text{if } 0 \leq \sigma < \sigma_{nom}, \alpha \leq \alpha_0 \\ & \text{or if } \dot{\alpha} > 0, \sigma = \sigma_{nom}, \alpha \leq \alpha_0 \\ 0 & \text{if } \sigma = 0 \text{ and } \dot{\alpha} > 0 \text{ or if } \alpha > \alpha_0 \end{cases} \quad 2.3.2.4$$

where we understand  $\dot{\alpha}$  to mean  $D\alpha/Dt_p$ .

### 2.3.3 Discrete Phase Morphology (Form Functions)

It is assumed, in the present study, that the propellant grains are multi-perforated cylinders having initial length  $L_0$ , external diameter  $D_0$  and perforation diameter  $d_0$ . Until such time as slivering occurs, that is to say the time at which the regressing perforation surfaces intersect, the surface area and volume are given by

$$S_p = \pi(L_0 - 2d)[(D_0 - 2d) + N(d_0 + 2d)] + \pi/2[(D_0 - 2d)^2 - N(d_0 + 2d)^2] \quad 2.3.3.1$$

$$V_p = \pi(L_0 - 2d)[(D_0 - 2d)^2 - N(d_0 + 2d)^2]/4 \quad 2.3.3.2$$

where  $N$  is the number of perforations and  $d$  is the total linear surface regression, assumed uniform over all the surfaces of a grain.

Once slivering occurs, the form functions become rather complicated for  $N > 1$ . Formulas for the form functions following the slivering of seven-perforation grains may be found in Krier et al (1973). The present version of the code supports single-, seven- and nineteen- perforations grains in the propelling charge.

#### 2.3.4 Interphase Drag

We express the interphase drag in a granular bed in the following form (Gough, 1983)

$$\hat{f}_s = \frac{1 - \alpha_e}{D_{pe}} \left( \frac{\alpha}{\alpha_e} \right)^3 \rho |u - u_p| (u - u_p) \hat{f}_s \quad . \quad 2.3.4.1$$

Equation 2.3.4.1 refers to the exterior voidage,  $\alpha_e$ , and the effective diameter,  $D_{pe}$ , based on the exterior volume and surface area computed as though the perforations were not present.

$$\hat{f}_s = \begin{cases} C \hat{f}_{s,RG} & \text{if } \epsilon_e \leq \epsilon_{e0} \quad , \\ \max \left[ C \hat{f}_{s,RG} \left( \frac{1 - \epsilon_e}{1 - \epsilon_{e0}} \frac{\epsilon_{e0}}{\epsilon_e} \right)^{0.45}, \hat{f}_{min} \right] & \text{if } \epsilon_{e0} < \epsilon \leq 1 \quad , \end{cases} \quad 2.3.4.2$$

$$C = \begin{cases} 0.85 & \text{if the grain is perforated and unignited} \quad , \\ 1.0 & \text{otherwise} \quad , \end{cases} \quad 2.3.4.3$$

$$\hat{f}_{min} = \begin{cases} 0.3 & \text{for spheres} \quad , \\ 0.75 & \text{for cylinders} \quad , \end{cases} \quad 2.3.4.4$$

$$\hat{f}_{s,RG} = 2.50 \text{Re}_p^{-0.081} \lambda^{2.17} \quad , \quad 2.3.4.5$$

$$\text{Re}_p = \rho_f \frac{|u - u_p|}{\mu_f} D_{pe} \quad , \quad 2.3.4.6$$

$$\lambda = \begin{cases} 1 & \text{for spheres} \\ (1/2 + L/D)/(3L/2D)^{2/3} & \text{for cylinders} \end{cases} \quad 2.3.4.7$$

We have used  $\alpha_{s_0}$  as the value of  $\alpha_s$  in the settled condition of the bed, L as the length of a cylindrical grain and D as its diameter, and  $\rho_f$  and  $\mu_f$  as the density and viscosity of the gas at the film temperature.

### 2.3.5 Interphase Heat Transfer

The interphase heat transfer, in both the propelling charge and the centercore ignition charge is assumed to be governed by the empirical correlation of Gelperin and Einstein (1971). We express the heat transfer in the form

$$Nu_p = 0.4 Pr^{1/3} Re_p^{2/3} \quad , \quad 2.3.5.1$$

where

$$Nu_p = hD_p/k_f \quad ,$$

$$Re_p = \rho_f |u - u_p| D_p / \mu_f \quad ,$$

$$h = q / (T - T_p) \quad ,$$

where h is the film coefficient and q is the heat transfer per unit surface area. The subscript f denotes an evaluation of properties at the film temperature  $(T + T_p)/2$  where T and  $T_p$  are respectively the continuous phase bulk average temperature and the particle surface average temperature. The viscosity is taken to have a Sutherland-type dependence on temperature,

$$\mu = 0.134064 \frac{(T/298)^{1.5}}{T + 110} \quad . \quad 2.3.5.2$$

The thermal conductivity follows from the Prandtl number which is assumed to satisfy

$$Pr = \frac{c_p \mu}{k} = \frac{4\gamma}{9\gamma - 5} \quad . \quad 2.3.5.3$$

The heat transfer per unit volume  $q_p$  is related to  $q$  according to

$$q_p = (1 - \alpha) \frac{S_p}{V_p} q \quad . \quad 2.3.5.4$$

### 2.3.6 Solid Phase Surface Temperature

Assuming that ignition is an essentially uniform event with respect to the surface of each grain of either the propelling charge or the centercore ignition charge and supposing that the temperature distribution within the solid phase can be captured by a cubic profile, leads to the following expression for the surface temperature

$$T_p = T_{p0} - \frac{2}{3} \frac{hH}{k_p} + \left[ \left( T_{p0} - \frac{2}{3} \frac{hH}{k_p} \right)^2 + \frac{4}{3} \frac{hTH}{k_p^2} - T_{p0}^2 \right]^{1/2} \quad , \quad 2.3.6.1$$

where  $T_{p0}$  is the initial surface temperature and  $H$  satisfies

$$\frac{DH}{Dt_p} = \alpha_p q \quad . \quad 2.3.6.2$$

### 2.3.7 Ignition and Combustion

Ignition is assumed to occur when the surface temperature exceeds a pre-determined value. The rate of surface regression is given by

$$\frac{Dd}{Dt_p} = B_1 + B_2 P^n \quad . \quad 2.3.7.1$$

It should be noted that only one of 2.3.6.2 and 2.3.7.1 has to be solved at each point according as the temperature is less than or equal to the ignition temperature.

The mass transfer per unit volume,  $\dot{m}$ , is related to the regression rate  $\dot{d}$  according to

$$\dot{m} = (1 - \alpha) \frac{S_p}{V_p} \dot{d} \quad . \quad 2.3.7.2$$

#### 2.4 Boundary Conditions and Projectile Motion

For the continuous phase we impose slip boundary conditions at all bounding surfaces. For the discrete phase we admit the possibility of separation from an external boundary so that the appropriate condition is one of non-penetration.

The projectile is assumed to move as a rigid body subject to the total force on its base and the surface of an afterbody, if present, and the resistance due to interactions with the gun tube. The latter may be expressed in a variety of forms. Appendix B may be consulted.

### 3.0 METHOD OF SOLUTION

As we have already noted, we have selected the Flux-Corrected Transport Algorithm LCPFCT (Boris et al, 1993) as the basis for the continuum flow solver. In Section 3.1 we briefly summarize the algorithm and note its application at boundary points and its treatment of multidimensional flows. In Section 3.2 we turn to the problem of non-uniform boundary geometry. We discuss the use of the Virtual Cell Principle (Landsberg et al, 1993) as a means of accommodating arbitrary boundary geometries within a uniform, structured, rectangular mesh. We compare the Virtual Cell approach with the method ultimately adopted in the NGEN Code, namely one in which the actual boundary cell geometry is used and the solution stabilized by a characteristic analysis of the boundary values. The comparison is made in the context of one-dimensional flow. In Section 3.3 we discuss the implementation of the characteristic based boundary analysis for two-dimensional flow. In Section 3.4 we discuss the Large Particle Integrator.

#### 3.1 Summary of LCPFCT Algorithm

LCPFCT is a one-dimensional solver for a canonical balance equation in the form

$$\frac{\partial \rho}{\partial t} = - \frac{1}{r^{k-1}} \frac{\partial}{\partial r} (r^{k-1} \rho v) - \frac{1}{r^{k-1}} \frac{\partial}{\partial r} (r^{k-1} D_1) + C_2 \frac{\partial D_2}{\partial r} + D_3 \quad 3.1.1$$

where  $k = 1, 2$  or  $3$  for planar, cylindrical and spherical flows respectively. Here  $\rho$  is the transported variable and  $D_1, D_2$  and  $D_3$  are referred to as source terms.

The computational domain is decomposed into  $N$  cells. The state variable  $\rho_i$  is considered to apply to the center of the  $i$ -th cell. The cell has volume  $\Lambda_i$  and is bounded by surfaces whose areas are  $A_{i-1/2}$  and  $A_{i+1/2}$  and which are presumed to be orthogonal to the fluid streamline. Fluid properties on the cell boundaries are determined by averaging with the values in adjacent cells.

The fluid velocity at the right hand boundary of cell  $i$  is  $v_{i+1/2}^f$  while the velocity of the boundary is  $v_{i+1/2}^s$ . We define  $\Delta v_{i+1/2} = v_{i+1/2}^f - v_{i+1/2}^s$ .

Equation 3.1.1 is integrated according to a finite volume formulation via several steps in which strong diffusion is first introduced and then subsequently canceled by antidiffusion to the maximum extent consistent with the minimal requirements of computational stability and the condition that the antidiffusion not introduce new maxima or minima in the updated distribution of  $\rho$ . Properties at the beginning of the timestep are denoted by superscript  $o$  while updated properties are denoted by superscript  $n$ .

We first discuss the scheme for non boundary points. The treatment of boundary points is taken up subsequently. First  $\rho$  is transported over timestep  $\Delta t$  to define

$$\Lambda_i^o \rho_i^* = \Lambda_i^o \rho_i^o - \Delta t \rho_{i+1/2}^o A_{i+1/2} \Delta v_{i+1/2} + \Delta t \rho_{i-1/2}^o A_{i-1/2} \Delta v_{i-1/2} \quad 3.1.2$$

Next, the effect of the source terms is added to define  $\rho^T$  according to

$$\begin{aligned} \Lambda_i^o \rho_i^T = & \Lambda_i^o \rho_i^* + \frac{\Delta t}{2} A_{i+1/2} (D_{1,i+1} + D_{1,i}) - \frac{\Delta t}{2} A_{i-1/2} (D_{1,i} + D_{1,i-1}) \\ & + \frac{\Delta t}{4} C_{2,i} (A_{i+1/2} + A_{i-1/2}) (D_{2,i+1} - D_{2,i-1}) + \Delta t \Lambda_i^o D_{3,i} \end{aligned} \quad 3.1.3$$

Except for the influence of the change in cell volume from  $\Lambda_i^o$  to  $\Lambda_i^n$ , Equations 3.1.2 and 3.1.3 represent the discretization of Equation 3.1.1 according to a finite volume formulation. The effect of the change in cell volume is combined with a strongly diffusive process according to

$$\Lambda_i^n \bar{\rho}_i = \Lambda_i^o \rho_i^T + \nu_{i+1/2} \Lambda_{i+1/2} (\rho_{i-1}^o - \rho_i^o) - \nu_{i-1/2} \Lambda_{i-1/2} (\rho_i^o - \rho_{i-1}^o) \quad 3.1.4$$

where  $\Lambda_{i+1/2} = \frac{1}{2} (\Lambda_{i+1}^n + \Lambda_i^n)$  and  $\nu$  is a coefficient of numerical diffusion.

Finally, as discussed by Boris et al (1993), flux-corrected antidiffusive fluxes are computed and the final updated value of  $\rho$  is given by

$$\rho_1^n = \bar{\rho}_1 - \frac{1}{\Lambda_1^n} \left[ f_{1+1/2}^c - f_{1-1/2}^c \right] \quad . \quad 3.1.5$$

Boundary conditions are supplied at  $r_{1/2}$  and  $r_{N+1/2}$ . These are formulated in conjunction with guard cells located outside the boundary so that the integration of boundary cells can be performed using essentially the same code as that which is used for the interior cells. In general LCPFCT expects the user to specify the boundary motion and sets the left hand boundary velocity difference

$$\Delta v_{1/2} = v_{1/2}^f - \left( r_{1/2}^n - r_{1/2}^o \right) / \Delta t \quad , \quad 3.1.6$$

and  $\Delta v_{N+1/2}$  is defined analogously. For nonperiodic boundary conditions the guard cell value  $\rho_0$  is permitted to take the general form

$$\rho_0 = B_1 \rho_1 + B_2 \quad , \quad 3.1.7$$

where  $B_1, B_2$  are set by the user. The right hand guard cell value  $\rho_N$  is defined analogously. The report by Boris et al (1993) may be consulted for a general discussion of the choices of  $B_1$  and  $B_2$  for a variety of boundary types.

As discussed by Boris et al (1993) LCPFCT may be made second order accurate in time by using a two-step scheme, first integrating from  $t$  to  $t + \Delta t/2$  and then from  $t$  to  $t + \Delta t$  using the intermediate values to define the geometric terms and the source terms. Further, LCPFCT is applied to multidimensional situations by timesplitting, integrating first in one direction and then another with the appropriate subsets of the multidimensional equations.

Then referring to the timesplit system of equations for the continuous phase, Equations 2.2.5 - 2.2.12, it is easy to see that each of these is of the form of Equation 3.1.1 with the proper choices of  $\rho, D_1, D_2, D_3$  and  $k$ . However, while a natural set of choices for the fluxes would be  $\alpha\rho, \alpha\rho u, \alpha\rho v$

and  $\alpha E$ , we have elected to use  $\rho$ ,  $\rho u$ ,  $\rho v$  and  $E$ , folding the influence of the porosity  $\alpha$  into the metric quantities  $\Lambda_{1,1/2}$  and  $A_{1,1/2}$ . This selection yields generally smooth thermodynamic state variables and minimizes the influence of the diffusive step defined by Equation 3.1.4.

As for the selection of guard cell values, Equation 3.1.7, we are concerned here only with impermeable boundaries with slip. We note that when the boundary is impermeable the guard cell values only affect the diffusion terms. We therefore use the simplest choices of  $B_1$  and  $B_2$ , namely those which provide even reflection of the thermodynamic properties and the tangential velocity and odd reflection of the normal velocity relative to the boundary.

### 3.2 Treatment of Non-Uniform Geometry

It is immediately obvious how to use LCPFCT to integrate multidimensional flows on domains whose boundaries are rectangular and conformal with the coordinate surfaces of a Cartesian grid. Here we consider the application of the method to non-uniform geometry.

Much progress has been made in recent years with regard to the analysis of flows with arbitrary complex three-dimensional boundary conditions. Methods based on unstructured meshes have been shown to be especially powerful for addressing complex geometries, see for example Lohner (1989), but do not adapt well to massively parallel computing systems. The popular mapping algorithms of the type discussed by Thompson et al (1985) achieve block structured arrays, but are not as flexible as the unstructured mesh algorithms. Moreover, these methods result in non-uniform mesh lines which introduce computational errors through the need to resolve accurately the metric derivatives associated with the transformation. The non-uniformity can also result in regions where the mesh is unnecessarily crowded with the result that the timestep is reduced in order to satisfy the stability condition for an explicit integration scheme.

Recently, Landsberg et al (1993) have suggested an alternative to these boundary fitted mesh algorithms. They suggest the use of a simple rectangular mesh which covers a superset of the computational domain and extends past the

physical boundaries in various locations. Cells are either open, closed or partially obstructed according as they lie inside the boundaries, outside the boundaries or over the boundaries. Only the partially obstructed cells require special treatment. According to Landsberg et al, accurate solutions can be obtained provided that the partially obstructed cells are characterized by correct values of volume, face area and the normal vector to the physical boundary. The normal vector is used to determine the flux-coupling which results when the balance equations are timesplit as discussed previously. Since the cell faces are formally located the same distance apart as those which are open, the stability condition does not demand a reduced timestep. Some distortion of the flow is expected near the boundary since the interpolation of flow properties is not consistent with the fraction of the cell which is actually inside the computational domain. As discussed by Landsberg et al, sufficiently accurate characterizations of cell volume, surface area and average normal vector can be determined by subdividing the boundary cell into "virtual cells" whose purpose is simply to establish these metric data and for which state variables are never determined.

In the present application, the metric data can be determined by simple analytical formulas, so that cell subdivision is not required. Nevertheless, we will refer to the partially obstructed cells whose boundaries lie outside the computational domain as virtual cells.

The Virtual Cell Principle has the advantages that it allows easy parallelization of the algorithm, complete flexibility with regard to boundary geometry, minimal additional computation at the boundaries, and freedom from the expense and possible inaccuracies associated with the computation of non-uniform mesh transformation derivatives.

Accordingly, we examine the applicability of the Virtual Cell Principle to the NGEN Code, using as a baseline the analytical solution of Love and Pidduck (1921) of the well-known Lagrange problem.

At the same time we evaluate an alternative procedure for the boundary cells. We again take the mesh to be orthogonal and rectangular. Cells are



For this simple one-dimensional flow the appropriate characteristic condition may be stated as (Courant and Hilbert, 1953)

$$\frac{\partial p}{\partial t} = - (u + c) \frac{\partial p}{\partial z} - \frac{\rho c}{g_0} \left( \frac{\partial u}{\partial t} + (u + c) \frac{\partial u}{\partial z} \right) \quad 3.2.1$$

which is appropriate at the right hand boundary, the base of the projectile. At that location  $\partial u/\partial t$  is known from the motion of the projectile. The spatial derivatives  $\partial p/\partial z$  and  $\partial u/\partial z$  can be discretized using the old data at cell  $N - 1$  and the old boundary values, the boundary value of pressure being determined by extrapolation as shown in Figure 3.1. Then 3.2.1 allows the determination of the characteristic based value of pressure at the new time.

The benchmark problem used for the evaluation of the two methods entails motion of a projectile through a cylindrical tube due to the expansion of a region of pressurized gas. An analytical solution was obtained by Love and Pidduck for specific conditions (1921) and has been used as a benchmark in the evaluation of other interior ballistic codes (Schmitt, 1981; Robbins, 1983). The tube diameter is 15 cm. The initial length of the gas column is 169.8 cm and the projectile travel is 600 cm. The projectile mass is 50 kg. The initial pressure and temperature of the gas are 621.09 MPa and 2666.8 K. The gas has molecular weight 23.8 g/gmol, covolume 1.0 cm<sup>3</sup>/g and ratio of specific heats equal to 1.22.

To examine the influence of the fraction of a cell outside the boundary we construct an accordion mesh which expands with the projectile and allows a fraction  $OUTFR$  of the last cell to be in front of the projectile. Here  $OUTFR = 1 - \zeta$  where  $\zeta$  is as shown in Figure 3.1. We obtained solutions with 15, 30 and 60 cells and various values of  $OUTFR$  ranging from 0 (cell completely inside) to 0.99 (cell almost completely outside). Guard cell values, Equation 3.2.7, were chosen to give symmetry in the density and energy and antisymmetry in the velocity.

It was found that both methods provided results at muzzle exit which were in good agreement with the analytical solution, with the physical element

analysis being somewhat better, especially for large values of OUTFR, as might be expected. However, early in the solution, the virtual cell analysis produced large wiggles and errors in the boundary values. Following some review, it was found that by replacing the velocity  $v_N$  by an interpolation between  $N - 1$  and the boundary, more stable results could be obtained. This measure could have been made contingent on OUTFR, but for simplicity was adopted uniformly. It was also applied to the characteristic based method where it had a slightly beneficial effect in that it eliminated a pressure wiggle of magnitude about 1% near the forward boundary.

The results at muzzle exit obtained with the two methods following the foregoing revision are presented in Tables 3.1 and 3.2. Except for the case with NCELL = 15 and OUTFR = 0.99, the virtual cell analysis does very well. The characteristic based method actually shows a larger disparity from the analytical prediction of base pressure. We note however, that the results for the physical element are almost identical to those obtained with TDNOVA (Robbins, 1983); namely; exit time, 10.58 ms; velocity, 808.5 m/s; and base pressure, 54.41 MPa.

Although the characteristic based method involved additional computation near the boundary, the effect on run time was not large. For the virtual element analysis the CPU times on a Silicon Graphics Personal Iris workstation were 0.5, 2.0 and 7.3 seconds for 15, 30 and 60 cells, while for the characteristic based method the times were 0.6, 2.0 and 7.3 seconds.

Based on the results of Tables 3.1 and 3.2 there would seem to be no reason not to use the virtual cell analysis. However, inspection of the solution at earlier times shows that this method, even with the value of  $v_N$  overwritten, may still produce significant errors. We refer to Table 3.3. which presents results at 0.4772 ms. At this early time the characteristic based method is in close agreement with the analytical solution while the virtual element analysis exhibits errors as large as 7.6%, and these errors do not decrease as NCELL is increased. The fact that the final values are as good as they are is a tribute to the stabilizing power of the LCPFCT algorithm.

Table 3.1. Comparison of LCPFCT solution with virtual cell embedding to that of Love and Pidduck (1921) for Lagrange gun problem at muzzle exit. NCELL is the number of cells. OUTFR is the fraction of the last cell in front of the projectile base. The Courant number is 0.5.

Method	NCELL	OUTFR	Exit Time (msec)	% Diff	Velocity (m/s)	% Diff	Base Pressure (MPa)	% Diff
Analytic	-	-	10.58	-	807.7	-	54.19	-
LCPFCT	15	0.00	10.55	-0.28	809.8	0.26	54.43	0.44
		0.25	10.56	-0.19	809.4	0.21	54.42	0.42
		0.50	10.56	-0.19	809.2	0.19	54.42	0.42
		0.75	10.56	-0.19	809.1	0.17	54.29	0.18
		0.90	10.57	-0.10	808.9	0.15	54.43	0.44
		0.99	10.58	0.00	808.3	0.07	55.33	2.10
LCPFCT	30	0.00	10.56	-0.19	809.2	0.19	54.37	0.33
		0.25	10.57	-0.10	809.0	0.16	54.38	0.35
		0.50	10.57	-0.10	808.9	0.15	54.39	0.37
		0.75	10.57	-0.10	808.8	0.14	54.35	0.30
		0.90	10.57	-0.10	808.7	0.12	54.31	0.22
		0.99	10.58	0.00	808.5	0.10	54.05	-0.26
LCPFCT	60	0.00	10.57	-0.10	808.9	0.15	54.41	0.41
		0.25	10.57	-0.10	808.8	0.14	54.39	0.37
		0.50	10.57	-0.10	808.7	0.12	54.40	0.39
		0.75	10.57	-0.10	808.7	0.12	54.39	0.37
		0.90	10.58	0.00	808.6	0.11	54.36	0.31
		0.99	10.58	0.00	808.5	0.10	54.07	-0.22

Table 3.2. Comparison of LCPFCT solution with characteristic analysis of boundary cell to that of Love and Pidduck (1921) for Lagrange gun problem at muzzle exit. NCELL is the number of cells. OUTFR is the fraction of the last cell in front of the projectile base. The Courant number is 0.5.

Method	NCELL	OUTFR	Exit Time (msec)	% Diff	Velocity (m/s)	% Diff	Base Pressure (MPa)	% Diff
Analytic	-	-	10.58	-	807.7	-	54.19	-
LCPFCT	15	0.00	10.58	0.00	808.5	0.10	54.55	0.66
		0.25	10.57	-0.10	808.6	0.11	54.55	0.66
		0.50	10.58	0.00	808.4	0.09	54.49	0.55
		0.75	10.58	0.00	808.3	0.07	54.42	0.42
		0.90	10.58	0.00	808.3	0.07	54.37	0.33
		0.99	10.58	0.00	808.3	0.07	54.35	0.30
LCPFCT	30	0.00	10.57	-0.10	808.8	0.14	54.51	0.59
		0.25	10.57	-0.10	808.7	0.12	54.50	0.57
		0.50	10.58	0.00	808.6	0.11	54.48	0.54
		0.75	10.58	0.00	808.5	0.10	54.45	0.48
		0.90	10.58	0.00	808.5	0.10	54.43	0.44
		0.99	10.58	0.00	808.5	0.10	54.41	0.41
LCPFCT	60	0.00	10.58	0.00	808.7	0.12	54.46	0.50
		0.25	10.58	0.00	808.7	0.12	54.45	0.48
		0.50	10.58	0.00	808.7	0.12	54.44	0.46
		0.75	10.58	0.00	808.6	0.11	54.42	0.42
		0.90	10.58	0.00	808.6	0.11	54.40	0.39
		0.99	10.58	0.00	808.5	0.10	54.45	0.48

Table 3.3. Comparison of base pressures at 0.4772 ms computed using analytic method of Love and Fidduck (1921) with LCPFCT with virtual cell (VC) and LCPFCT with characteristic method (CM). The fraction of the last cell outside the boundary is 0.99 for both the VC and CM calculations. The Courant number is 0.5.

Method	NCELL	Base Pressure (MPa)	% Diff
Analytic	-	554.2	-
LCPFCT/VC	15	582.1	5.03
	30	544.1	-1.82
	60	512.2	-7.58
LCPFCT/CM	15	554.3	0.02
	30	554.2	0.00
	60	554.1	-0.02

On balance, it appears that the virtual cell analysis could be a satisfactory method under some circumstances, particularly if we treat cells which are almost completely obstructed as closed. However, the characteristic based method does seem to offer greater accuracy and stability without much additional cost. Of course, in a highly parallel computing environment, the additional work at the boundary will slow down the entire calculation at a greater proportional rate than in the present serial calculation. Yet, if the method allows the same degree of accuracy to be achieved with fewer points, considerable savings in run time can be achieved, especially in three-dimensional calculations.

We have selected the characteristic based analysis for the following reasons. Although the present study shows the virtual cell analysis to be satisfactory for all but the most strongly occluded cells we believe that practical limits on mesh size make it desirable to maintain stability for cells which are as much as 99% occluded. Especially when cells are located near an outer radial boundary, they can represent a significant fraction of the total volume. Moreover, the present study has addressed cells whose geometry is essentially stationary. In a two-dimensional application we expect cells to grow or shrink due to relative motion of the external boundaries. Not only is it desirable to follow the history of the flow in a continuous manner as

certain cells shrink to nothing or expand from nothing, we expect additional numerical strain to follow from the change in volume as we approach zero. This latter concern may be understood from an examination of Equation 3.1.4. Finally, we look beyond the present application to the computational challenge presented by the analysis of increment containers. It is expected that a characteristic based method will be of great value in determining the coupled internal boundary values corresponding to the flow on each side of the container.

### 3.3 Characteristic Based Application of LCPFCT to Two-Dimensional Flow with Non-Uniform Boundaries

We begin by discussing the representation of gun and projectile geometry. Figure 3.2 illustrates the embedding of tube and afterbody geometry into a structured rectangular mesh as is presently done in the NGEN Code. It is assumed that the breechface and the base of the projectile/sabot are flat and so is the base of the afterbody if one is present. The tube and afterbody are allowed to have arbitrary geometry as expressed by tables of radii versus axial distance. It is assumed that the structure of the geometry is consistent with the resolving power of the mesh. Also, for the time being, we constrain the geometry so that each axial or radial sweep with LCPFCT involves a simply connected set of cells. This effectively limits the afterbody shape to one in which the radius does not decrease with distance down the tube. This restriction is in no way fundamental and can be removed by the extension of the coding to look for multiple boundary intersections on axial and radial lines.

The axial distribution of cells is such that a fixed uniform complement is spaced between the breechface and the base of the afterbody, if present, and expands in concert with the motion of the projectile. Another fixed uniform complement is attached to the afterbody, if present, and moves with the projectile. The radial distribution is divided into two regions. The cells in the inner region are evenly spaced between the centerline and the outside of the base of the afterbody. The cells in the outer region are evenly spaced between the outside of the base of the afterbody and the largest radius of the chamber.

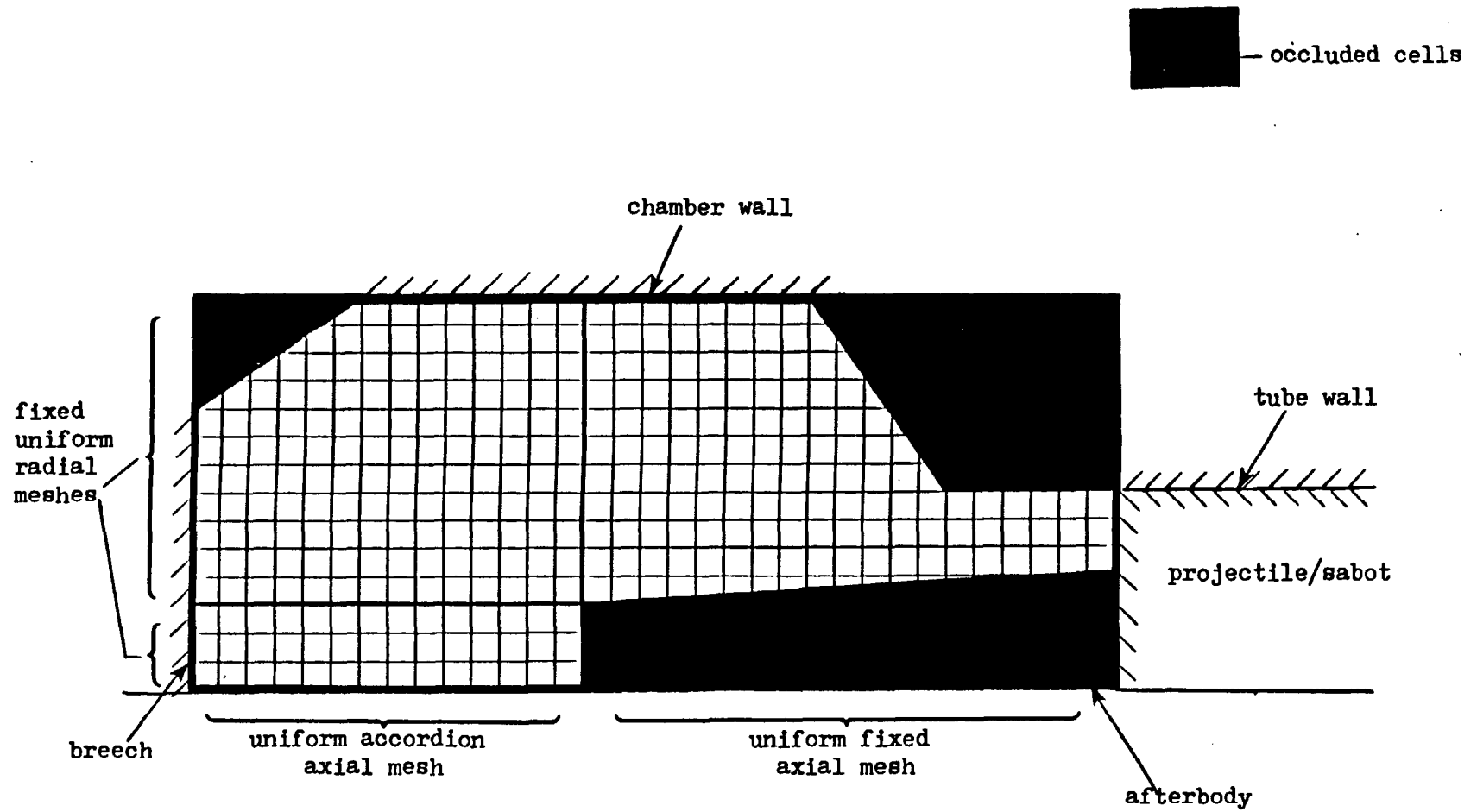


Figure 3.2 Chamber and afterbody geometry as represented in NGEN Code.

If no afterbody is present the distribution is axially uniform from the breech to the base of the projectile and radially uniform from the centerline to the largest chamber radius. When an afterbody is present, motion of the projectile will eventually result in a large difference in axial cell spacing at the base of the afterbody. This could be avoided by the introduction of coding to increase the number of cells behind the afterbody from time to time.

At each time step the radial boundaries are scanned for intersections with the array of cells. Cells are marked as open, partially occluded or closed. Closed cells are ignored in the calculation, but they are assigned default state variable values in order to facilitate plotting. Partially occluded cells are assigned values of volume and area fractions which are transmitted to the LCPFCT metric routines to modify the nominal values corresponding to open cells. The volume and area fractions are computed analytically on the assumption that the boundary element is linear across the cell in question.

Because the balance equations are solved in divergence form, it is necessary to impose a geometric conservation law (Thomas and Lombard, 1979). The volume fraction is only computed analytically at the first step. Subsequently it is deduced from an integral of the area fraction times the normal cell face velocity. This eliminates the introduction of a fictitious source term due to inconsistencies between the finite volume and area fractions.

We now indicate how the characteristic analysis is applied to the multidimensional situation with non-uniform boundaries. Cells are first integrated in the axial direction at all radial locations. The integration is performed from the first open or partially occluded cell at each radial position to the last such cell, it being assumed, as noted above, that only one such string exists. Boundary cells adjacent to the flat breechface or projectile/sabot base are always open so that their treatment is straightforward. Boundary cells created by termination by the tube wall or the afterbody may be partially occluded. They are treated after the fashion of the virtual cell analysis described in the previous section. Thus, on the axial sweep, we only account for area and volume fraction.

When the axial sweep is complete at all locations we perform the radial sweep at each axial location. It is at this point that the characteristic analysis is used to stabilize the solution. We use the external boundary position to define the boundaries of the first and last cells to be integrated and we introduce the normal to the boundary in setting the boundary values. The axial velocity component is extrapolated to the wall and the value of radial velocity at the wall is determined from the condition of attachment. This value is then used together with the interior data to compute a characteristic value of boundary pressure which is then compared with the value implied by the LCPFCT integration as in the one-dimensional case discussed previously. Again, mass transfer between the boundary cell and its neighbor is introduced to bring the two values into agreement. The influence of the cross flow terms is taken to be embedded in the LCPFCT axial sweep so that the characteristic analysis is effectively one-dimensional as far as spatial differencing is concerned, thereby minimizing the computational burden.

Appendix A discusses the characteristic analysis of a two-dimensional single phase flow with a non-homogeneous source term. The results contained therein form the basis for the present application since we formally include with the non-homogenous terms the derivative of porosity. Equation A.2.27 is the relevant characteristic form, and we restate it here as

$$\frac{\partial p}{\partial t} + [v - v_m \pm c] \frac{\partial p}{\partial r} \pm \frac{\rho c}{g_o} \left[ \frac{\partial v}{\partial t} + [v - v_m \pm c] \frac{\partial v}{\partial r} \right] = \frac{c^2}{g_o} \xi_A \quad . \quad 3.3.1$$

Now  $\xi_A$  includes the non-homogenous terms and the crossflow (axial) derivatives.

We have  $v_m$  as the radial mesh velocity and  $\xi_A$  is defined by

$$\frac{c^2}{g_o} \xi_A = \frac{c^2}{g_o} \xi_1 \pm \frac{c}{g_o} \xi_3 + \xi_4 \quad , \quad 3.3.2$$

where the  $\xi_i^*$ , including  $\xi_2^*$  which is not coupled, are defined as follows

$$\xi_1^* = \xi_1 - \frac{\partial \rho u}{\partial z} \quad , \quad 3.3.3$$

$$\xi_2^* = \xi_2 - \rho u \frac{\partial u}{\partial z} - g_o \frac{\partial p}{\partial z} \quad , \quad 3.3.4$$

$$\xi_3^* = \xi_3 - \rho u \frac{\partial v}{\partial z} \quad , \quad 3.3.5$$

$$\xi_4^* = \xi_4 - u \frac{\partial p}{\partial z} + \frac{c^2}{g_o} u \frac{\partial \rho}{\partial z} \quad . \quad 3.3.6$$

We write the  $\xi_i$  as  $\xi_{1r} + \xi_{1z}$ ,  $i = 1 - 4$ , to conform with the timesplitting convention. Then we have (Gough, 1983), with the formal representation of the porosity derivative as non-homogeneous

$$\xi_{1z} = \frac{1}{\alpha} \left[ \dot{m} + \dot{m}_{1g} - \rho \left( \frac{\partial \alpha}{\partial t} + u \frac{\partial \alpha}{\partial z} \right) \right] \quad , \quad 3.3.7$$

$$\xi_{1r} = - \frac{\rho v}{r} - \frac{\rho v}{\alpha} \frac{\partial \alpha}{\partial r} \quad , \quad 3.3.8$$

$$\xi_{2z} = \frac{1}{\alpha \rho} \left[ - f_z + \dot{m} (u_p - u) - \psi u \right] \quad , \quad 3.3.9$$

$$\xi_{2r} = 0 \quad , \quad 3.3.10$$

$$\xi_{3z} = \frac{1}{\alpha \rho} \left[ \dot{m} (v_p - v) - \psi v \right] \quad , \quad 3.3.11$$

$$\xi_{3r} = - \frac{f_r}{\alpha \rho} \quad , \quad 3.3.12$$

$$\xi_{4z} = \frac{1}{\alpha \rho \left( \frac{\partial e}{\partial p} \right)_\rho} \left\{ f \cdot (u - u_p) - q_p + \dot{m} \left[ e_p - e + p \left( \frac{1}{\rho_p} - \frac{1}{\rho} \right) + \frac{|u - u_p|^2}{2g_o} \right] \right. \\ \left. + \dot{m}_{1g} \left[ e_{1g} - e - \frac{p}{\rho} + \frac{u \cdot u}{2g_o} \right] \right\} \quad , \quad 3.3.13$$

$$\xi_{4r} = 0 \quad . \quad 3.3.14$$

Now the z-components of  $\xi_A$  can be resolved as the result of the integration of the axial equations of motion including the relevant source terms. This is exactly what occurs on the axial sweep by LCPFCT except that the influence of changing cell volume is also captured. Then, factoring out this term and using a superscript  $\circ$  to denote the result of the axial sweep, Equation 3.3.1 may be discretized at the boundary in the form

$$p_b^n - p_b^\circ + (v - v_b \pm c) \left( \frac{\partial p}{\partial r} \right)^\circ \Delta t \\ = \frac{c^2}{g_o} \xi_{Ar} \mp \frac{\rho c}{g_o} \left[ v^n - v^\circ + (v - v_b \pm c) \left( \frac{\partial v}{\partial r} \right)^\circ \Delta t \right] \\ + \left[ \bar{p}_b - p_b^\circ \pm \frac{\rho c}{g_o} (\bar{v}_b - v_b^\circ) + \frac{\rho c^2}{g_o A} \left( \frac{DA}{Dt} \right) \right] \quad . \quad 3.3.15$$

where  $\xi_{Ar}$  involves only the  $\xi_{1r}$ .

The spatial derivatives are understood to be evaluated using old data. We understand  $DA/Dt$  to be the axial convective derivative of the cell cross-sectional area. This is the only additional term which needs to be differenced. Equation 3.3.15 therefore makes only minimal computational demands.

### 3.4 The Large Particle Integrator (LPI)

We now discuss the LPI which is intended to be applied to those discrete phases which cannot be assumed to be in mechanical equilibrium with the continuous phase. In all cases of practical interest this will include all solid propellant increments.

In previous work (Gough, 1983) we have explained the importance of the presence of ullage in solid-propellant charges and of the properties of the increment containers which are generally present in artillery charges. The initial presence and subsequent persistence of ullage and the permeability and fracture properties of the containers can exert considerable influence over the path of flamespreading and the subsequent ballistic behavior of the charge. Small differences in these attributes can make the difference between a safe charge and one which can destroy the gun (May and Horst, 1979). Therefore, in previous work we have taken a modeling approach based on the representation of charge increment boundaries as explicit discontinuities across which not only the porosity but also the gas-phase properties may jump discontinuously. The increment boundaries were tracked explicitly as part of the numerical solution process. The internal boundary conditions linking the state variables on each side consisted of finite balances of mass, momentum and energy. By viewing the container as a surface attribute of the increment we were able to embed properties of reactivity and permeability into the finite balance equations or jump conditions. Thus our earlier approach not only assured precise tracking of ullage, with a complete elimination of the possibility of contamination through numerical diffusion of the solid propellant properties outside the increment boundary, but it also admitted a representation of the container characteristics on the assumption that the motion of the container was tied to

that of the propellant. Although this approach was successful, it involved a great deal of complex code and grid management and a simpler approach was sought for NGEN.

There is no escaping the complexities associated with the presence of containers. They must be treated as internal boundaries. The approach taken here in respect to the modeling of the continuous phase is thought to anticipate this eventual goal in an appropriate manner. At the same time, the choice of continuum flow solver has been made with a view to the simplification of the representation of the increment boundaries. These are still tracked explicitly via the adoption of a Lagrangian representation of each increment. But the boundaries are not viewed as discontinuities. Instead, the porosity is made to vary continuously over a short distance. Internal jump conditions are not applied. The continuum flow solver is required to be robust enough to integrate the flow in a stable manner in the presence of strong porosity gradients. We have previously shown that LCPFCT meets this requirement (Gough, 1992).

Consider a single charge increment. In the present version of the code its initial distribution is defined by a rear and forward delimiter and by an inner and an outer delimiter. The increment is assumed to occupy uniformly the cylindrical domain defined by these delimiters minus any intrusions by the chamber and afterbody. The increment is then represented by a structured array of LPI-particles. These are arranged in an axially uniform manner from the rear to the forward delimiter and radially from the inner to the outer delimiter. LPI-particles which would lie outside the tube wall or inside the afterbody according to this prescription are then pushed radially to the appropriate radial boundaries. The redundant particles are then assigned zero weight and play no part in the subsequent solution process.

Each particle is assigned a weight as follows. The grain number density  $n_0$  may be computed from

$$n_0 = \frac{M_i}{\rho_p V_p V_i} \quad , \quad 3.4.1$$

where  $M_i$  is the increment mass and  $V_i$  the increment volume and  $\rho_p, V_p,$  are respectively the density of the propellant and the initial volume of an individual grain. Then the number weighting of a particle is taken to be  $n_0$  times the volume of a cylinder defined by the midpoints between the particle and its four neighbors. For boundary particles the relevant midpoint value is replaced by the appropriate axial or radial coordinate of the particle. It is easy to see that this process automatically assigns non-zero weight to at most one particle which was pushed into contact with a radial boundary.

In addition to number weighting, each LPI-particle is assigned the following attributes: axial and radial position and velocity, surface regression, surface temperature and cubic profile thermal parameter (Equation 2.3.6.2), and values of porosity and intergranular stress.

At each time step the equations of motion are integrated using a simple first order time differencing scheme. The positions are updated first for all LPI-particles. Then, in a second sweep the velocities are updated and subjected to the external boundary condition. Depending on the surface temperature either the thermal parameter or the surface regression is integrated. In the same sweep all the interphase transfer properties are computed for each particle and mapped onto the grid for the continuum flow solver together with the porosity distributions.

We now amplify on the previous paragraph. First, with regard to the equation of motion, we see from an inspection of Equation 2.2.14 that we require gradients of pressure and of intergranular stress. These are computed quite differently. The pressure gradient is computed on the continuum mesh by means of central differencing to define cell centered values. Then for each LPI-particle a local value of pressure gradient, together with all other

necessary continuous phase state variables, is computed using linear interpolation in both the radial and the axial directions. The gradient of intergranular stress is computed using differences between the LPI-particles which neighbor the particle in question. One-sided differences are used at boundaries.

We now explain the mapping of LPI data back to the continuum mesh. At each time step each particle is assigned a rectangular domain of influence as follows. Let  $z_L$  and  $z_R$  be the left and right axial delimiters and  $r_i$  and  $r_o$  be the inner and outer delimiters. Then  $z_L$  is set equal to the axial position of the particle to the rear, provided that such a particle exists. If we are at the boundary or if the neighbor in question has zero weight, the  $z_L$  is set equal to a nominal value defined by the user. If this value is less than the position of the rear boundary it is replaced by the position of the boundary. Then  $z_R$ ,  $r_i$  and  $r_o$  are all defined in an analogous manner. Let the coordinates of the particle be  $(z_{ij}, r_{ij})$  and let

$$V_{ij} = \frac{\pi}{8} (z_R - z_L) [(r_{ij} + r_o)^2 - (r_{ij} + r_i)^2] \quad 3.4.2$$

be the volume associated with the particle. This is identical with the procedure used to define the number weighting, except at the boundaries where the definition of the delimiter admits a deliberate extension into the ullage for the purpose of smoothing.

If  $V_{p_{ij}}$  and  $N_{ij}$  are respectively the grain volume and the number weighting, we can define the particle volume fraction

$$\alpha_{ij} = \frac{V_{p_{ij}} N_{ij}}{V_{ij}} \quad , \quad 3.4.3$$

and similarly for the other interphase data such as mass and enthalpy transfer and drag. The value of  $\alpha_{ij}$  so defined is used to update the solid propellant intergranular stress by means of a simple first order time difference.

To assign the LPI-particle volume to the continuum mesh we simply scan the continuum mesh to find those cells whose centers are in the domain of influence. Let  $(z_c, r_c)$  be the coordinates of such a cell center. Define

$$w_z = \begin{cases} (z_R - z_c)/(z_R - z_{1j}) & \text{if } z_c \geq z_{1j} \\ (z_c - z_L)/(z_{1j} - z_L) & \text{if } z_c < z_{1j} \end{cases} \quad , \quad 3.4.4$$

and define  $w_R$  analogously for the radial direction. Then the continuum cell in question is assigned a volume fraction contribution  $w_R w_z \alpha_{1j}$  and similarly for the other interphase properties. These values are summed over all LPI-particles. It is not hard to see that this is tantamount to a bidirectional linear interpolation process.

Some difficulties can arise with this approach when the LPI-particle is close to an external boundary whose shape does not conform well with the rectangular domain of influence. Local pockets of elevated porosity can be produced. This problem is expected to be remedied through minor finessing of the logic to determine the boundaries of the domain of influence in such cases.

A more serious potential problem relates to the behavior of the aggregate as a whole. The presence of the pressure gradient in the solid propellant equation of motion can create a Helmholtz type of instability. Suppose that we have a local minimum of porosity in a macroscopically one-dimensional flow. Porosity affects the gas-phase properties in the same manner as cross-sectional area in a duct. Thus, for subsonic flow, the porosity minimum will be accompanied by a pressure minimum. The pressure gradient will therefore act to drive particles towards the location of the minimum of porosity, deepening it. The process may possibly be stabilized to some extent by interphase drag and certainly by intergranular stresses as the porosity becomes small enough. Nevertheless, strong variations in porosity can and will arise and are inherent in the formulation of the equations. It is not presently known how best to address this problem.

To assign the LPI-particle volume to the continuum mesh we simply scan the continuum mesh to find those cells whose centers are in the domain of influence. Let  $(z_c, r_c)$  be the coordinates of such a cell center. Define

$$w_z = \begin{cases} (z_R - z_c)/(z_R - z_{ij}) & \text{if } z_c \geq z_{ij} \\ (z_c - z_L)/(z_{ij} - z_L) & \text{if } z_c < z_{ij} \end{cases} , \quad 3.4.4$$

and define  $w_R$  analogously for the radial direction. Then the continuum cell in question is assigned a volume fraction contribution  $w_R w_z \alpha_{ij}$  and similarly for the other interphase properties. These values are summed over all LPI-particles. It is not hard to see that this is tantamount to a bidirectional linear interpolation process.

Some difficulties can arise with this approach when the LPI-particle is close to an external boundary whose shape does not conform well with the rectangular domain of influence. Local pockets of elevated porosity can be produced. This problem is expected to be remedied through minor finessing of the logic to determine the boundaries of the domain of influence in such cases.

A more serious potential problem relates to the behavior of the aggregate as a whole. The presence of the pressure gradient in the solid propellant equation of motion can create a Helmholtz type of instability. Suppose that we have a local minimum of porosity in a macroscopically one-dimensional flow. Porosity affects the gas-phase properties in the same manner as cross-sectional area in a duct. Thus, for subsonic flow, the porosity minimum will be accompanied by a pressure minimum. The pressure gradient will therefore act to drive particles towards the location of the minimum of porosity, deepening it. The process may possibly be stabilized to some extent by interphase drag and certainly by intergranular stresses as the porosity becomes small enough. Nevertheless, strong variations in porosity can and will arise and are inherent in the formulation of the equations. It is not presently known how best to address this problem.

#### 4.0 NUMERICAL SOLUTIONS

The operability of the NGEN Code and its general applicability to solid propellant charges are illustrated here by reference to two different data bases. The first of these represents a 155mm howitzer charge and the second represents a 120mm tank gun charge. In both cases we represent the actual geometry of the tube to an extent consistent with the capabilities of the XKTC Code. Thus it is assumed that the breech face and the base of the projectile (or the base of the sabot) are flat. The tube wall geometry is captured as is the geometry of the afterbody in the case of the tank gun simulation.

##### 155mm Howitzer Simulation

The complete NGEN input data file for this problem is presented in Table 4.1. The data base was developed from the one-dimensional XKTC (Gough, 1986) data base for the M203 propelling charge. For simplicity flamespreading is not considered. The charge is taken to be ignited at the initial instant. The discharge from the igniter is ignored and the initial condition corresponds to ambient temperature and pressure. Bore resistance is likewise ignored. The propellant consists of seven-perforation grains with the correct geometry and thermodynamic properties. However, the burn rate is adjusted to give approximately the computed maximum pressure for the original XKTC data base.

The chamber radius is taken to taper linearly with axial distance from a value of 9.17 cm at the breechface to a value of 7.82 cm at the entrance of the tube. In the NGEN simulation the propellant is initially configured with ullage in front of it and around it. The forward boundary delimiter is 75 cm which is less than the position of the projectile base at 82.14 cm. Similarly, the outer radial delimiter is 7.6 cm which is smaller than the tube radius at all locations. Of course, the representation of the charge properties will involve some smearing of the porosity outside the delimiters as discussed in Chapter 3.0.

Table 4.1. Input Data for NGEN Simulation of 155mm Howitzer  
Propelling Charge

CONTROL PARAMETERS

NPRINT(0-NO PRINT,1-PRINT)	1
NSUMRY(0-NO SUMMARY TABLES,1-YES)	1
NPLOT(0-NO ISOMETRIC CARPET PLOTS,1-PLOT)	1
NDSKW(0-NO DISC SAVE,1-DISC SAVE)	0
NDSKR(0-NO DISC START,>0-DISC START AT STEP NDSKR)	0

ISOMETRICALLY PLOTTED QUANTITIES (1-YES,0-NO)

MESH 0 POROSITY 1 GRANULAR STRESS 0 PRESSURE 1  
 DENSITY 0 GAS AXIAL VELOCITY 1 SOLID AXIAL VELOCITY 1  
 GAS RADIAL VELOCITY 1 SOLID RADIAL VELOCITY 1 GAS TEMPERATURE 0  
 PARTICLE SURFACE TEMPERATURE 0

TERMINATION AND LOGOUT PARAMETERS

MAX. STEPS	10000
MAX. TRAVEL(CM)	520.700
STEPS TO LOGOUT	5000
INTERVAL TO LOGOUT(MSEC)	0.500
DEBUG PRINT(0-NO;1-YES)	0

INTEGRATION DATA

COURANT NUMBER(-)	0.500
ANTIDIFFUSIVE FLUX MULTIPLIER	0.999
TOTAL NUMBER OF RADIAL CELLS(-)	8
MINIMUM NUMBER OF AXIAL CELLS BEHIND AFTERBODY	30
MAXIMUM NUMBER OF AXIAL CELLS BEHIND AFTERBODY	30
NUMBER OF AXIAL CELLS ALONG AFTERBODY	0
NUMBER OF RADIAL CELLS AT BASE OF AFTERBODY	0

INITIAL DATA

PRESSURE(MPA)	0.101
TEMPERATURE(K)	294.0
GAMMA(-)	1.2430
MOL.WGT(GM/GMOL)	23.4400
COVOLUME(CM**3/GM)	1.0300

CHARGE REPRESENTATION PARAMETERS

NUMBER OF PROPELLANTS IN CHARGE 1  
 NUMBER OF INCREMENTS IN CHARGE 1  
 PROPELLANT MODEL (1-LP,2-2D) 2

PROPERTIES OF PROPELLANT TYPE 1

SOLID PHASE CONSTITUTIVE DATA

SETTLING POROSITY OF GRANULAR BED(-) 0.40000  
 SPEED OF COMPRESSION WAVE(CM/SEC) 15240.0  
 SPEED OF EXPANSION WAVE(CM/SEC) 127000.0  
 DENSITY OF SOLID PHASE(GM/CC) 1.5830  
 THERMAL CONDUCTIVITY(J/CM-SEC-DEG.K) 0.160100E-02  
 THERMAL DIFFUSIVITY(CM\*\*2/SEC) 0.645160E-03

GAS PHASE CONSTITUTIVE DATA AND PROPELLANT INITIAL TEMPERATURE

RATIO OF SPECIFIC HEATS(-) 1.24300  
 MOLECULAR WEIGHT(GM/GM-MOL) 23.440  
 COVOLUME(CC/GM) 1.030  
 INITIAL TEMPERATURE (DEG.K) 445.0

SOLID PHASE COMBUSTION CHARACTERISTICS

NUMBER OF BURN RATE DATA 2  
 IGNITION TEMPERATURE(DEG.K) 444.4  
 CHEMICAL ENERGY(J/GM) 4384.

MAX. PRESSURE (MPA)	BURN RATE ADDITIVE CONSTANT (CM/SEC)	PRE-EXPONENT (CM/SEC-MPA**BN)	EXPONENT (-)
68.95	0.00000	0.24810	0.78640
689.50	0.00000	0.24810	0.78640

GRAIN GEOMETRY

FORM(0-CYLINDER,1-SPHERE,2-SOLID STICK,  
 3-PERFORATED OR SLOTTED STICK) 0  
 EXTERNAL DIAMETER(CM) 1.060  
 LENGTH(CM) 2.408  
 DIAMETER OF PERFORATIONS(CM) 0.086  
 NUMBER OF PERFORATIONS(-) 7.

PROPERTIES OF INCREMENT NUMBER 1

MAIN CHARGE PROPELLANT TYPE	1
NUMBER OF AXIAL CELLS	30
NUMBER OF RADIAL CELLS	8
MASS OF MAIN CHARGE(G)	11861.4000
REAR BOUNDARY DELIMITER (CM)	0.000
FORWARD BOUNDARY DELIMITER (CM)	75.000
INNER BOUNDARY DELIMITER (CM)	0.000
OUTER BOUNDARY DELIMITER (CM)	7.600

PROPERTIES OF PROJECTILE

INITIAL POSITION OF PROJECTILE/SABOT BASE(CM)	82.140
PROJECTILE MASS(GM)	43181.800
NUMBER OF ENTRIES IN BORE RESISTANCE TABLE	2
RESISTANCE LAW NUMBER	0

N.B. IF <1 OR >3, VALUE WILL DEFAULT TO 2 INTERNALLY

BORE RESISTANCE DATA

PROJECTILE TRAVEL(CM)	RESISTIVE PRESSURE(MPA)
0.000	0.000
600.000	0.000

NUMBER OF TUBE GEOMETRY DATA 3

TUBE GEOMETRY

AXIAL POS(CM)	RADIUS(CM)
0.000E+00	9.17
82.1	7.82
602.	7.82

The continuum mesh is given 8 radial and 30 axial cells. Due to the taper of the chamber, not all cells are open. The charge is represented by 8 radial and 30 axial particles. The maximum Courant number is 0.5.

The distribution of porosity at four times are shown in Figure 4.1. The distribution at  $t = 0$  ms also illustrates the continuum grid, it being understood that the plotted lines correspond to cell centers except on the external boundaries. The initial ullage is apparent from the porosity distribution. We note that the smearing at the boundaries results in a zone of sharply varying but not discontinuous properties. By 4.0 ms the charge has expanded to fill the chamber. By 8.0 ms, which is close to the time of maximum pressure, the porosity is essentially uniform except for the small region of ullage behind the projectile base which is an expected feature of the solution since the propellant grains are expected to lag to a certain extent. By 12.0 ms burnout of the charge is occurring with the process beginning at the breech where the elevated pressure causes more rapid combustion.

Figure 4.2 presents the distributions of pressure at four similar times. It should be noted that the viewpoint is from the tube wall. It is interesting to note how rapidly the pressure equilibrates in the radial direction. The distributions are essentially one-dimensional at all times, including the earliest at 0.5 ms. This is true even though the gas-phase flow field at 0.5 ms, shown in Figure 4.3, is far from one-dimensional. Strong radial convection is associated with the pressurization of the radial ullage by the products of combustion. This is of course strongest near the breech where the radial ullage is most pronounced. At the base of the projectile the suction caused by motion of the projectile dominates the flow which is essentially axial.

As a check on the overall accuracy of the coding, a comparison was made of the NGEN ballistic predictions with those of XKTC. The data bases were made completely consistent except for the representation of the radial ullage in NGEN, a feature absent from XKTC. The agreement is shown in Figure 4.4 and is thought to be satisfactory.

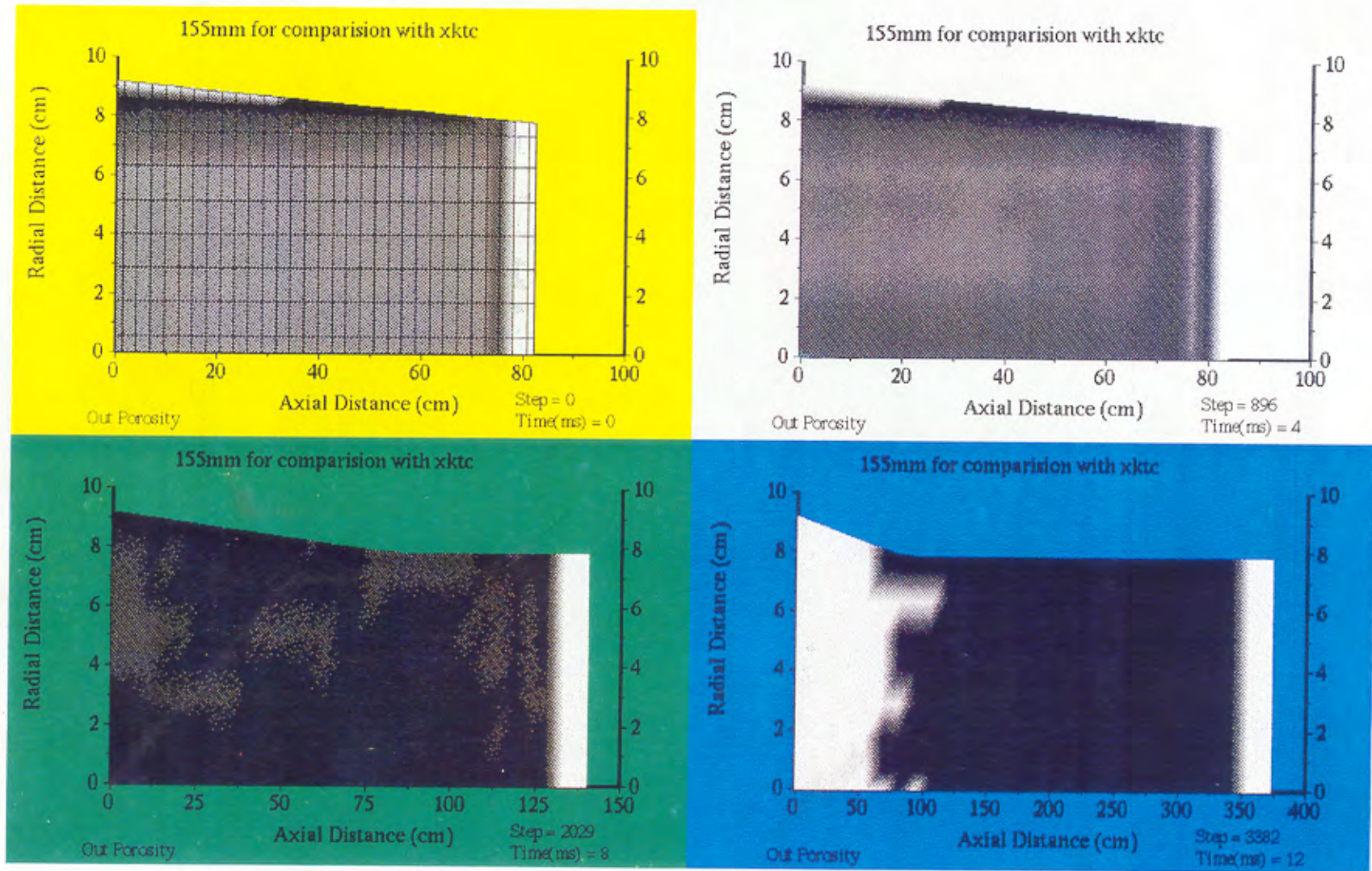
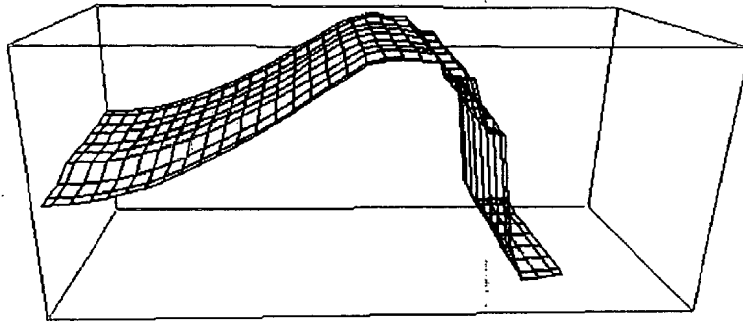


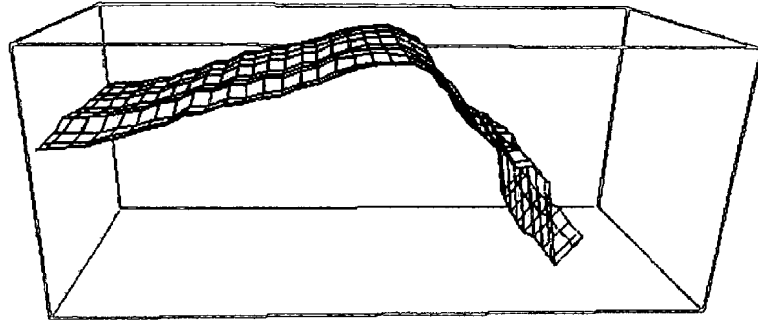
Figure 4.1 Porosity Distributions in 155mm Howitzer at Four times.

155mm for comparison with xkte



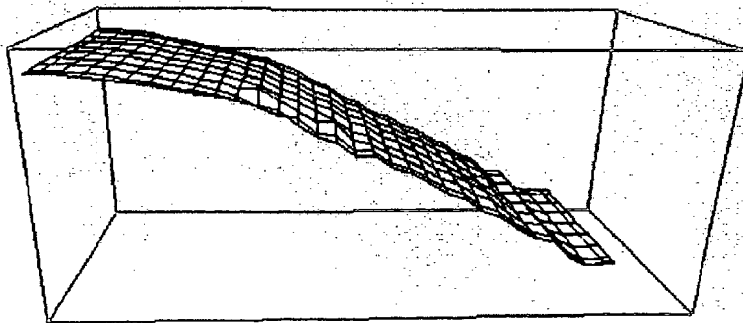
Out Pressure      Step = 66      Min = 0.258586  
Time(ms) = 0.5      Max = 0.539724

155mm for comparison with xkte



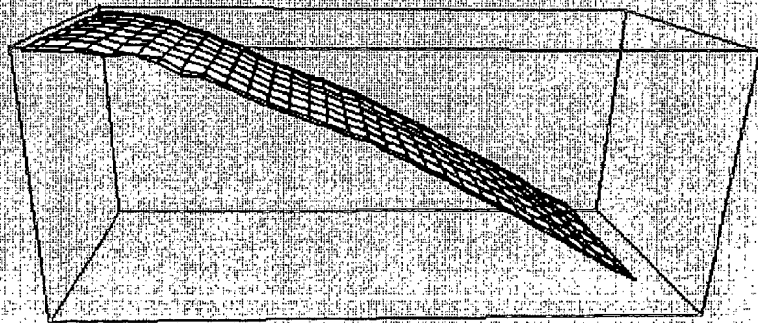
Out Pressure      Step = 775      Min = 32.5994  
Time(ms) = 3.5      Max = 34.5592

155mm for comparison with xkte



Out Pressure      Step = 2192      Min = 295.678  
Time(ms) = 8.5      Max = 344.356

155mm for comparison with xkte



Out Pressure      Step = 3392      Min = 135.698  
Time(ms) = 12      Max = 159.429

Figure 4.2 Pressure Distributions in 155mm Howtizer at Four times.

# ARL CFD SIMULATION / NGEN CODE

## 155mm Gun

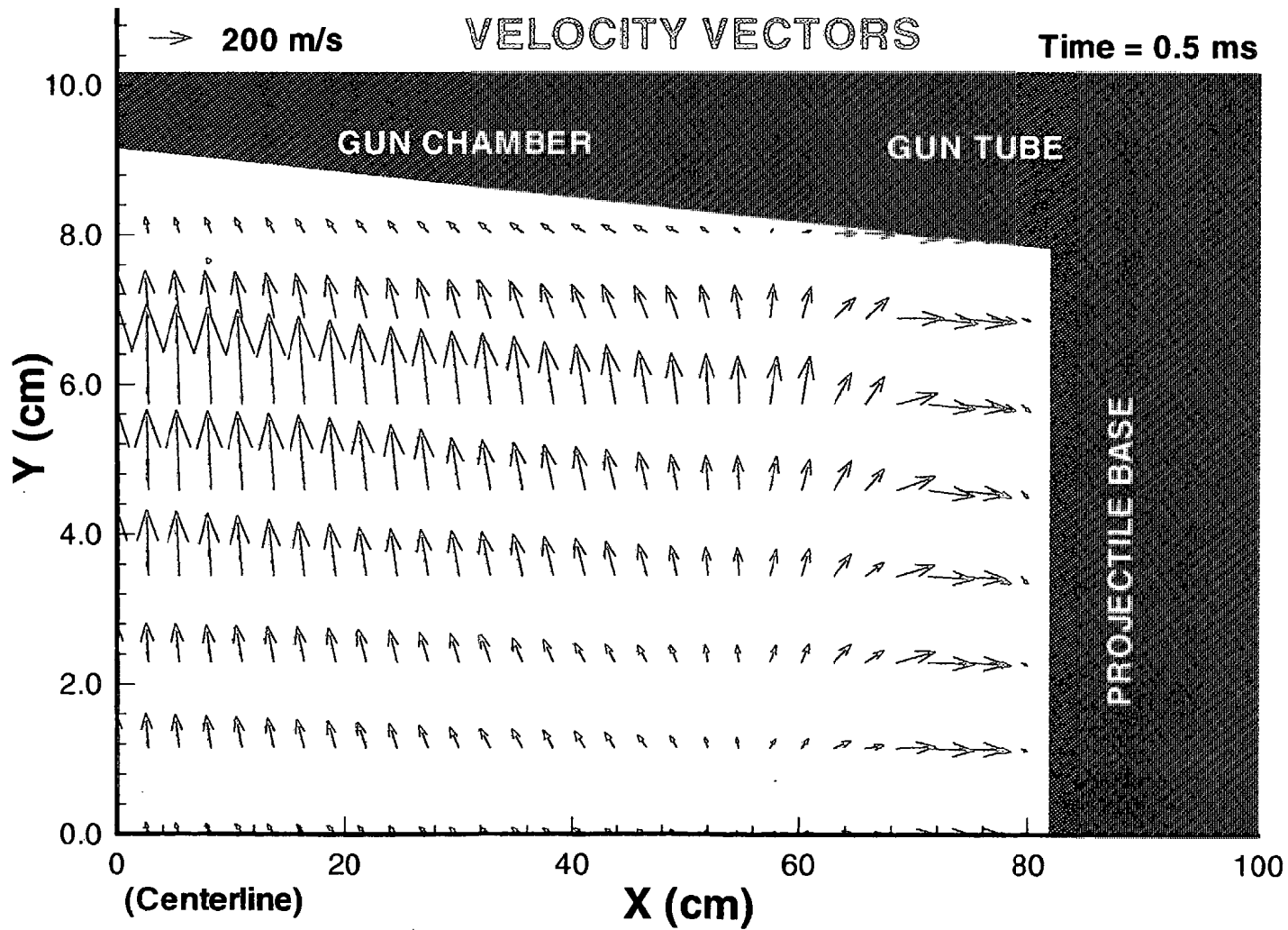


Figure 4.3 Gas-Phase Flow Field in 155mm Howitzer at 0.5 ms.

# ARL CFD Simulation / NGEN Code

## 155mm Gun

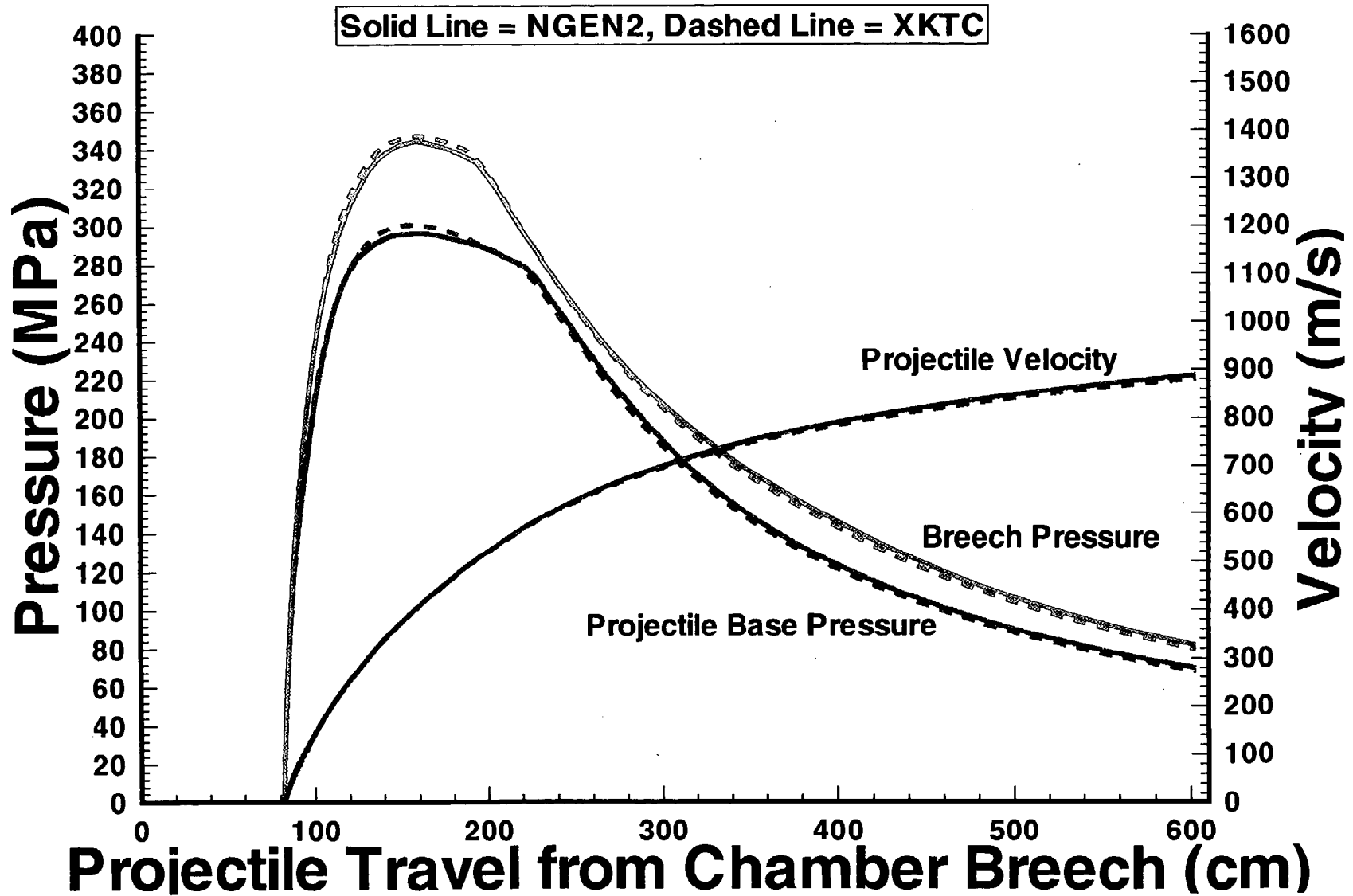


Figure 4.4 Comparison of NGEN and XKTC Ballistic Predictions for 155mm Howitzer.

## 120mm Tank Gun Simulations

The complete NGEN input data file for this problem is presented in Table 4.2. The geometrical data were developed from an XKTC data base for a tank gun round with a strongly intruding afterbody. Apart from the projectile mass, the remaining data are purely nominal. The charge is represented as completely filling the available initial volume. It is taken to be seven perforation granular with burn rate adjusted to give a moderately high pressure of nearly 380 MPa. Flamespreading is neglected, the charge being initially ignited. Likewise, we ignore bore resistance and the possible presence of a combustible cartridge case. The initial pressure is taken to be 6.895 MPa and the temperature is 3009K.

The purpose of the simulation is to test the ability of NGEN to represent the strongly non-uniform boundary geometry typical of tank gun ammunition. The continuum mesh is assigned 10 radial cells, with 3 assigned to the base of the afterbody. A total of 30 axial cells are assigned with 15 behind the afterbody and 15 along the afterbody. Clearly, due to the non-uniform geometry many of the cells are closed. The propellant is represented by 8 radial and 30 axial particles. All the spatial delimiters are set equal to zero. As a default procedure, NGEN takes the propellant to occupy the entire initial volume of the chamber, taking into account the intrusion of the afterbody. As discussed in Chapter 3.0, those particles which would be covered by the external boundaries are assigned zero weight and are not updated in the solution algorithm. The maximum Courant number is 0.5.

Figure 4.5 illustrates the porosity distributions at four times. The distribution at  $t = 0.0$  ms also illustrates the continuum grid. It should be noted that the base of the afterbody is actually flat. The shape of the base shown in the figure is an artifact of the plot interface routine. The figure illustrates clearly the non-uniform nature of the boundary geometry and its representation by a grid which is everywhere rectangular except adjacent to the radial boundaries. The distributions show the gradual separation of the propellant from the base of the sabot and the base of the afterbody. We also

Table 4.2. Input Data for NGEN Simulation of 120mm Tank Gun Charge

CONTROL PARAMETERS

NPRINT(0-NO PRINT,1-PRINT)	1
NSUMRY(0-NO SUMMARY TABLES,1-YES)	1
NPLOT(0-NO ISOMETRIC CARPET PLOTS,1-PLOT)	1
NDSKW(0-NO DISC SAVE,1-DISC SAVE)	0
NDSKR(0-NO DISC START,>0-DISC START AT STEP NDSKR)	0

ISOMETRICALLY PLOTTED QUANTITIES (1-YES,0-NO)

MESH 0 POROSITY 1 GRANULAR STRESS 0 PRESSURE 1  
DENSITY 0 GAS AXIAL VELOCITY 1 SOLID AXIAL VELOCITY 0  
GAS RADIAL VELOCITY 1 SOLID RADIAL VELOCITY 0 GAS TEMPERATURE 0  
PARTICLE SURFACE TEMPERATURE 0

TERMINATION AND LOGOUT PARAMETERS

MAX. STEPS	10000
MAX. TRAVEL(CM)	475.000
STEPS TO LOGOUT	10000
INTERVAL TO LOGOUT(MSEC)	0.500
DEBUG PRINT(0-NO;1-YES)	0

INTEGRATION DATA

COURANT NUMBER(-)	0.500
ANTIDIFFUSIVE FLUX MULTIPLIER	0.999
TOTAL NUMBER OF RADIAL CELLS(-)	10
MINIMUM NUMBER OF AXIAL CELLS BEHIND AFTERBODY	15
MAXIMUM NUMBER OF AXIAL CELLS BEHIND AFTERBODY	15
NUMBER OF AXIAL CELLS ALONG AFTERBODY	15
NUMBER OF RADIAL CELLS AT BASE OF AFTERBODY	3

INITIAL DATA

PRESSURE(MPA)	6.895
TEMPERATURE(K)	3009.0
GAMMA(-)	1.2430
MOL.WGT(GM/GMOL)	23.3600
COVOLUME(CM**3/GM)	1.0300

CHARGE REPRESENTATION PARAMETERS

NUMBER OF PROPELLANTS IN CHARGE	1
NUMBER OF INCREMENTS IN CHARGE	1
PROPELLANT MODEL (1-LP,2-2D)	2

PROPERTIES OF PROPELLANT TYPE 1

SOLID PHASE CONSTITUTIVE DATA

SETTLING POROSITY OF GRANULAR BED(-)	0.40000
SPEED OF COMPRESSION WAVE(CM/SEC)	15240.0
SPEED OF EXPANSION WAVE(CM/SEC)	127000.0
DENSITY OF SOLID PHASE(GM/CC)	1.5830
THERMAL CONDUCTIVITY(J/CM-SEC-DEG.K)	0.160100E-02
THERMAL DIFFUSIVITY(CM**2/SEC)	0.645160E-03

GAS PHASE CONSTITUTIVE DATA AND PROPELLANT INITIAL TEMPERATURE

RATIO OF SPECIFIC HEATS(-)	1.24300
MOLECULAR WEIGHT(GM/GM-MOL)	23.260
COVOLUME(CC/GM)	1.030
INITIAL TEMPERATURE (DEG.K)	445.0

SOLID PHASE COMBUSTION CHARACTERISTICS

NUMBER OF BURN RATE DATA	2
IGNITION TEMPERATURE(DEG.K)	444.4
CHEMICAL ENERGY(J/GM)	4384.

MAX. PRESSURE (MPA)	BURN RATE ADDITIVE CONSTANT (CM/SEC)	PRE-EXPONENT (CM/SEC-MPA**BN)	EXPONENT (-)
68.95	0.00000	0.50000	0.70000
689.50	0.00000	0.50000	0.70000

GRAIN GEOMETRY

FORM(0-CYLINDER,1-SPHERE,2-SOLID STICK, 3-PERFORATED OR SLOTTED STICK)	0
EXTERNAL DIAMETER(CM)	1.060
LENGTH(CM)	2.408
DIAMETER OF PERFORATIONS(CM)	0.086
NUMBER OF PERFORATIONS(-)	7.

PROPERTIES OF INCREMENT NUMBER 1

MAIN CHARGE PROPELLANT TYPE	1
NUMBER OF AXIAL CELLS	30
NUMBER OF RADIAL CELLS	8
MASS OF MAIN CHARGE(G)	7800.0000
REAR BOUNDARY DELIMITER (CM)	0.000
FORWARD BOUNDARY DELIMITER (CM)	0.000
INNER BOUNDARY DELIMITER (CM)	0.000
OUTER BOUNDARY DELIMITER (CM)	0.000

PROPERTIES OF PROJECTILE

INITIAL POSITION OF PROJECTILE/SABOT BASE(CM)	55.900
PROJECTILE MASS(GM)	8936.000
NUMBER OF ENTRIES IN BORE RESISTANCE TABLE	2
RESISTANCE LAW NUMBER	0

N.B. IF <1 OR >3, VALUE WILL DEFAULT TO 2 INTERNALLY

BORE RESISTANCE DATA

PROJECTILE TRAVEL(CM)	RESISTIVE PRESSURE(MPA)
0.000	0.000
600.000	0.000

NUMBER OF TUBE GEOMETRY DATA 6

TUBE GEOMETRY

AXIAL POS(CM)	RADIUS(CM)
0.000E+00	5.72
7.62	7.85
48.3	7.85
55.9	6.05
59.4	6.00
529.	6.00

NUMBER OF AFTERBODY GEOMETRY DATA 2

AFTERBODY GEOMETRY

AXIAL POS(CM)	RADIUS(CM)
0.000E+00	1.90
36.8	2.67

note, at 4.5 ms, the separation from the re-entrant corner at the mouth of the tube, as grains are swept around the chambrage.

Additional details of the simulation are shown in Figures 4.6 - 4.8, which illustrate the gas-phase flow field at three times, and by Figures 4.9 - 4.11, which illustrate the pressure contours at the same times. It is interesting to note the suction created by the base of the afterbody which strongly perturbs the flow field away from the axial structure implicit in one-dimensional codes. We note that since the grid behind the afterbody is expanding in concert with the motion of the projectile, while that along the afterbody retains its initial axial spacing, there is a strong discontinuity in cell size near the base of the afterbody at later times. It may be useful to admit a refinement of the rear complement of cells to retain resolution of the chamber geometry as well as to reduce this disparity in cell size.

The pressure contours show that in spite of the non-uniform geometry and the flow field, the distributions quickly become nearly one-dimensional except right near the base of the afterbody. Some small pressure wiggles are apparent in that region. It is not presently known to what extent these reflect the limited complement of cells or the local clustering of propellant particles due to the Helmholtz mechanism discussed in the previous chapter.

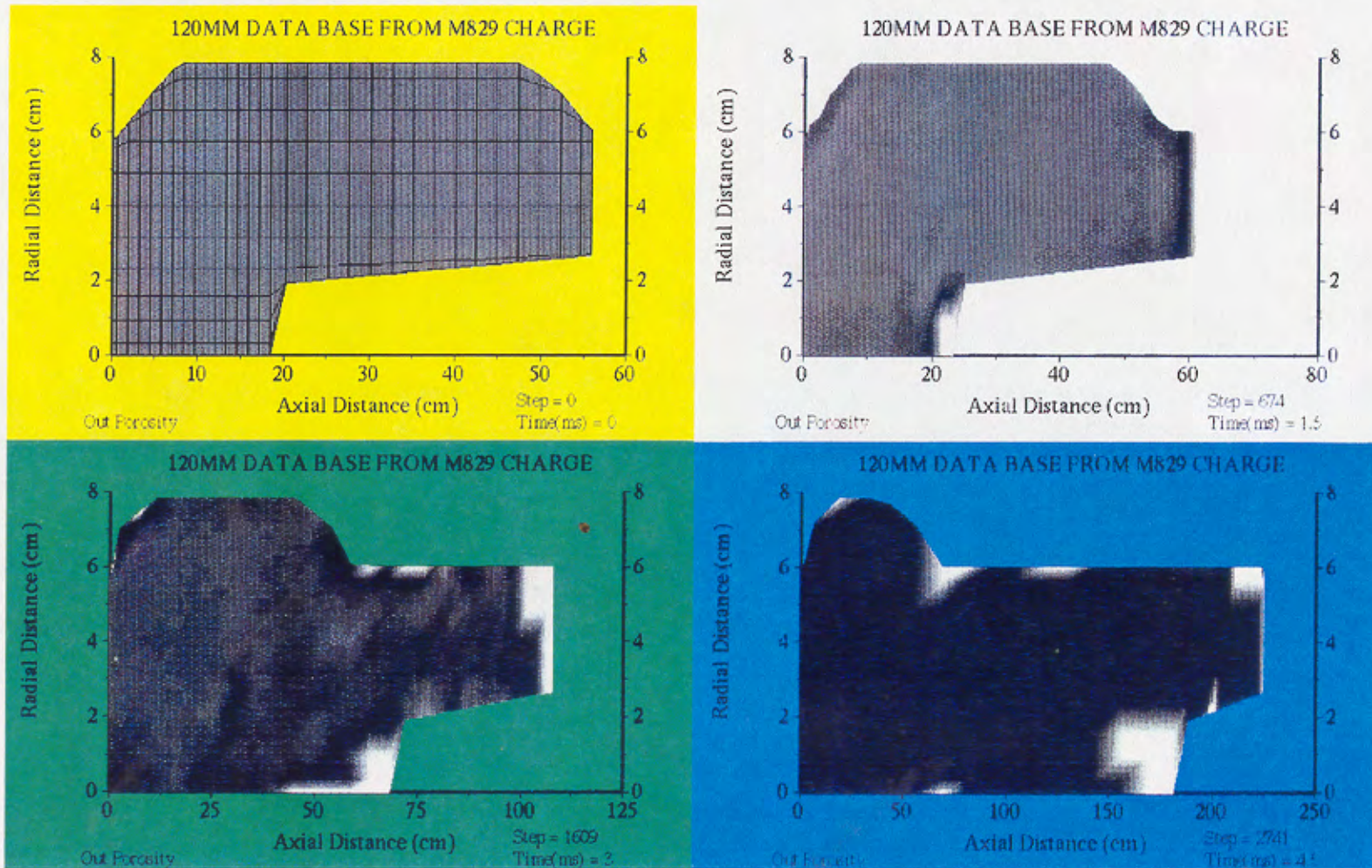


Figure 4.5 Porosity Distributions in 120mm Tank Gun at Four times.

# ARL CFD SIMULATION / NGEN CODE

## 120mm Gun, M829 Charge

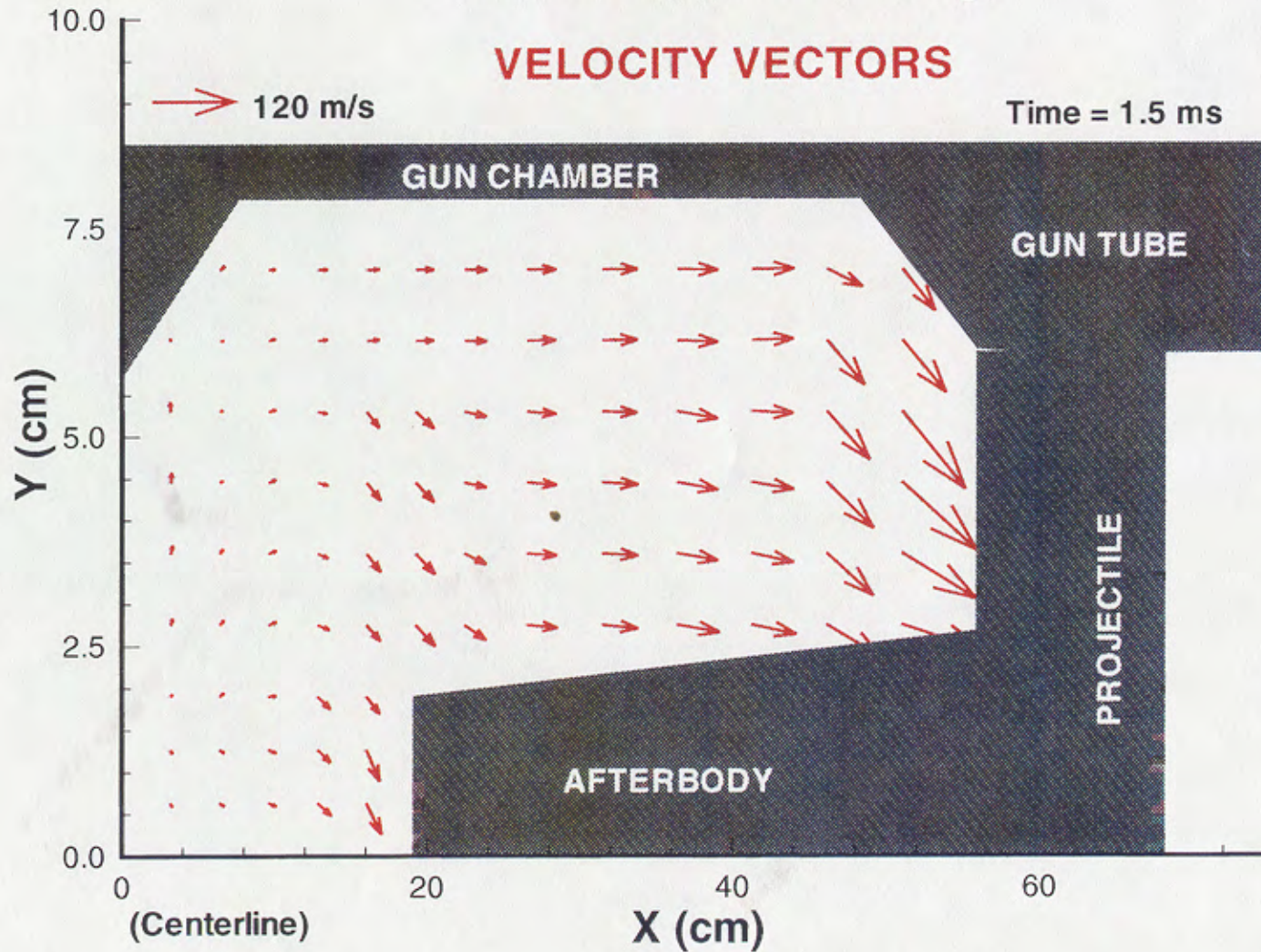


Figure 4.6 Gas-Phase Flow Field in 120mm Tank Gun at 1.5 ms.

# ARL CFD SIMULATION / NGEN CODE

## 120mm Gun

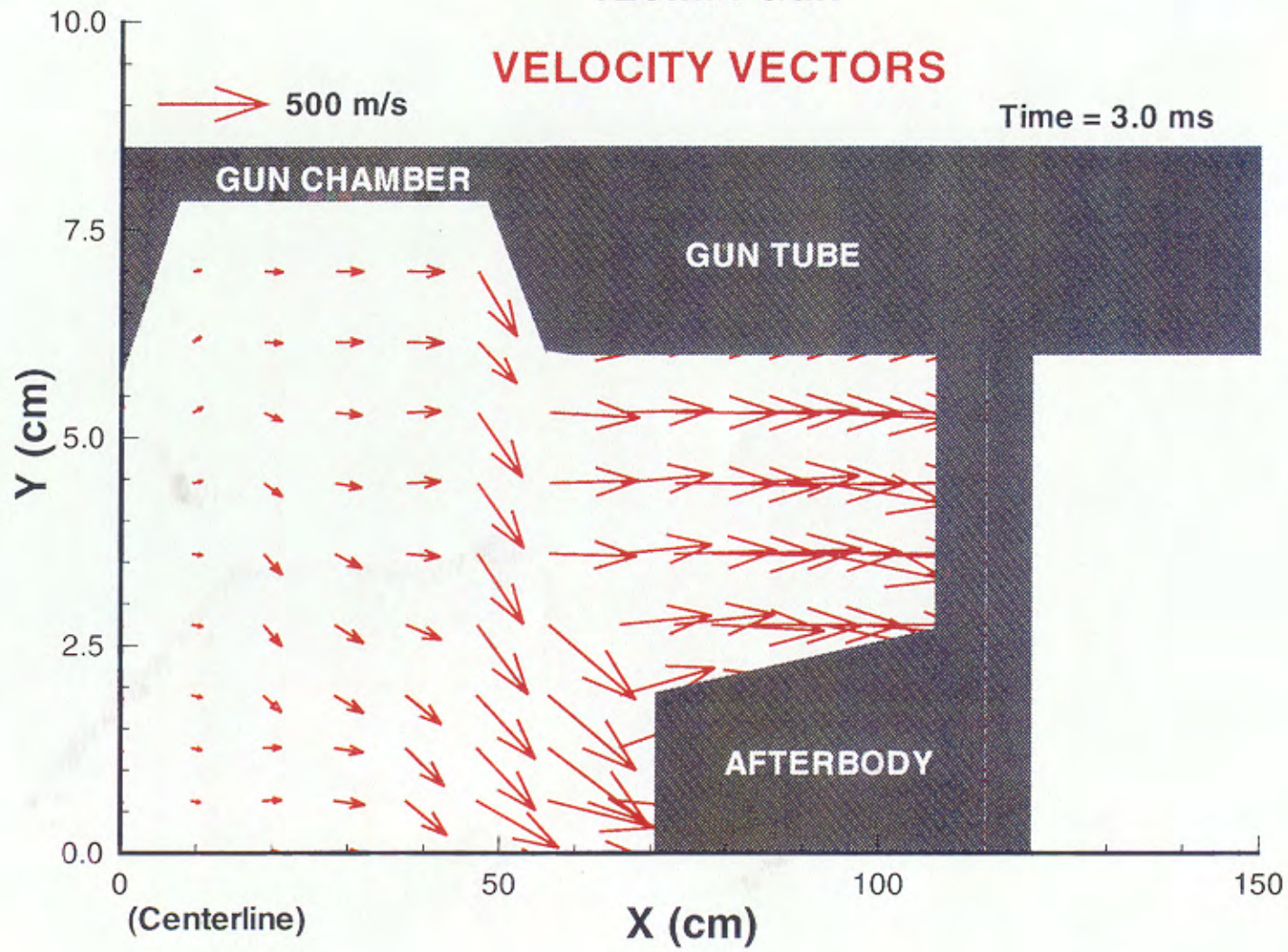


Figure 4.7 Gas-Phase Flow Field in 120mm Tank Gun at 3.0 ms.

# ARL CFD SIMULATION / NGEN CODE

## 120mm Gun

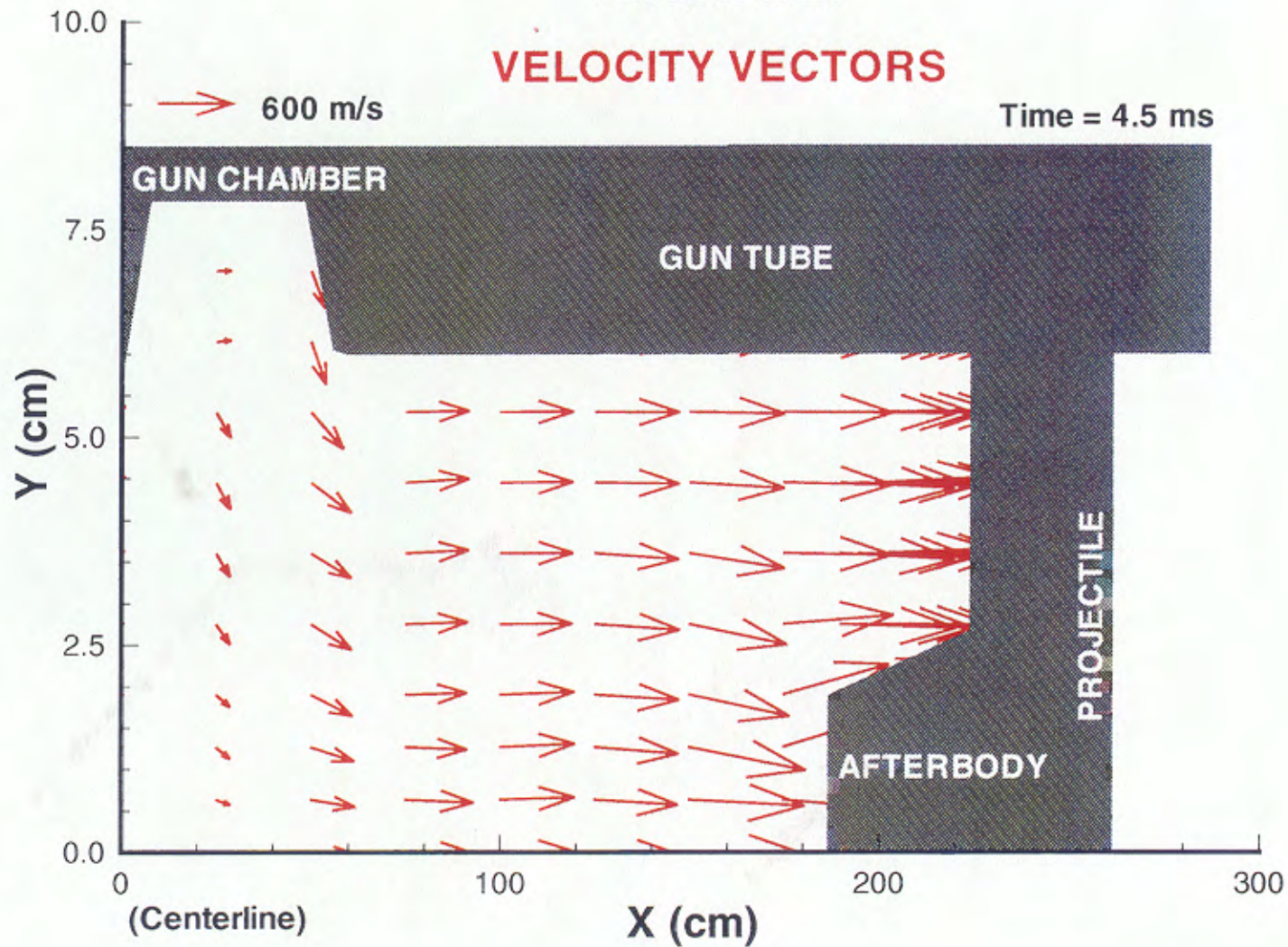


Figure 4.8 Gas-Phase Flow Field in 120mm Tank Gun at 4.5 ms.

# ARL CFD SIMULATION / NGEN CODE

120mm Gun

PRESSURE CONTOURS

Time = 1.5 ms

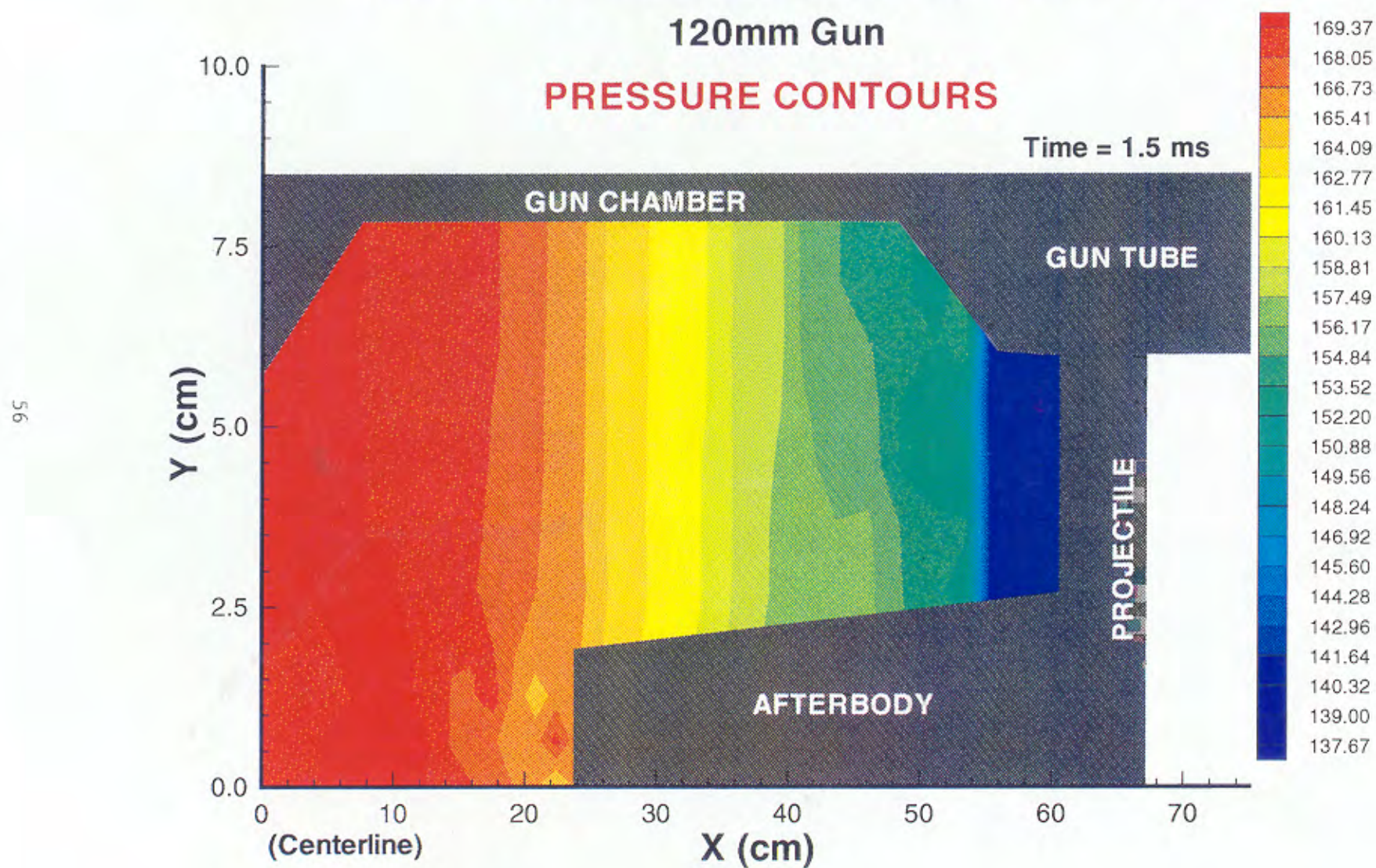


Figure 4.9 Pressure Contours in 120mm Tank Gun at 1.5 ms.

# ARL CFD SIMULATION / NGEN CODE

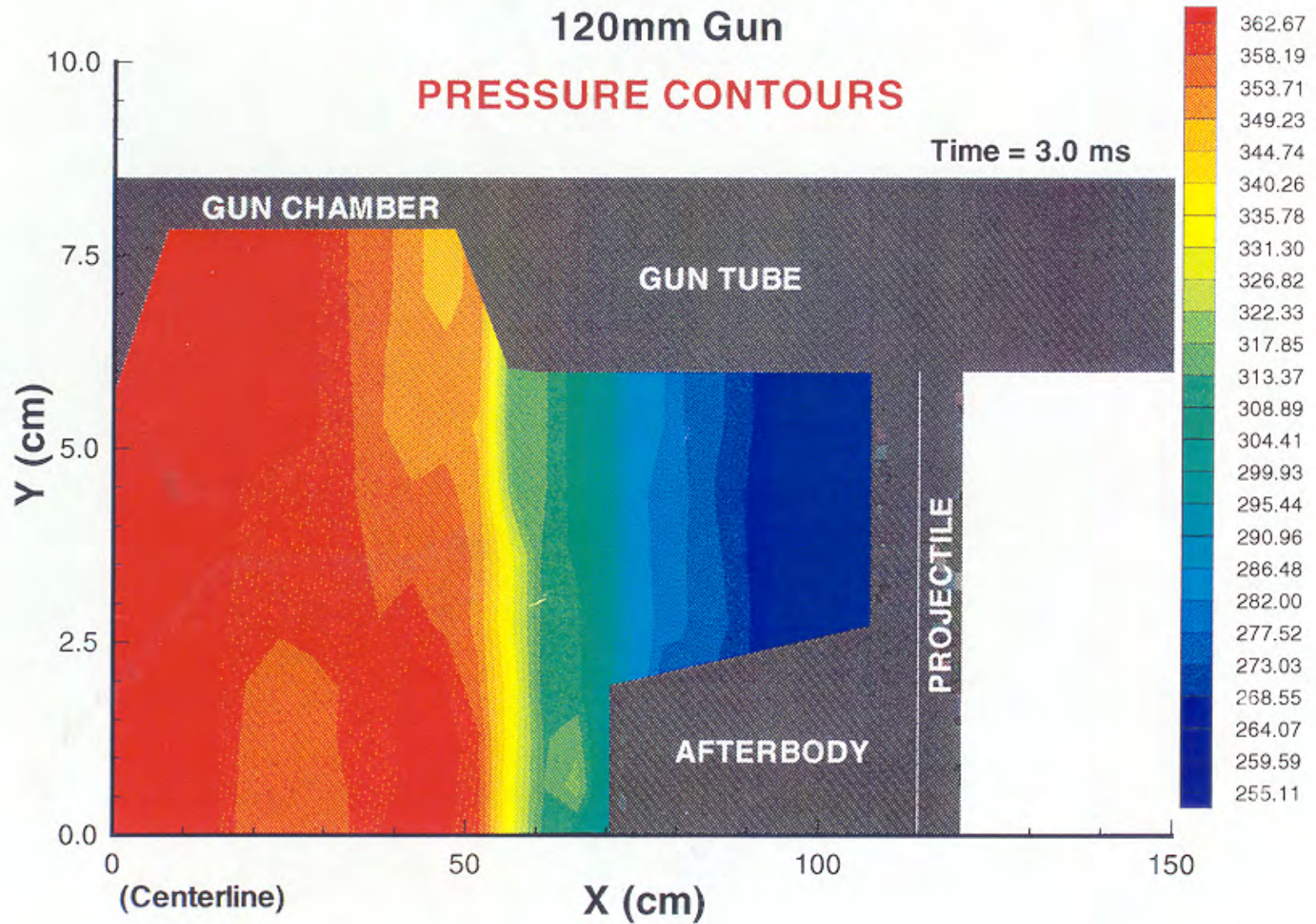


Figure 4.10 Pressure Contours in 120mm Tank Gun at 3.0 ms.

# ARL CFD SIMULATION / NGEN CODE

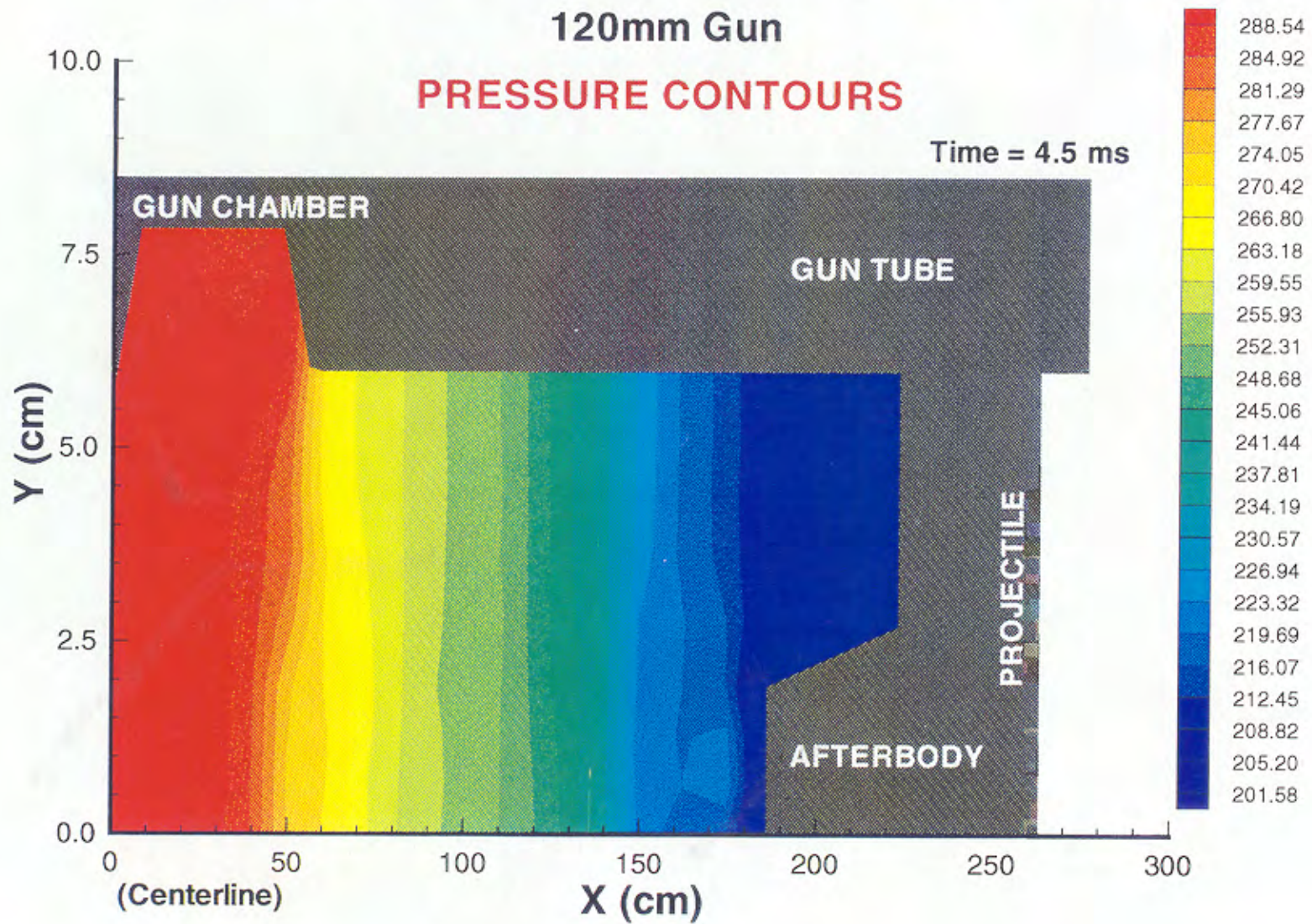


Figure 4.11 Pressure Contours in 120mm Tank Gun at 4.5 ms.

## 5.0 CONCLUSIONS

We have developed and described algorithms to support two key modules of the NGEN Code. We have used LCPFCT as the basis for the continuum flow solver (CFS) and developed a Large Particle Integrator (LPI) to track the propellant grains in solid propellant charges.

The CFS uses LCPFCT in a timesplit formulation which is easy to understand and modify. We have presented a method of accommodating non-uniform geometry in a structured mesh, using a characteristic based analysis. This analysis permits the timestep to be based on the Courant stability condition for interior cells even when the boundary cells will violate it by two orders of magnitude. The characteristic based analysis has been formulated in a fashion which is simple to implement and which imposes a minimal computational burden. The approach taken to the treatment of non-uniform geometry is thought to admit massive parallelization, although the special treatment of boundary cells suggests that optimal computer architecture may be such that individual processors integrate a string of cells rather than just one. More importantly, the method is thought to address the complexities associated with the representation of internal boundaries defined by increment containers. The LPI is also simple in structure and provides direct control of the porosity distribution at the boundaries of charge increments.

We have illustrated operability of the algorithm by reference to two solid propellant data bases, one for a 155 mm howitzer and the other for a 120 mm tank gun. Each calculation required about 10 minutes on an SGI Indigo work station, showing the algorithm to be reasonably fast even though no special measures have yet been taken to optimize run times.

INTENTIONALLY LEFT BLANK.

## REFERENCES

- Boris, J.P. and Book, D.L. "Solution of Continuity Equations by the Method of Flux-Corrected Transport" *Methods in Computational Physics* 16 pp 85-129 1976
- Boris, J.P., Landsberg, A.M., Oran, E.S. and Gardner, J.H. "LCPFCT - A Flux-Corrected Transport Algorithm for Solving Generalized Continuity Equations" *NRL Memorandum Report NRL/MR/6410-93-7192, Naval Research Laboratory* 1993
- Chen, J.L., Kuo, K.K. and Cheung, F.B. "Theoretical Modeling of the Interior Ballistic Processes in an Electrothermal Gun" *Proceedings of the 27th Jannaf Combustion Meeting* 1990
- Coffee, T.P. "A Two-Dimensional Model for the Combustion Chamber/ Gun Tube of a Concept VI C Regenerative Liquid Propellant Gun" *Proceedings of the 27th Jannaf Combustion Meeting* 1990
- Cook, D.C., Dyvik, J.A. and Chryssomallis, G.S. "A Multidimensional Electrothermal Model" *Proceedings of the 26th Jannaf Combustion Meeting* 1989
- Courant, R and Hilbert, D. "Methods of Mathematical Physics" *Interscience* 1953
- Fisher, E.B. and Graves, K.W. "Mathematical Model of Double Base Propellant and Ignition in the 81mm Mortar" *Calspan Report DG-3029-D-1* 1972
- Fitt, A.D., Crowley, A.B., Aston, J.A.G. and Toro, E.F. "Contrasting Numerical Methods for Two-Dimensional Two-Phase Interior Ballistic Flows" *Proceedings of the 11th International Symposium on Ballistics* 1989
- Gelperin, N.I. and Einstein, V.G. "Heat Transfer in Fluidized Beds." *Fluidization*, edited by Davidson, J.F. and Harrison, D. *Academic Press, NY* 1971
- Gibeling, H.J. and McDonald, H. "An Implicit Numerical Analysis for Two-Dimensional Turbulent Interior Ballistic Flows" *Ballistic Research Laboratory Contract Report ARBRL-CR-00523* 1984
- Gough, P.S. "Modeling of Rigidized Gun Propelling Charges" *Ballistic Research Laboratory Contract Report ARBRL-CR-00518* 1983
- Gough, P.S. "The XNOVAKTC Code" *Paul Gough Associates Report PGA-TR-86-1* 1986
- Gough, P.S. "Formulation of a Next-Generation Interior Ballistic Code" *Proceedings of the 29th Jannaf Combustion Meeting* 1991

- Gough, P.S. "Formulation of a Next-Generation Interior Ballistic Code I. Evaluation of Computational Algorithms" Proceedings of the 30th Jannaf Combustion Meeting 1992
- Groenenboom, P.H.L. and Thomsen, P. "Two Phase Flow Computation for a 40mm Granular Propellant Gun in Comparison with Experimental Results" Proceedings of the 11th International Symposium on Ballistics 1989
- Hadley, G. "Linear Algebra" Addison-Wesley 1961
- Hsiao, C.C., Phillips, G. and Su, F. "First Principles Modeling of a DNA 60mm ETC Gun Design" Jannaf Workshop on ETC Modeling and Diagnostics 1991
- Kashiwa, B.A., Padial, N.T. and Butler, D. "Toward a Comprehensive Model for Electrothermal Gun Performance" Proceedings of the 27th Jannaf Combustion Meeting 1990
- Krier, H., Shimpi, S.A. and Adams, M.J. "Interior Ballistic Predictions Using Data From Closed and Variable Volume Simulators." Univ. of Illinois at Urbana-Champaign. TR-AAE-73-6 1973
- Landsberg, A.M., Boris, J.P., Young, T.R. and Scott, R.J. "Computing Complex Shocked Flows Through the Euler Equations" Naval Research Laboratory 1993
- Lohner, R. "Adaptive H-refinement on 3-D Unstructured Grids for Transient Problems" AIAA Paper 89-0653 1989
- Love, A.E.A. and Pidduck, F.B. "Lagrange Ballistic Problem" Phil. Trans. Roy. Soc. vol 222 pp 167-226 1921
- May, I.W. and Horst, A.W. "Charge Design and Pressure Waves in Guns" Papers in Astronautics and Aeronautics, vol.68, Interior Ballistics of Guns, Edited by H. Krier and M. Summerfield. 1979
- Meineke, E. and Heiser, R. "A Complete Numerical Solution of the Interior Ballistics Chambrage Problem" Proceedings of the 11th International Symposium on Ballistics 1989
- Oran, E.S., Boris, J.P. and Brown, E.F. "Fluid-Dynamic Computations on a Connection Machine -- Preliminary Timings and Complex Boundary Conditions" AIAA Paper 90-0335 1990
- Robbins, F.W. "Comparison of TDNOVA Results with an Analytic Solution" ARBRL-MR-03299, USA ARRADCOM, Ballistic Research Laboratory 1983
- Schmitt, J.A. and Mann, T.L. "An Evaluation of the Alpha Code in its One-Phase Mode" ARBRL-MR-03081, USA ARRADCOM, Ballistic Research Laboratory 1981

- Schmitt, J.A. "A Numerical Algorithm for the Multidimensional, Multiphase, Viscous Equations of Interior Ballistics" Proceedings of the 2nd Army Conference on Applied Mathematics and Computing 1984
- Sinha, N., Hosangadi, A. and Dash, S.M. "Development of an Upwind/Implicit Computational Model for the Advancement of Army ETC Guns" Jannaf Workshop on ETC Modeling and Diagnostics 1991
- Steffens, U., Krassin, D. and Rittel, R. "Two-Phase Flow Predictions of Regenerative Liquid Propulsion - A Comparison with Experimental Results" Proceedings of the Tenth International Symposium on Ballistics 1987
- Steffens, U., Rittel, R., Lenselink, H. and Florie, K. "Applications of a Three-Dimensional Gasdynamic Simulation Model to Interior Ballistics" Proceedings of the Eleventh International Symposium on Ballistics 1989
- Thomas, P.D. and Lombard, C.K. "Geometric Conservation Law and its Application to Flow Computations on Moving Grids" AIAA Journal n.17 pp 1030-1036 1979
- Thompson, J.F., Warsi, Z.U.A. and Masten, C.W. "Numerical Grid Generation" North Holland, New York 1985
- Williams, F.A. "Combustion Theory" Addison-Wesley 1965
- Winsor, N.K. and Goldstein, S.A. "Finite Element Modeling of an Electrothermal Gun" Proceedings of the 27th Jannaf Combustion Meeting 1990

**INTENTIONALLY LEFT BLANK.**

## NOMENCLATURE

A	Area of computational cell in LCPFCT
a	Rate of propagation of intergranular disturbances
B	Burn rate coefficient
b	Covolume
c	Isentropic speed of sound in continuous phase
$c_v$	Specific heat at constant volume
$c_p$	Specific heat at constant pressure
$D_0$	Initial diameter of grain
$D_{p_0}$	Effective diameter of grain
d	Surface regression
$d_0$	Initial perforation diameter of grain
E	Total energy per unit volume of continuous phase
e	Internal energy of continuous phase
$e_{i_8}$	Chemical energy of propellant
$e_p$	Chemical energy of igniter
$f_{d_1}$	Interphase drag due to i-th discrete phase
$f_r$	Radial component of interphase drag
$\hat{f}_s$	Friction factor
$f_z$	Axial component of interphase drag
$\epsilon_0$	Constant used to reconcile units
H	Thermal parameter for cubic profile analysis of propellant temperature
h	Film coefficient
k	Thermal conductivity
L	Length of propellant grain
$\dot{m}$	Mass generation per unit volume due to propellant combustion
$\dot{m}_{i,j}$	Mass generation per unit volume due to igniter combustion
N	Number of perforations in propellant grain
$N_c$	Number of continuous phases
$N_d$	Number of dispersed phases
$Nu_p$	Nusselt number
n	Burn rate exponent

$n_{d_i}$	Number density of i-th dispersed phase
Pr	Prandtl number
p	Pressure
q	Heat transfer per unit surface area
$q_{d_i}$	Heat transfer per unit volume to i-th dispersed phase
$q_p$	Heat transfer per unit volume to propellant
$Re_p$	Reynolds number
r	Radial coordinate
$S_{d_i}$	Surface area of member of i-th dispersed phase
$S_p$	Surface area of a propellant grain
T	Temperature of continuous phase
$T_{d_i}$	Temperature of i-th dispersed phase
$T_p$	Surface temperature of propellant
t	Time
u	Velocity of continuous phase
$u_{d_i}$	Velocity of i-th dispersed phase
u	Axial velocity component of continuous phase
$u_p$	Axial velocity component of propellant
$V_{d_i}$	Volume of a member of i-th dispersed phase
$v_p$	Volume of a propellant grain
$v_i$	Diffusion velocity of i-th component of continuous phase
v	Radial velocity component of continuous phase
$v_p$	Radial velocity component of propellant
$Y_i$	Mass fraction of i-th component of continuous phase
z	Axial coordinate

#### Greek Symbols

$\alpha$	Porosity
$\alpha_1$	Volume fraction of i-th component of continuous phase
$\alpha_{d_i}$	Volume fraction of i-th component of dispersed phase
$\gamma$	Ratio of specific heats
$\Lambda$	Volume of computational cell in LCPFCT

$\mu$	Viscosity
$\rho$	Density of continuous phase
$\rho_p$	Density of propellant grain
$\sigma_{d_i}$	Stress tensor for i-th dispersed phase
$\sigma$	Intergranular stress
$\tau$	Shear stress tensor
$\dot{\omega}_i$	Rate of production of i-th component of continuous phase due to chemical reactions

**INTENTIONALLY LEFT BLANK.**

**APPENDIX A:**  
**CHARACTERISTIC ANALYSIS OF CONTINUUM EQUATIONS**

INTENTIONALLY LEFT BLANK.

Our interest in this topic is principally motivated by the numerical ramifications of the theory of characteristic surfaces. In the case of one dimensional unsteady flow, the existence of real characteristic directions enables one to replace the system of partial differential equations by an equivalent system of ordinary differential equations in which the derivatives are taken along the characteristic lines. When we proceed to a larger number of independent variables an analogous result holds for hyperbolic systems of equations. Given  $n$  independent variables, a hyperbolic system is one that admits the existence of a hypersurface of dimension  $n - 1$  such that only derivatives interior to the surface appear in the equations.

We proceed as follows. In Section A.1, we discuss the theory in general for a quasilinear system of partial differential equations which depend on three independent coordinates. Then, in Section A.2 we deduce the characteristic forms for an inviscid two dimensional single phase flow with non-homogeneous source terms. By treating the additional terms associated with diffusion as embedded in the non-homogeneous source terms we can easily establish "pseudocharacteristic" forms, which are of value in the formulation of numerical solution algorithms for the Navier-Stokes equations. Similarly, with suitable interpretation, we may apply the results obtained here in the context of multiphase flows.

### A.1 General Formulation of Characteristic Analysis

Consider a system of partial differential equations

$$A \frac{\partial \psi}{\partial t} + B \frac{\partial \psi}{\partial z} + C \frac{\partial \psi}{\partial r} = D \tag{A.1.1}$$

where  $\psi$  and  $D$  are  $n$ -dimensional column vectors and  $A$ ,  $B$ ,  $C$  are  $n \times n$  square matrices. The concept of a characteristic surface follows naturally from the consideration of an initial value problem posed for a surface



The condition  $\text{Rank}(\Delta) < n$  will lead to a partial differential equation for  $\phi(t, z, r)$  in the form

$$F(t, z, r, \psi, \phi_t, \phi_z, \phi_r) = 0 \quad , \quad \text{A.1.6}$$

it being assumed that  $A, B, C$  are functions only of  $t, z, r$  and  $\psi$ . Since every element of  $\Delta$  is a homogeneous linear combination of  $\phi_t, \phi_z$  and  $\phi_r$  it follows that  $F$  is homogeneous of order  $\kappa \geq 1$  in these quantities so that

$$F(t, z, r, \psi, \lambda\phi_t, \lambda\phi_z, \lambda\phi_r) = \lambda^\kappa F(t, z, r, \psi, \phi_t, \phi_z, \phi_r) \quad . \quad \text{A.1.7}$$

Accordingly it follows that

$$F_{\phi_t}\phi_t + F_{\phi_z}\phi_z + F_{\phi_r}\phi_r = 0 \quad . \quad \text{A.1.8}$$

Because of the degree of freedom induced by the homogeneity of  $F$  it is convenient in many cases to append an additional condition corresponding to the normalization of the vector  $(\phi_t, \phi_z, \phi_r)$ . In practice the most convenient choice is to set  $\phi_t = -1$ . This corresponds to having  $\phi$  in the form

$$\phi = t(z, r) - t \quad , \quad \text{A.1.9}$$

so that  $\phi_t = -1$ ,  $\phi_z = \partial t / \partial z$  and  $\phi_r = \partial t / \partial r$ .

It is useful to interpret these results geometrically (Courant and Hilbert, 1953). We may think of  $\phi = \phi_0$  as defining a surface with normal vector proportional to  $(\phi_t, \phi_z, \phi_r)$ . Then A.1.6, the partial differential equation for the characteristic surface, imposes an algebraic constraint on the components of the normal at each point in the  $(t, z, r)$  space. At each point A.1.6 defines a family of planes such that the characteristic surface must be tangent to one of them. If  $F$  is not linear, the envelope of this family of planes is a cone, the Monge cone, whose generators are called bicharacteristics.

According to A.1.7 the family of allowable normal vectors at a given point lies on the surface of a cone whose apex is the point in question. Thus A.1.8 asserts that the vector  $(F_{\phi_t}, F_{\phi_z}, F_{\phi_r})$  is perpendicular not only to the surface of normal vectors, but also to the vectors themselves since they lie along the cone. In fact, the vector  $(F_{\phi_t}, F_{\phi_z}, F_{\phi_r})$  defines a bicharacteristic

direction. From A.1.8 it is evident that it must lie in a tangent plane of a characteristic surface. However, the bicharacteristic may be thought of as the limit of the line of intersection of neighboring tangent planes. Thus if we write  $b$  as a bicharacteristic,  $n$  as the normal to a tangent plane and  $\lambda$  as a parameter which labels the planes at a given point, it follows that

$$b = n \times \left[ n + \frac{dn}{d\lambda} d\lambda \right]. \quad \text{Therefore } b = n \times \frac{dn}{d\lambda} d\lambda. \quad \text{Since both } n \text{ and } \frac{dn}{d\lambda} \text{ lie on a}$$

tangent plane of the cone defined by A.1.6 we see that  $b$  is parallel to  $(F_{\phi_t}, F_{\phi_z}, F_{\phi_r})$ . The bicharacteristic ray may be written as

$$\frac{dt}{F_{\phi_t}} = \frac{dz}{F_{\phi_z}} = \frac{dr}{F_{\phi_r}} \quad \text{A.1.10}$$

This result may be used to eliminate  $\phi_t$ ,  $\phi_z$  and  $\phi_r$  from A.1.6 and to describe the characteristic surface by reference to the bicharacteristics.

## A.2 Two-Dimensional Inviscid Single-Phase Flow

We now wish to deduce complete results for a two-dimensional, inviscid, single-phase flow with a local source term. We will also assume that the equations are subject to a general coordinate transformation for computational purposes. We may first state the equations in cylindrical coordinates in non-conservative form and with the energy equation recast to eliminate the internal energy in favor of pressure and density with the help of the continuity equations and the thermodynamic identity

$$\frac{p}{\rho^2} - \left( \frac{\partial e}{\partial \rho} \right)_p = \frac{c^2}{g_0} \left( \frac{\partial e}{\partial p} \right)_\rho, \quad \text{A.2.1}$$

where we have  $p$ , pressure;  $\rho$ , density;  $e$ , internal energy;  $c$ , isentropic speed of sound; and  $g_0$ , a constant to reconcile units.

The identification of the non-homogeneous terms with a local source is for illustrative purposes only. As noted in the introduction, the formulism of this section is intended to be applicable to more complex systems of

equations in which certain partial derivatives may also be treated formally as "non-homogeneous". Such terms will include diffusion terms and terms related to the porosity in multiphase flows.

With  $t$ , time;  $z$ , axial coordinate;  $r$ , radial coordinate;  $u$ , axial velocity;  $v$ , radial velocity; and  $\dot{m}$  a local source whose energy content is  $e_{1g}$ , we have

$$\frac{D\rho}{Dt} + \rho \left( \frac{\partial u}{\partial z} + \frac{\partial v}{\partial r} \right) = \dot{m} - \frac{\rho v}{r} = \xi_1 \quad , \quad \text{A.2.2}$$

$$\rho \frac{Du}{Dt} + g_o \frac{\partial p}{\partial z} = -\dot{m}u = \xi_2 \quad , \quad \text{A.2.3}$$

$$\rho \frac{Dv}{Dt} + g_o \frac{\partial p}{\partial r} = -\dot{m}v = \xi_3 \quad , \quad \text{A.2.4}$$

$$\frac{Dp}{Dt} - \frac{c^2}{g_o} \frac{D\rho}{Dt} = \frac{\dot{m}}{\rho \left( \frac{\partial e}{\partial p} \right)_p} \left\{ e_{1g} + \frac{u \cdot u}{2g_o} - e - p/\rho \right\} = \xi_4 \quad , \quad \text{A.2.5}$$

and where  $D/Dt$  is the convective derivative.

We identify these equations with the system

$$A \frac{\partial \psi}{\partial t} + B \frac{\partial \psi}{\partial z} + C \frac{\partial \psi}{\partial r} = D \quad , \quad \text{A.2.6}$$

by setting

$$\psi = \begin{bmatrix} \rho \\ u \\ v \\ p \end{bmatrix} \quad , \quad D = \begin{bmatrix} \xi_1 \\ \xi_2 \\ \xi_3 \\ \xi_4 \end{bmatrix} \quad , \quad A = \begin{bmatrix} 1 & 0 & 0 & 0 \\ 0 & \rho & 0 & 0 \\ 0 & 0 & \rho & 0 \\ -\frac{c^2}{g_o} & 0 & 0 & 1 \end{bmatrix} \quad ,$$

$$B = \begin{bmatrix} u & \rho & 0 & 0 \\ 0 & \rho u & 0 & g_0 \\ 0 & 0 & \rho v & 0 \\ -\frac{c^2 u}{g_0} & 0 & 0 & u \end{bmatrix}$$

$$C = \begin{bmatrix} v & 0 & \rho & 0 \\ 0 & \rho v & 0 & 0 \\ 0 & 0 & \rho v & g_0 \\ -\frac{c^2 v}{g_0} & 0 & 0 & v \end{bmatrix}$$

A.2.7

At this point we have established the balance equations in a form suitable for the application of the methodology described in Section A.1. However, we now consider a transformation of coordinates in the form

$$\begin{aligned} \tau &= t & , \\ \zeta &= \zeta(t, z, r) & , \\ \eta &= \eta(t, z, r) & . \end{aligned}$$

A.2.8

We assume that this transformation is one to one and has continuous partial derivatives and that  $\partial(\zeta, \eta)/\partial(z, r) \neq 0$  so that we can also write

$$\begin{aligned} t &= \tau & , \\ z &= z(\tau, \zeta, \eta) & , \\ r &= r(\tau, \zeta, \eta) & . \end{aligned}$$

A.2.9

We have used a separate notation  $\tau$  for the time in the transformed frame. This facilitates the use of subscripts to denote partial derivatives. Thus we

understand  $\phi_t = \left( \frac{\partial \phi}{\partial t} \right)_{z,r}$  whereas  $\phi_\tau = \left( \frac{\partial \phi}{\partial \tau} \right)_{\zeta,\eta}$  and  $\phi$  is an arbitrary property.

Bearing this in mind we define

$$\begin{aligned} u_m &= z_r \quad , \\ v_m &= r_r \quad . \end{aligned} \tag{A.2.10}$$

Thus  $u_m$  and  $v_m$  are the velocity components in a cylindrical coordinate frame of a point moving so that it is stationary with respect to the transformed frame. Evidently, if we impose the requirement  $u_m = u$  and  $v_m = v$  we will have selected the transformed frame to coincide with a Lagrangian description of the fluid whereas the choice  $u_m = v_m = 0$  implies the retention of an Eulerian description, possibly in a different coordinate frame established by a stationary transformation.

It follows that the balance equations A.2.6 subject to A.2.8 and A.2.10 become

$$A \frac{\partial \psi}{\partial \tau} + [(B - Au_m)\zeta_z + (C - Av_m)\zeta_r] \frac{\partial \psi}{\partial \zeta} + [(B - Au_m)\eta_z + (C - Av_m)\eta_r] \frac{\partial \psi}{\partial \eta} = D \quad . \tag{A.2.11}$$

Thus we now consider the characteristic surfaces for the system

$$A \frac{\partial \psi}{\partial \tau} + B' \frac{\partial \psi}{\partial \zeta} + C' \frac{\partial \psi}{\partial \eta} = D \tag{A.2.12}$$

where we identify  $B'$  and  $C'$  as:

$$B' = \begin{bmatrix} w & \rho \zeta_z & \rho \zeta_r & 0 \\ 0 & \rho w & 0 & \epsilon_0 \zeta_z \\ 0 & 0 & \rho w & \epsilon_0 \zeta_r \\ -c^2 w / \epsilon_0 & 0 & 0 & w \end{bmatrix}$$

$$C' = \begin{bmatrix} x & \rho\eta_z & \rho\eta_x & 0 \\ 0 & \rho x & 0 & \varepsilon_0\eta_z \\ 0 & 0 & \rho x & \varepsilon_0\eta_x \\ -c^2x/\varepsilon_0 & 0 & 0 & x \end{bmatrix}$$

and where we have introduced

$$w = (u - u_m)\zeta_z + (v - v_m)\zeta_x \quad ,$$

A.2.13

$$x = (u - u_m)\eta_z + (v - v_m)\eta_x \quad .$$

Then the characteristic surfaces  $\phi(\tau, \zeta, \eta)$  are such that the rank of  $\Delta$  is less than four where

$$\Delta = A\phi_\tau + B'\phi_\zeta + C'\phi_\eta \quad .$$

A.2.14

Thus we have

$$\Delta = \begin{bmatrix} \dot{\phi} & \rho(\zeta_z\phi_\zeta + \eta_z\phi_\eta) & \rho(\zeta_x\phi_\zeta + \eta_x\phi_\eta) & 0 \\ 0 & \rho\dot{\phi} & 0 & \varepsilon_0(\zeta_z\phi_\zeta + \eta_z\phi_\eta) \\ 0 & 0 & \rho\dot{\phi} & \varepsilon_0(\zeta_x\phi_\zeta + \eta_x\phi_\eta) \\ -c^2\dot{\phi}/\varepsilon_0 & 0 & 0 & \dot{\phi} \end{bmatrix}$$

and where we have introduced

$$\dot{\phi} = \phi_\tau + w\phi_\zeta + x\phi_\eta \quad .$$

A.2.15

Now in our applications of the conditions of compatibility we shall always require that either  $\phi_\zeta = 0$  or that  $\phi_\eta = 0$  so that the normal lies either in the  $r - \eta$  plane or the  $r - \zeta$  plane. We assume therefore that  $\phi_\eta = 0$ . The corresponding results for the case  $\phi_\zeta = 0$  will follow from considerations of symmetry. With this assumption  $\Delta$  reduces to

$$\Delta = \begin{bmatrix} \dot{\phi} & \rho\zeta_z\phi_\zeta & \rho\zeta_x\phi_\zeta & 0 \\ 0 & \rho\dot{\phi} & 0 & \epsilon_0\zeta_z\phi_\zeta \\ 0 & 0 & \rho\dot{\phi} & \epsilon_0\zeta_x\phi_\zeta \\ -c^2\dot{\phi}/\epsilon_0 & 0 & 0 & \dot{\phi} \end{bmatrix} \quad \text{A.2.16}$$

Now we consider two possibilities

(i) Let  $\dot{\phi} = 0$ . Then  $\Delta$  reduces to

$$\Delta = \begin{bmatrix} 0 & \rho\phi_\zeta\zeta_z & \rho\phi_\zeta\zeta_x & 0 \\ 0 & 0 & 0 & \epsilon_0\zeta_z\phi_\zeta \\ 0 & 0 & 0 & \epsilon_0\zeta_x\phi_\zeta \\ 0 & 0 & 0 & 0 \end{bmatrix}$$

From this it is apparent that the streamline

$$\dot{\phi} = \phi_r + w\phi_\zeta = 0$$

is a characteristic direction. In order to establish the condition of compatibility we now introduce  $\alpha$  and  $\beta$  as coordinates internal to the characteristic surface. Then we may write the augmented matrix as

$$\Delta^* = \Delta \begin{bmatrix} \vdots & \xi_1 - \{ \dot{\alpha} \rho_\alpha + \rho [\zeta_z \alpha_\zeta + \eta_z \alpha_\eta] u_\alpha + \rho [\zeta_x \alpha_\zeta + \eta_x \alpha_\eta] v_\alpha \} \\ \vdots & - \{ \dot{\beta} \rho_\beta + \rho [\zeta_z \beta_\zeta + \eta_z \beta_\eta] u_\beta + \rho [\zeta_x \beta_\zeta + \eta_x \beta_\eta] v_\beta \} \\ \vdots & \\ \vdots & \xi_2 - \{ \rho \dot{\alpha} u_\alpha + g_0 [\zeta_z \alpha_\zeta + \eta_z \alpha_\eta] p_\alpha \} \\ \vdots & - \{ \rho \dot{\beta} u_\beta + g_0 [\zeta_z \beta_\zeta + \eta_z \beta_\eta] p_\beta \} \\ \vdots & \\ \vdots & \xi_3 - \{ \rho \dot{\alpha} v_\alpha + g_0 [\zeta_x \alpha_\zeta + \eta_x \alpha_\eta] p_\alpha \} \\ \vdots & - \{ \rho \dot{\beta} v_\beta + g_0 [\zeta_x \beta_\zeta + \eta_x \beta_\eta] p_\beta \} \\ \vdots & \\ \vdots & \xi_4 - \dot{\alpha} [p_\alpha - c^2 \rho_\alpha / g_0] - \dot{\beta} [p_\beta - c^2 \rho_\beta / g_0] \end{bmatrix}$$

where  $\dot{\alpha}$  and  $\dot{\beta}$  are defined by analogy with  $\dot{\phi}$ .

Accordingly, if we write  $\xi'_i$ ,  $i = 1, \dots, 4$  to denote the members of the fifth column of  $\Delta^*$ , the conditions of solvability yield the following conditions of compatibility.

$$\zeta_z \xi'_3 - \zeta_x \xi'_2 = 0 \quad , \quad \text{A.2.17}$$

$$\xi'_4 = 0 \quad . \quad \text{A.2.18}$$

A convenient choice for  $\alpha, \beta$  is

$$\alpha = \zeta \quad , \quad \beta = \eta \quad , \quad \text{A.2.19}$$

and we will adhere to this convention. The use of a separate nomenclature for the coordinates internal to the characteristic surface is again motivated by the desire to maintain clarity in respect to the representation of the partial derivatives.

Evidently

$$\alpha_\tau = \alpha_\eta = \beta_\tau = \beta_\zeta = 0 \quad ,$$

$$\alpha_\zeta = \beta_\eta = 1 \quad ,$$

and therefore,

$$\dot{\alpha} = w \quad ,$$

$$\dot{\beta} = x \quad .$$

Then, using the chain rule for differentiation and noting  $\dot{\phi}_\eta = 0$  we can show for any variable  $s$  that

$$s_\alpha = s_\zeta - \frac{\phi_\zeta}{\phi_\tau} s_\tau \quad . \quad \text{A.2.20}$$

Since  $\dot{\phi} = 0$  implies  $\phi_\zeta/\phi_\tau = -1/w$ , Equation A.2.17 may be identified as a linear combination of the two momentum equations. Furthermore, Equation A.18 becomes

$$p_\tau + w p_\zeta - \frac{c^2}{\epsilon_0} (\rho_\tau + w \rho_\zeta) = \xi_4 - x \left[ p_\eta - \frac{c^2}{\epsilon_0} \rho_\eta \right] \quad . \quad \text{A.2.21}$$

This is now recognized as the familiar one dimensional result with the  $\eta$ -derivatives taken to the right hand side and treated formally as non-homogeneous terms. Strictly speaking we should consider the singular case when  $w = 0$  so that  $\phi_\tau = 0$  and the choice A.2.19 cannot be made. However, the same result is obtained and, in any case, is not of interest here.

(ii) Now let  $\dot{\phi} \neq 0$ . Then perform successively the following row and column operations to  $\Delta$  as given by Equation A.2.16. Add  $g_0/c^2$  times column one to column four; subtract  $\zeta_2 \phi_\zeta / \dot{\phi}$  times row two from row one; subtract  $g_0 \zeta_2 \phi_\zeta / \rho \dot{\phi}$

times column two from column four; subtract  $g_0 \zeta_r \phi_\zeta / \rho \dot{\phi}$  times column three from column four; subtract  $\zeta_r \phi_\zeta / \dot{\phi}$  times row three from row one; add  $g_0/c^2$  times row four to row one. Then  $\Delta$  is equivalent to  $\bar{\Delta}$  where

$$\bar{\Delta} = \begin{bmatrix} 0 & 0 & 0 & \frac{g_0}{\dot{\phi} c^2} \left[ \dot{\phi}^2 - c^2 (\zeta_z^2 + \zeta_r^2) \phi_\zeta^2 \right] \\ 0 & \rho \dot{\phi} & 0 & 0 \\ 0 & 0 & \rho \dot{\phi} & 0 \\ -c^2 \dot{\phi} / g_0 & 0 & 0 & 0 \end{bmatrix}$$

Accordingly,  $\phi$  can only be characteristic if

$$\dot{\phi}^2 = c^2 (\zeta_z^2 + \zeta_r^2) \phi_\zeta^2 \quad . \quad \text{A.2.22}$$

That is

$$\phi_r + \left[ w \pm c \sqrt{\zeta_z^2 + \zeta_r^2} \right] \phi_\zeta = 0 \quad . \quad \text{A.2.23}$$

Then identifying Equation A.2.22 with F in Equation A.1.10 we see that the bicharacteristics satisfy the familiar one dimensional form

$$d\tau = \frac{d\zeta}{w \pm c (\zeta_z^2 + \zeta_r^2)^{1/2}} \quad \text{A.2.24}$$

The corresponding condition of compatibility is easily seen to be

$$\xi_1' - \frac{\zeta_z \phi_\zeta}{\dot{\phi}} \xi_2' - \frac{\zeta_r \phi_\zeta}{\dot{\phi}} \xi_3' + \frac{g_0}{c^2} \xi_4' = 0 \quad .$$

Then choosing  $\alpha$  and  $\beta$  as before, Equation A.2.19, and observing  $\phi_\zeta / \dot{\phi} = \mp 1/c$ .

where  $c_* = c(\zeta_z^2 + \zeta_r^2)^{1/2}$ , the condition of compatibility may be expressed as

$$\begin{aligned}
 p_\alpha \pm \frac{\rho c}{E_0} \frac{(\zeta_z u_\alpha + \zeta_r v_\alpha)}{\sqrt{\zeta_z^2 + \zeta_r^2}} \\
 &= \frac{c^2}{E_0} \left\{ [\xi_1 - (x\rho_\beta + \rho\eta_z u_\beta + \rho\eta_r v_\beta)] \right. \\
 &\pm \frac{\zeta_z}{c_*} [\xi_2 - (\rho x u_\beta + E_0 p_\beta \eta_z)] \\
 &\pm \frac{\zeta_r}{c_*} [\xi_3 - (\rho x v_\beta + E_0 p_\beta \eta_r)] \\
 &\left. + \frac{E_0}{c^2} [\xi_4 - x(p_\beta - \frac{c^2}{E_0} \rho_\beta)] \right\}
 \end{aligned}$$

A.2.25

As before, the  $\beta$ -derivatives are, in effect,  $\eta$ -derivatives which is to say derivatives along a coordinate curve which we may align with a computational boundary. Again, Equation A.2.25 is analogous with the one dimensional result with the cross derivatives ( $\beta$ -derivatives) treated formally as non-homogeneous terms.

In the present report we will require the result for a radial boundary. Transforming via  $\alpha \rightarrow \beta$ ,  $\zeta \rightarrow \eta$  and  $w \rightarrow x$  we have

$$p_\beta \pm \frac{\rho c^2}{E_0 c_*} [\eta_z u_\beta + \eta_r v_\beta] = \frac{c^2}{E_0} \frac{\xi_A}{[x \pm c_*]}$$

A.2.26

where  $\xi_A$  may be identified from Equation A.2.25 as the non-homogeneous group with crossflow terms with respect to  $\alpha$ . For a rectilinear grid we may restate Equation A.2.26 as

$$\frac{\partial p}{\partial t} + [v - v_m \pm c] \frac{\partial p}{\partial r} \pm \frac{\rho c}{E_0} \left[ \frac{\partial v}{\partial t} + [v - v_m \pm c] \frac{\partial v}{\partial r} \right] = \frac{c^2}{E_0} \xi_A$$

A.2.27

INTENTIONALLY LEFT BLANK.

**APPENDIX B:**  
**DESCRIPTION OF NGEN INPUT FILES**

**INTENTIONALLY LEFT BLANK.**

FILE 1 (10A8) PROBLEM TITLE (1 CARD).

TITLE - PROBLEM TITLE, UP TO 80 ALPHANUMERIC CHARACTERS.

FILE 2 (5I5,4X,11I1) LOGOUT OPTIONS (2 CARDS).

NPRINT - IF ZERO, TABLES OF THE STATE VARIABLES ARE NOT PRINTED.

- IF ONE, TABLES OF THE STATE VARIABLES ARE PRINTED ON A LOGOUT SCHEDULE DETERMINED BY NSTEP AND DTLOG AS DESCRIBED IN FILE 3.

NSUMRY - IF ZERO, NO SUMMARY TABLES ARE PRODUCED AT THE CONCLUSION OF THE RUN.

- IF ONE, SUMMARY TABLES ARE PROVIDED OF THE HISTORIES OF THE CONVENTIONAL INTERIOR BALLISTIC VARIABLES

NPLOT - IF ZERO, NO ISOMETRIC PLOTS PRODUCED ON LOGOUT.

- IF ONE, PLOTS OF STATE VARIABLES PRODUCED ON LOGOUT. THESE PLOTS ARE ISOMETRIC VIEWS OF THE STATE VARIABLES AS SELECTED IN ACCORDANCE WITH THE VALUES OF THE ARRAY IPLTV DEFINED BELOW. PLOTTING IS EFFECTED BY MEANS OF THE POSTPROCESSOR TGAP.

NDSKW - IF ZERO, NO DISC STORAGE ON LOGOUT.

- IF ONE, SOLUTION SAVED ON DISC (UNIT 8) ON LOGOUT.

NDSKR - IF ZERO, INITIAL DISTRIBUTIONS ARE CONSTRUCTED FROM INPUT DATA.

- IF NOT ZERO, INITIAL DISTRIBUTIONS ARE READ FROM UNIT 8 AND CORRESPOND TO TIME STEP EQUAL TO NDSKR.

IPLTV(I), I=1, ..., 11 - IF IPLTV(I)=1, THE QUANTITY TABULATED BELOW WILL BE PLOTTED AS AN ISOMETRIC VIEW. OTHERWISE, NOT.

I                    QUANTITY PLOTTED IF IPLTV(I)=1.  
-----

1	MESH.
2	POROSITY.
3	GRANULAR STRESS.
4	PRESSURE.
5	DENSITY.
6	GAS AXIAL VELOCITY.
7	SOLID AXIAL VELOCITY.
8	GAS RADIAL VELOCITY.
9	SOLID RADIAL VELOCITY.
10	GAS TEMPERATURE.
11	PARTICLE SURFACE TEMPERATURE.

FILE 3 (I5,F10.0,I5,F10.0,I5) TERMINATION AND OUTPUT  
PARAMETERS (1 CARD).

NSTOP - INTEGRATION STEP FOR TERMINATION.  
ZSTOP - PROJECTILE DISPLACEMENT FOR TERMINATION (CM).  
NSTEP - NUMBER OF STEPS BEFORE PRINTOUT  
DTPRT - TIME INTERVAL FOR PRINTOUT (MSEC).  
NDEBUG - DEBUG SWITCH. IF ZERO THERE IS NO DEBUG PRINT.  
IF NDEBUG = 1, DEBUG PRINTING OCCURS ON UNIT  
FORT.50. FILE 3.1 AND 3.2 ARE REQUIRED.

FILE 3.1 (3I5) DEBUG PARAMETERS (1 CARD).

NDTON - INTEGRATION STEP AT WHICH DEBUG COMMENCES.  
NDTOFF - STEP AT WHICH DEBUG CEASES.  
NJLIS - NUMBER OF CELL STRINGS.

FILE 3.2 (3I5) DEBUG CELL STRINGS (NJLIS CARDS).

JDIR(I) - IF 1, DEBUG OCCURS ON AXIAL SWEEP.  
IF 2, DEBUG OCCURS ON RADIAL SWEEP.  
JLIS(I,1) - FIRST RADIAL OR AXIAL LOCATION FOR  
DEBUG.  
JLIS(I,2) - LAST RADIAL OR AXIAL LOCATION FOR  
DEBUG.

DEBUG PRINT OCCURS FOR THE LAST 5 AXIAL OR RADIAL  
CELLS AT EACH RADIAL OR AXIAL LOCATION ACCORDING  
AS JDIR IS EITHER 1 OR 2.

FILE 4 (2F10.0,3I5) CONTINUUM MESH PARAMETERS (1 CARD).

CRN - COURANT NUMBER, MUST BE LESS THAN ONE. A  
VALUE OF 0.5 IS RECOMMENDED.  
DIFF1 - FRACTION OF ANTIDIFFUSIVE FLUX ALLOWED. A  
VALUE OF 0.999 IS RECOMMENDED.  
NCELLR - TOTAL NUMBER OF RADIAL CELLS.  
NCHMIN - INITIAL NUMBER OF AXIAL CELLS ALLOCATED TO  
REGION BEHIND THE BASE OF THE AFTERBODY.  
NCHMAX - MAXIMUM NUMBER OF AXIAL CELLS ALLOCATED TO  
REGION BEHIND THE BASE OF THE AFTERBODY.  
THIS DATUM IS PRESENTLY INACTIVE.  
NABDYZ - NUMBER OF AXIAL CELLS ALLOCATED TO AFTERBODY.  
IF > 0, FILES 22 AND 23 ARE REQUIRED.  
NABDYR - NUMBER OF RADIAL CELLS ALLOCATED TO BASE OF  
AFTERBODY.

NOTES: (1) NABDYZ AND NABDYR ARE ONLY REQUIRED IF AN  
INTRUDING AFTERBODY IS PRESENT.  
(2) NCELLR MUST NOT EXCEED 25.  
(3) THE SUM OF NCHMIN AND NABDYZ MUST NOT  
EXCEED 200.

FILE 5 (4F10.0) AMBIENT CONDITIONS (1 CARD).

PO - INITIAL PRESSURE OF GAS PHASE (MPA).

TEMPO - INITIAL TEMPERATURE OF GAS PHASES (DEG.K). THIS IS ALSO THE INITIAL TEMPERATURE OF ANY PROPELLANT FOR WHICH XTEMST IS ZERO IN FILE 8.

GAMMA0 - RATIO OF SPECIFIC HEATS OF AMBIENT GAS (-).

GMOL0 - MOLECULAR WEIGHT OF AMBIENT GAS (GM/GM-MOL).

BV - COVOLUME (CM\*\*3/GM).

FILE 6 (3I5) CHARGE REPRESENTATION PARAMETERS (1 CARD).

NPRPS - NUMBER OF TYPES OF PROPELLANT IN CHARGE. MAXIMUM OF 10.

NBAGS - NUMBER OF INCREMENTS OF PROPELLANT. MAXIMUM OF LPIN, A PARAMETER PRESENTLY SET EQUAL TO 4. LPIN SHOULD NOT BE INCREASED TO A VALUE LARGER THAN 10.

MODPRP - IF 0, NO SOLID PROPELLANT INCREMENTS ARE PRESENT. IF 1, THE PROPELLANT IS MODELED ACCORDING TO A SIMPLE LUMPED PARAMETER MODEL IN WHICH THE CHARGE CONSISTS OF A SINGLE INCREMENT AND EXPANDS ONLY IN THE AXIAL DIRECTION AND ACCORDING TO A LAGRANGEAN (LINEAR) DISTRIBUTION. FILE 10.5 IS REQUIRED. THE PROPELLANT IS ASSUMED TO BE TYPE 1.

IF 2, THE INCREMENTS ARE MODELING USING A TWO-DIMENSIONAL MODEL. FILE 11 IS REQUIRED.

NOTE : FILES 6.5,7,8,9,10 ARE REPEATED, AS A GROUP, NPRPS TIMES, ONCE FOR EACH OF THE NPRPS TYPES OF PROPELLANT PRESENT IN THE CHARGE.

IT SHOULD BE NOTED THAT THE SUBSCRIPT USED TO DISTINGUISH THE VARIOUS TYPES OF PROPELLANT IS SUPPRESSED IN THE SUBSEQUENT DISCUSSION.

FILE 6.5 (10A8) PROPELLANT NAME (1 CARD).

PRNAME - PROPELLANT DESCRIPTION. UP TO 80 ALPHANUMERIC CHARACTERS.

FILE 7 (8F10.0) SOLID PHASE CONSTITUTIVE DATA (1 CARD).

XEE - SETTLING POROSITY OF BED (-).

SEE THE NOTE FOLLOWING THE DISCUSSION OF FILE 11 CONCERNING DEFAULT PROPERTIES OF THIS DATUM.

XAP1 - RATE OF PROPAGATION OF COMPRESSIVE WAVE IN SETTLED BED (CM/SEC).

XAP2 - RATE OF PROPAGATION OF UNLOADING WAVE (CM/SEC).

XRHOP - DENSITY OF SOLID PHASE (GM/CC).

XKP - THERMAL CONDUCTIVITY OF SOLID PHASE (J/CM-SEC-DEG.K).

XALFAP - THERMAL DIFFUSIVITY OF SOLID PHASE (CM\*\*2/SEC).

FILE 8 (4F10.0) GAS PHASE CONSTITUTIVE DATA AND INITIAL PROPELLANT TEMPERATURE (1 CARD).

XGAM - RATIO OF SPECIFIC HEATS (-).  
XGMOL - MOLECULAR WEIGHT (GM/GM-MOL).  
XBV - COVOLUME (CC/GM).  
XTEMST - INITIAL TEMPERATURE OF SOLID PROPELLANT (DEG.K). IF XTEMST IS ENTERED AS ZERO, IT DEFAULTS TO TEMPO AS DESCRIBED IN FILE 5.

FILE 9 (I5/(8F10.0)) SOLID PHASE COMBUSTION CHARACTERISTICS (2 OR MORE CARDS).

NTB - NUMBER OF TABULAR DATA TO DEFINE BURN RATE. MAXIMUM OF 10.

XTIG - IGNITION TEMPERATURE OF SOLID PHASE (DEG.K). THIS QUANTITY STARTS A NEW CARD.

XECH - CHEMICAL ENERGY RELEASED IN COMBUSTION (J/GM).

TMAXP(1) - MAXIMUM PRESSURE FOR WHICH CORRESPONDING COEFFICIENTS ARE APPLICABLE IN THE LAW  $RDOT = TB1(1) + TB2(1) * P^{**} * TBN(1)$  WHERE P IS PRESSURE AND RDOT IS REGRESSION RATE. THIS QUANTITY STARTS A NEW CARD.

TB1(1) - BURN RATE ADDITIVE CONSTANT (CM/SEC).

TB2(1) - BURN RATE PRE-EXPONENTIAL FACTOR (CM/SEC-MPA\*\*BN).

TBN(1) - BURN RATE EXPONENT (-).

TMAXP(NTB) - MAXIMUM PRESSURE FOR WHICH CORRESPONDING COEFFICIENTS ARE APPLICABLE IN THE LAW  $RDOT = TB1(NTB) + TB2(NTB) * P^{**} * TBN(NTB)$  WHERE P IS PRESSURE AND RDOT IS REGRESSION RATE.

TB1(NTB) - BURN RATE ADDITIVE CONSTANT (CM/SEC).

TB2(NTB) - BURN RATE PRE-EXPONENTIAL FACTOR (CM/SEC-MPA\*\*BN).

TBN(NTB) - BURN RATE EXPONENT (-).

NOTES: (1) A NEW CARD IS STARTED FOR TMAXP(1), TMAXP(3) ETC, BUT NOT FOR TMAXP(2), TMAXP(4) ETC.

(2) IF THE PRESSURE EXCEEDS TMAXP(NTB), THE CORRESPONDING DATA ARE USED AS DEFAULT VALUES.

FILE 10 (I5,6F10.0) GRAIN GEOMETRY (1 CARD).

NFORM - IF ZERO, GRAIN IS A CYLINDER.

- IF ONE, GRAIN IS A SPHERE.

- IF TWO, GRAIN IS AN UNPERFORATED STICK.

XOD - EXTERNAL DIAMETER (CM).

XGLEN - LENGTH (CM).

XDPERF - DIAMETER OF PERFORATION (CM).

XNPERF - NUMBER OF PERFORATIONS (-).

FILE 10.5 (5F10.0) DESCRIPTION OF INCREMENT FOR LUMPED PARAMETER  
MODEL WITH LAGRANGEAN MOTION (1 CARD).

NOTE: FILE REQUIRED IF AND ONLY IF MODPRP (FILE 6) IS EQUAL TO 1.

- PROPMO - INITIAL MASS OF PROPELLANT (GM).
- ZPROP1 - POSITION OF FORWARD BOUNDARY OF CYLINDRICAL CORE (CM).
- ZPROP2 - POSITION OF FORWARD BOUNDARY OF PROPELLANT (CM). THE  
POROSITY IS UNIFORM FROM ZERO TO ZPROP1 AND TAPERS  
LINEARLY TO ONE FROM ZPROP1 TO ZPROP2. THESE VALUES  
EXPAND IN PROPORTION TO THE MOTION OF THE PROJECTILE.  
NO ACCOUNT IS TAKEN OF ANY POSSIBLE INTRUSION BY THE  
TUBE OR AFTERBODY IN CALCULATING THE POROSITY.
- RPROP1 - POSITION OF OUTER BOUNDARY OF CYLINDRICAL CORE (CM).
- RPROP2 - POSITION OF OUTER BOUNDARY OF PROPELLANT (CM). THESE  
DATA CONTROL THE RADIAL DISTRIBUTION OF POROSITY IN  
A FASHION ANALOGOUS TO ZPROP1 AND ZPROP2 EXCEPT THAT  
THEY REMAIN CONSTANT AT ALL TIMES.

NOTE: FILE 11 IS REPEATED NBAGS TIMES, ONCE FOR EACH OF THE NBAGS  
INCREMENTS OF PROPELLANT.

IT SHOULD BE NOTED THAT THE SUBSCRIPT USED TO DISTINGUISH  
THE VARIOUS BAGS OF PROPELLANT IS SUPPRESSED.

FILE 11 (3I5,5F10.0) DESCRIPTION OF INCREMENT FOR TWO-DIMENSIONAL  
MODELING (1 CARD).

NOTE: FILE REQUIRED IF AND ONLY IF MODPRP (FILE 6) IS EQUAL TO 2.

- MPRP - POINTER TO FILE OF PROPELLANT PROPERTIES WHICH  
CHARACTERIZE THE MAIN CHARGE CONTAINED IN THE INCREMENT.  
MPRP MUST BE GREATER THAN ZERO AND LESS THAN OR  
EQUAL TO NPRPS (FILE 5).
- NZC - NUMBER OF AXIAL PARTICLES FOR INCREMENT. MUST NOT  
EXCEED PARAMETER LPIZ, PRESENTLY EQUAL TO 50.
- NRC - NUMBER OF RADIAL PARTICLES FOR INCREMENT. MUST NOT  
EXCEED LPIR, PRESENTLY EQUAL TO 20.
- XCHWT - INITIAL MASS OF MAIN CHARGE IN INCREMENT (GM).
- XZR - INITIAL POSITION OF REAR BOUNDARY (CM).
- XZF - INITIAL POSITION OF FORWARD BOUNDARY (CM).
- XRI - INITIAL POSITION OF INNER BOUNDARY (CM).
- XRO - INITIAL POSITION OF OUTER BOUNDARY (CM).

- NOTES: (1) IF XZR, XZF, XRI OR XRO IS ENTERED AS ZERO, IT IS  
DEFAULTED TO THE CORRESPONDING BOUNDARY OF THE GUN  
CHAMBER.
- (2) THE INCREMENT IS TAKEN TO BE UNIFORMLY DISTRIBUTED  
WITHIN THE ENVELOPE DEFINED BY THESE DATA LESS ANY  
INTRUSIONS BY THE TUBE WALL OR THE AFTERBODY.
- (3) PRESENT CODING ASSUMES MULTIPLE INCREMENTS TO BE  
ARRANGED END-TO-END.

FILE 12 (415) IGNITER DISCHARGE TABLE COUNTERS AND OPTIONS  
(1 CARD).

- NTABIG - IF ZERO, A TABULAR REPRESENTATION OF AN IGNITION STIMULUS VIEWED AS AN EXTERNALLY INJECTED SOURCE IS NOT CONSIDERED.
- IF ONE, AN EXTERNALLY INJECTED IGNITION SOURCE IS CONSIDERED. VALUES OF JZP, JRP AND JTP MUST BE SPECIFIED AND FILES 13,14,15 16 AND 17 MUST BE INCLUDED.
- JZP - NUMBER OF AXIAL STATIONS IN DISCHARGE TABLE FOR CASE WHEN NTABIG EQUALS ONE.  
JZP MUST NOT EXCEED TWENTY.
- JRP - NUMBER OF RADIAL STATIONS IN DISCHARGE TABLE FOR CASE WHEN NTABIG EQUALS ONE.  
JRP MUST NOT EXCEED EIGHT.
- JTP - NUMBER OF TIME LEVELS IN DISCHARGE TABLE FOR CASE WHEN NTABIG EQUALS ONE.  
JTP MUST NOT EXCEED TWENTY.

FILE 13 (3F10.0) ENERGY OF EXTERNAL IGNITION SOURCE (1 CARD).  
NOTE: THIS FILE IS REQUIRED IF AND ONLY IF NTABIG IS EQUAL TO ONE.

- EIG - ENERGY OF IGNITER GAS (J/GM).  
GAMIG - RATIO OF SPECIFIC HEATS OF IGNITER GAS (-).  
GMOLIG - MOLECULAR WEIGHT OF IGNITER GAS (GM/GMOL).

FILE 14 (8F10.0) AXIAL POSITIONS FOR DISCHARGE TABLE (1 TO 3 CARDS).  
NOTE: THIS FILE IS REQUIRED IF AND ONLY IF NTABIG IS EQUAL TO ONE.

ZPHI(I), I=1, JZP - AXIAL POSITIONS (CM).

FILE 15 (8F10.0) RADIAL POSITIONS FOR DISCHARGE TABLE (1 CARD).  
NOTE: THIS FILE IS REQUIRED IF AND ONLY IF NTABIG IS EQUAL TO ONE.

RPHI(I), I=1, JRP - RADIAL POSITIONS (CM).

FILE 16 (8F10.0) TIME LEVELS FOR DISCHARGE TABLE (1 TO 3 CARDS).  
NOTE: THIS FILE IS REQUIRED IF AND ONLY IF NTABIG IS EQUAL TO ONE.

TPHI(I), I=1, JTP - TIME LEVELS (MSEC).

FILE 17 (8F10.0) DISCHARGE TABLE (JRP\*JTP TO 3\*JRP\*JTP CARDS).  
NOTE: THIS FILE IS REQUIRED IF AND ONLY IF NTABIG IS EQUAL  
TO ONE.

PHI(1,1,1) - FIRST VALUE OF RATE OF DISCHARGE PER UNIT VOLUME  
(GM/CC-SEC).

PHI(2,1,1) - SECOND VALUE.

PHI(JZP,1,1) - VALUE AT LAST AXIAL POSITION, FIRST RADIAL  
POSITION AND FIRST TIME.

PHI(1,2,1) - VALUE AT FIRST AXIAL, SECOND RADIAL POSITION.  
THIS ENTRY STARTS A NEW CARD.

PHI(JZP,JRP,JTP) - LAST VALUE.

FILE 18 (2F10.0,5I5) PROJECTILE POSITION, MASS,  
AND BORE RESISTANCE DATA (1 CARD).

ZPO - INITIAL LOCATION OF BASE OF PROJECTILE  
OR SABOT (CM). THIS CORRESPONDS TO THE  
FORWARD BOUNDARY OF THE COMPUTATIONAL  
DOMAIN AND THE AFTERBODY, IF PRESENT, IS  
VIEWED AS INTRUDING INTO THE REGION TO  
REAR OF THIS LOCATION.

PRMASS - PROJECTILE MASS (KG).

NBRES - NUMBER OF ENTRIES IN TABULAR DESCRIPTION OF  
BORE RESISTANCE. MUST NOT EXCEED 10.

IBRES - TYPE OF LAW FOR BORE RESISTANCE.

IF 1, RESISTANCE GIVEN DIRECTLY BY INTERPOLATION  
OF TABULAR DATA OF FILE 28.

IF 2, INTERPOLATED VALUE MULTIPLIED BY  
 $7.2/v^{0.6}$

WHERE V IS PROJECTILE VELOCITY IN FT/SEC.

IF 3, INTERPOLATED VALUE MULTIPLIED BY

$(1+.0004414v)/1+.005046v$

WHERE V IS PROJECTILE VELOCITY IN IN/SEC.

IF 11,12 OR 13, THE RESISTANCE IS AS FOR 1,2 OR 3  
RESPECTIVELY AND THE RESISTANCE DUE TO  
COMPRESSED AIR IN FRONT OF THE PROJECTILE  
IS ALSO TAKEN INTO ACCOUNT ACCORDING TO AN  
ANALYTICAL FORMULA BASED ON STEADY-STATE  
SHOCK THEORY.

FILE 19 (8F10.0) BORE RESISTANCE TABLE (1 TO 3 CARDS).

ZBRES(1) - FIRST VALUE OF PROJECTILE DISPLACEMENT  
AT WHICH BORE RESISTANCE IS SPECIFIED  
(CM).

FBRES(1) - CORRESPONDING VALUE OF BORE RESISTANCE  
(MPA).

ZBRES(NBRES) - LAST VALUE OF DISPLACEMENT.

FBRES(NBRES) - CORRESPONDING VALUE OF BORE RESISTANCE.

FILE 20 (15) TUBE GEOMETRY FILE COUNTER (1 CARD).

NBYE - NUMBER OF PAIRS OF DATA TO DEFINE TUBE GEOMETRY.  
MINIMUM OF TWO AND MAXIMUM OF TEN.

FILE 21 (2F10.0) TUBE GEOMETRY DATA (NBYE CARDS).

ZBYE(1) - FIRST AXIAL POSITION (CM).

RBYE(1) - CORRESPONDING RADIAL POSITION (CM).

ZBYE(2) - SECOND AXIAL POSITION. STARTS A NEW CARD.

RBYE(NBYE)

NOTE: THE GEOMETRY IS ARBITRARY EXCEPT THAT ZBYE(I) MUST BE  
GREATER THAN ZBYE(I-1) AND THAT THE RESULTING  
CONFIGURATION MUST NOT CROSS ANY AXIAL LINE IN MORE  
THAN TWO LOCATIONS. PRESENT CODING IN NGEN ASSUMES  
THAT THE OPEN CELLS FOR EACH AXIAL SWEEP ARE SINGLY  
CONNECTED. CODING ALSO ASSUMES THAT THE TUBE WALL  
IS MODERATELY TAPERED. TUBES WITH VERY STRONG CHAMBRAGE  
MAY PRESENT COMPUTATIONAL DIFFICULTIES WITH THE PRESENT  
ALGORITHM.

FILE 22 (15) AFTERBODY FILE COUNTER (1 CARD).

NOTE: THIS FILE IS ONLY REQUIRED IF NABDYZ (FILE 4) IS GREATER  
THAN ZERO.

NBYI - NUMBER OF PAIRS OF DATA TO DEFINE AFTERBODY GEOMETRY.  
MINIMUM OF TWO AND MAXIMUM OF TEN.

FILE 23 (2F10.0) AFTERBODY GEOMETRY (NBYI CARDS).

NOTE: THIS FILE IS ONLY REQUIRED IF NABDYZ (FILE 4) IS GREATER  
THAN ZERO.

ZBYI(1) - FIRST AXIAL POSITION (CM).

RBYI(1) - CORRESPONDING RADIAL POSITION (CM).

ZBYI(2) - SECOND AXIAL POSITION. STARTS A NEW CARD.

RBYI(NBYI)

NOTE: THE COMMENTS CONCERNING THE TUBE GEOMETRY DATA APPLY  
HERE ALSO. IN ADDITION NOTE THAT THE AFTERBODY DATA  
ARE NOT NECESSARILY REFERENCED TO THE BREECHFACE. AN

INTERNAL ADJUSTMENT COLLOCATES ZBYI(NBYI) WITH THE  
BASE OF THE PROJECTILE/SABOT.  
ALSO NOTE THAT IT IS ASSUMED THAT THE BASE OF THE AFTERBODY,  
LIKE THAT OF THE BASE OF THE PROJECTILE/SABOT, IS FLAT AND  
OF SUFFICIENT RADIAL EXTENSION TO BE COVERED BY AT LEAST  
ONE RADIAL CELL (SEE NABDYR, FILE 4). FINALLY, THE EXPOSED  
PART OF THE BASE OF THE PROJECTILE/SABOT MUST BE LARGE  
ENOUGH TO BE COVERED BY AT LEAST 3 RADIAL CELLS IN THE  
PRESENT VERSION OF THE CODE.

INTENTIONALLY LEFT BLANK.

NO. OF  
COPIES

ORGANIZATION

2 ADMINISTRATOR  
ATTN DTIC DDA  
DEFENSE TECHNICAL INFO CTR  
CAMERON STATION  
ALEXANDRIA VA 22304-6145

1 DIRECTOR  
ATTN AMSRL OP SD TA  
US ARMY RESEARCH LAB  
2800 POWDER MILL RD  
ADELPHI MD 20783-1145

3 DIRECTOR  
ATTN AMSRL OP SD TL  
US ARMY RESEARCH LAB  
2800 POWDER MILL RD  
ADELPHI MD 20783-1145

1 DIRECTOR  
ATTN AMSRL OP SD TP  
US ARMY RESEARCH LAB  
2800 POWDER MILL RD  
ADELPHI MD 20783-1145

ABERDEEN PROVING GROUND

5 DIR USARL  
ATTN AMSRL OP AP L (305)

<u>NO. OF</u> <u>COPIES</u>	<u>ORGANIZATION</u>	<u>NO. OF</u> <u>COPIES</u>	<u>ORGANIZATION</u>
1	HQDA ATTN SARD TR MS K KOMINOS PENTAGON WASHINGTON DC 20310-0103	1	PM PEO ARMAMENTS ATTN AMCPM TMA TANK MAIN ARMAMENT SYSTEM PCNTY ARSNL NJ 07806-5000
1	HQDA ATTN SARD TR DR R CHAIT PENTAGON WASHINGTON DC 20310-0103	1	PM PEO ARMAMENTS ATTN AMCPM TMA 105 TANK MAIN ARMAMENT SYSTEM PCNTY ARSNL NJ 07806-5000
1	CHAIRMAN DOD EXPLOSIVES SAFETY BD HOFFMAN BLDG 1 RM 856 C 2461 EISENHOWER AVE ALEXANDRIA VA 22331-0600	1	PM PEO ARMAMENTS ATTN AMCPM TMA 120 TANK MAIN ARMAMENT SYSTEM PCNTY ARSNL NJ 07806-5000
1	HQS US ARMY MATERIEL CMD ATTN AMCICP AD M FISETTE 5001 EISENHOWER AVE ALEXANDRIA VA 22333-0001	1	PM PEO ARMAMENTS ATTN AMCPM TMA AS H YUEN TANK MAIN ARMAMENT SYSTEM PCNTY ARSNL NJ 07806-5000
1	US ARMY BMDS CMD ADVANCED TECHLGY CTR PO BOX 1500 HUNTSVILLE AL 35807-3801	2	CDR US ARMY ARDEC ATTN SMCAR CCH V C MANDALA E FENNELL PCNTY ARSNL NJ 07806-5000
1	OFC OF THE PRODUCT MGR ATTN SFAE AR HIP IP MR R DE KLEINE 155MM HOWITZER M109A6 PALADIN PCNTY ARSNL NJ 07806-5000	1	CDR US ARMY ARDEC ATTN SMCAR CCH T L ROSENDORF PCNTY ARSNL NJ 07806-5000
3	PM ADV FIELD ARTLRY SYSTEM ATTN SFAE ASM AF E LTC A ELLIS T KURIATA J SHIELDS PCNTY ARSNL NJ 07801-5000	1	CDR US ARMY ARDEC ATTN SMCAR CCS PCNTY ARSNL NJ 07806-5000
1	PM ADV FIELD ARTLRY SYSTEM ATTN SFAE ASM AF Q W WARREN PCNTY ARSNL NJ 07801-5000	1	CDR US ARMY ARDEC ATTN SMCAR AEE J LANNON PCNTY ARSNL NJ 07806-5000
1	CDR US ARMY ARDEC ATTN AMSMC PBM A SIKLOSI PROD BASE MODERNIZATION AGENCY PCNTY ARSNL NJ 07806-5000	11	CDR US ARMY ARDEC ATTN SMCAR AEE B A BEARDELL D DOWNS S EINSTEIN S WESTLEY S BERNSTEIN J RUTKOWSKI B BRODMAN P O'REILLY R CIRINCIONE P HUI J O'REILLY PCNTY ARSNL NJ 07806-5000
1	CDR US ARMY ARDEC ATTN AMSMC PBM E L LAIBSON PROD BASE MODERNIZATION AGENCY PCNTY ARSNL NJ 07806-5000		

<u>NO. OF COPIES</u>	<u>ORGANIZATION</u>
5	COMMANDER ATTN SMCAR AEE WW M MEZGER J PINTO D WIEGAND P LU C HU US ARMY ARDEC PCNTY ARSNL NJ 07806-5000
1	COMMANDER ATTN SMCAR AES S KAPLOWITZ US ARMY ARDEC PCNTY ARSNL NJ 07806-5000
1	COMMANDER ATTN SMCAR HFM E BARRIERES US ARMY ARDEC PCNTY ARSNL NJ 07806-5000
1	COMMANDER ATTN SMCAR FSA T M SALSURY US ARMY ARDEC PCNTY ARSNL NJ 07806-5000
1	COMMANDER ATTN SMCAR FSA F LTC R RIDDLE US ARMY ARDEC PCNTY ARSNL NJ 07806-5000
1	COMMANDER ATTN SMCAR FSC G FERDINAND US ARMY ARDEC PCNTY ARSNL NJ 07806-5000
1	COMMANDER ATTN SMCAR FS T GORA US ARMY ARDEC PCNTY ARSNL NJ 07806-5000
1	COMMANDER ATTN SMCAR FS DH J FENECK US ARMY ARDEC PCNTY ARSNL NJ 07806-5000
3	COMMANDER ATTN SMCAR FSS A R KOPMANN B MACHEK L PINDER US ARMY ARDEC PCNTY ARSNL NJ 07806-5000

<u>NO. OF COPIES</u>	<u>ORGANIZATION</u>
1	COMMANDER ATTN SMCAR FSN N K CHUNG US ARMY ARDEC PCNTY ARSNL NJ 07806-5000
2	DIR BENET WEAPONS LABS ATTN SMCAR CCB RA G P O'HARA G A PFLEGL WATERVLIET NY 12189-4050
1	DIR BENET WEAPONS LABS ATTN SMCAR CCB RT S SOPOK WATERVLIET NY 12189-4050
1	DIR BENET WEAPONS LABS ATTN SMCAR CCB S F HEISER WATERVLIET NY 12189-4050
2	CDR US ARMY RSRCH OFC ATTN TECHNICAL LIBRARY D MANN PO BOX 12211 RSCH TRI PK NC 27709-2211
1	CDR USACECOM ATTN ASQNC ELC IS L R MYER CENTER R&D TECHNICAL LIBRARY FORT MONMOUTH NJ 07703-5301
1	CMDT US ARMY AVIATION SCHOOL ATTN AVIATION AGENCY FORT RUCKER AL 36360
1	PM US TANK AUTOMOTIVE CMD ATTN AMCPM ABMS T DEAN WARREN MI 48092-2498
1	PM US TANK AUTOMOTIVE CMD ATTN SFAE ASM BV FIGHTING VEHICLE SYSTEMS WARREN MI 48397-5000
1	PM ABRAMS TANK SYSTEM ATTN SFAE ASM AB WARREN MI 48397-5000
1	DIR HQ TRAC RPD ATTN ATCD MA FORT MONROE VA 23651-5143

<u>NO. OF COPIES</u>	<u>ORGANIZATION</u>	<u>NO. OF COPIES</u>	<u>ORGANIZATION</u>
1	COMMANDER ATTN STRBE WC US ARMY BELVOIR R&D CTR FORT BELVOIR VA 22060-5006	1	CDR NAVAL AIR SYSTEMS CMD ATTN AIR 954 TECH LIBRARY WASH DC 20360
1	DIRECTOR ATTN ATRC L MR CAMERON US ARMY TRAC FT LEE FORT LEE VA 23801-6140	4	CDR NAVAL RSRCH LAB ATTN TECHNICAL LIBRARY CODE 4410 K KAILASANATE J BORIS E ORAN WASH DC 20375-5000
1	COMMANDANT US ARMY CMD & GEN STAFF COLLEGE FORT LEAVENWORTH KS 66027	1	OFFICE OF NAVAL RSRCH ATTN CODE 473 R S MILLER 800 N QUINCY STREET ARLINGTON VA 22217-9999
1	COMMANDANT ATTN REV AND TRNG LIT DIV US ARMY SPECIAL WARFARE SCHOOL FORT BRAGG NC 28307	1	OFFICE OF NAVAL TECHLGY ATTN ONT 213 D SIEGEL 800 N QUINCY ST ARLINGTON VA 22217-5000
1	COMMANDER ATTN SMCAR QA HI LIB RADFORD ARMY AMMUNITION PLANT RADFORD VA 24141-0298	1	CDR NAVAL SURFACE WARFARE CTR ATTN CODE 730 SILVER SPRING MD 20903-5000
1	COMMANDER ATTN AMXST MC 3 US ARMY FRGN SCIENCE & TECHLGY CTR 220 SEVENTH STREET NE CHRLTTESVLE VA 22901-5396	1	CDR NAVAL SURFACE WARFARE CTR ATTN CODE R 13 R BERNECKER SILVER SPRING MD 20903-5000
1	COMMANDANT ATTN ATSF CD COL T STRICKLIN US ARMY FIELD ARTLRY CTR & SCHOOL FT SILL OK 73503-5600	7	CDR NAVAL SURFACE WARFARE CTR ATTN T C SMITH K RICE S MITCHELL S PETERS J CONSAGA C GOTZMER TECHNICAL LIBRARY INDIAN HEAD MD 20640-5000
1	COMMANDANT ATSF CN P GROSS US ARMY FIELD ARTLRY CTR & SCHOOL FT SILL OK 73503-5600	1	CDR NAVAL SURFACE WARFARE CTR ATTN CODE G30 GUNS & MUNITIONS DIV DAHLGREN VA 22448-5000
1	CMDT US ARMY ARMOR SCHOOL ATTN ATZK CD MS M FALKOVITCH ARMOR AGENCY FORT KNOX KY 40121-5215	1	CDR NAVAL SURFACE WARFARE CTR ATTN CODE G32 GUNS SYSTEMS DIV DAHLGREN VA 22448-5000
2	CDR NAVAL SEA SYSTEMS CMD ATTN SEA 62R SEA 64 WASH DC 20362-5101	1	CDR NAVAL SURFACE WARFARE CTR ATTN CODE G33 T DORAN DAHLGREN VA 22448-5000